Contact electrification in aerosolized micron-sized solid particles: dependence upon size, chemical composition and gas properties

vorgelegt von
Dipl.-Ing.
Stefano Alois
geb. in Roma

von der Fakultät V – Verkehrs- und Maschinensysteme
der Technischen Universität Berlin
zur Erlangung des akademischen Grades

Doktor der Ingenieurwissenschaften
-Dr.-Ing.-

genehmigte Dissertation

Promotionausschuss:

Vorsitzender:	Prof. Dr.-Ing. habil. Manfred Zehn
Gutachter:	Prof. Dr. sc. techn. habil. Jörn Sesterhenn
Gutachter:	Dr. Stephen Lane

Tag der wissenschaftlichen Aussprache: 21. November 2018

Berlin, 2018

Stefano Alois
Institute of Fluid Mechanics and Engineering Acoustics
Technische Universität Berlin
Müller-Breslau-Str. 15
10623, Berlin
Germany
Email: stefano.alois@gmail.com
This document was compiled and typeset in LaTeX

Zusamenfassung

Die Kontaktelektrifizierung ist in unserem Alltag allgegenwärtig und ihr kommt eine enorme Bedeutung für Partikel im Mikrometerbereich zu. Hier könnte sie in einer Vielzahl von praktischen Anwedungen von erheblichem Nutzen dabei sein, die Ladung der Partikel zu fördern beziehungsweise zu verhindern. Trotz umfangreicher Untersuchungen, ein vollständiges Verständnis der Ladungstransfermechanismen fehlt noch.
In dieser Arbeit wird die Kontaktelektrifizierung aerosolierter Partikel im Mikrometerbereich experimentell mit neuartigen Sensortechnologien untersucht. Eine neue laserbasierte Technik wurde entwickelt, die die gleichzeitige Bestimmung von Größe und elektrischer Ladung einzelner Partikel erlaubt, welche sich in einer speziellen Kammer unter kontrollierten Umweltbedingungen absetzen. Es konnte beobachtet werden, dass Partikel in einem Größenbereich von $1-8\mu$m die mit der Einlassröhre interargieren elektrifiziert werden, wobei die Oberflächenladungskonzentration (σ) dabei in einem relativ engen Bereich um $\pm 100\text{e}/\mu\text{m}^2$ ($\approx \pm 0.02\text{mC}/\text{m}^2$) liegt. Erklärungen für diesen Effekt werden in den folgenden Abschnitten diskutiert, wie zum Beispiel die Möglichkeit der Feldemission an der Kontaktstelle die die Oberflächenladungsdichte beschränkt. In einer zweiten Messtechnik wurde die elektrische Spannung am Injektorsystem (z.B. Faraday-Röhre) während der Aerosolisierung gemessen, um die Größen- und Zusammensetzungsabhängigkeit der geladene Partikel die das Einlassrohr verlassen zu untersuchen. In Übereinstimmung mit den Werten von σ die mithilfe der lasergestützten Technik bestimmt wurden, zeigte sich auch hier, dass die Nettoladung linear mit der gesamten Partikeloberfläche zunimmt. Aufbauend auf der Zusammensetzungsabhängigkeit der Kontaktelektrifizierung wird ein neues, einfaches und physikalisch sinnvolles Modell vorgeschlagen auf der Grundlage des Elektronentransfers: Bei isolierenden Oxiden wurde eine lineare Korrelation zwischen σ und der absolute generalized relative electronegativity (χ_{AGR}) gefunden, welche man mithilfe der Kenntnis der Zusammensetzung der Kontaktflächen erhält; $\sigma = a\chi_{\text{AGR}} - b$, mit $a = 4.7\text{e}/\mu\text{m}^2/\text{V}$, $b = -27\text{e}/\mu\text{m}^2$. Dieses prädiktive Modell kann zur Abschätzung des Ausmaßes der Kontaktladung verwendet werden und zeigt annehmbare Übereinstimmungen mit der Kontaktelektrifizierung die bei Proben von Vulkanasche beobachtet wurden, wenn diese als Siliziumoxide behandelt wurden. Für Metalle kann festgestellt werden, dass die Ladung mit der Elektronenarbeitsfunktion sowie der Elektronegativität korreliert, wenn auch nur mit eingeschränkter Genauigkeit. Der Prozess der Kontaktelektrifizierung scheint nicht stark von der Zusammensetzung des Gases beeinflusst zu sein. Auch die Effekte der relativen Luftfeuchtigkeit, Partikelaggregation (Kohäsion), Haftung

an der Einlassrohrwand und elektrischer Gasdurchschlag wurden untersucht. Diese Arbeit soll unser Verständnis der Kontaktelektrifizierung fördern und neue Herausforderungen an zukünfitige Forschung vorantreiben.

Abstract

Contact electrification is ubiquitously present in our everyday life and acquires significant importance for micron scale particles, where it may be of considerable use in order to prevent/promote charging in a variety of practical applications. Despite being widely studied, a complete understanding of the charge transfer mechanisms is still lacking.

In this work, contact electrification of aerosolized micron scale particles is experimentally investigated using novel sensor techniques. A new laser-based technique has been developed, allowing the simultaneous determination of size and electrical charge of individual particles settling under controlled conditions into a unique environmental chamber. Particles interacting with the injector tube have been seen to become electrified with a relatively narrow range of surface charge concentration (σ) around $\pm 100 e/\mu m^2$ ($\approx \pm 0.02 mC/m^2$) for all particle sizes in the range $1-8\mu m$. Explanations for this effect are discussed, including the possibility of field emission at the contact site limiting the surface charge concentration. In a second measurement technique the voltage on the injector system (i.e. a Faraday tube) was measured during aerosolization in order to investigate the size and composition dependence of the charged particles leaving the injector tube. Again the net charge was seen to increase linearly with the total particle surface area, in agreement with σ values determined using the laser-based technique. Studying the composition dependence of contact electrification a simple new physically meaningful model has been put forward based on electron transfer: in the case of insulating oxides a linear correlation was found between σ and the absolute generalized relative electronegativity (χ_{AGR}), obtained by knowing the composition of the contacting surfaces; $\sigma = a\chi_{AGR} - b$, where $a = 4.7 e/\mu m^2/V$, $b = -27 e/\mu m^2$. This predictive model may be used for estimating the magnitude of contact charging, and was seen to give reasonable agreement with observed contact electrification of volcanic ash samples, when treated as silica. For metals the charge was observed to correlate with electron work function as well as electronegativity, though with limited accuracy. The contact electrification process was not seen to be greatly affected by gas composition. Also the effects of relative humidity, particle aggregation (cohesion), adhesion to the injector tube wall and gas breakdown were investigated.

This work is hoped to advance our understanding of contact electrification and put forward new challenges for future research.

Acknowledgement

I would like to express my sincere gratitude to my advisors, Prof. Jörn Sesterhenn and Jon Merrison, for the possibility they had given me and for all their support during my research. During this period I have learned a lot and improved as a researcher. I would also like to thank Jens Jacob Iversen, for being such a great support both scientifically and as a lab technician. I have been really lucky to be able to work with all of you, thank you and Jon for all the great time spent together in the lab.
I also want to thank my family for always supporting me and all my decisions. My mum, my dad, my brother, my sister in law and my two wonderful nephews. You are awesome.
Also, my special thank goes to all the VERTIGO crew (both ESR's and Supervisors) for everything they have taught me about volcanology, a field I did not know before and that has revealed being incredibly fascinating. I will never forget all the workshops, summer schools and field work we did together, combining fun and hard work.
Thank you also to all my colleagues of the "Computational Fluid Mechanics" department that I met during my PhD, for their help, support and fruitful discussions.
Last, but not least, a big thank you goes to all the friends I have met along the way during these 3 years. It has been an incredibly stimulating period of my life, and this is also due to the strong relationships I was able to build during these years with incredible people, who contributed broadening my way of thinking. They have also been of immense support during the toughest periods of my PhD. When writing names there is always the risk of forgetting someone, but you will forgive me: thanks to Paolo Lamagni, Matteo Miola, Chiara De Notaris, Jacopo Catalano, Luca Bordoni and Bartolini, Carina, Christel, JB, Steffen, Niki, Robert, Julian, Ben, Antonis, Thomas, all the Murgueros, Caterina and generally everyone that has been close to me during these years. And I feel it is important to acknowledge also my dear friends which accompanied me during my Bachelor and Master degree: without you I know I would not have been able to reach this result.

Now it is the moment to start a new adventure.

Thank you, by heart, to all of you.

CONTENTS

LIST OF FIGURES

LIST OF TABLES

CHAPTER 1

INTRODUCTION

1.1 Contact electrification

When the surfaces of two materials get in contact, a certain amount of electrical charge is usually transferred from one surface to the other, as a result of what is called *contact electrification*.
Despite being firstly observed in the antiquity by Thales of Miletus in his experiments rubbing amber against wool [1] and having been widely studied in the last century, there are still uncertainties upon the most basic mechanisms of charge transfer: is it due to electron transfer? Or are ions being transferred instead? Can it be due to bits of material transferred between the two surfaces? What is the role played by the chemical composition and size scale of the two materials? How does the surrounding gas and surface water layer influence the charge transfer? Currently there is no universally accepted physical model explaining this process. Even the terminology regarding particulate electrification is a source of confusion: contact electrification and tribo-electrification are often interchangeably used in literature. Conventionally, contact electrification is referred as "contact and macroscopic separation leading to charge transfer" [2], while tribo-electrification puts emphasis upon the dependence on composition (as in the purely empirical triboelectric series) [2].
The purpose of this study is to experimentally investigate this physical phenomena focusing on aerosolized micron-scale solid particles, using novel precision techniques in order to determine a dependence upon particles length

scale, their chemical composition and the surrounding gas properties.
Contact electrification in fine solid particles are studied here because of their relevance in a wide range of practical problems/applications. In industry, powders can become electrically charged and several phenomena can occur: in fluidized beds or pneumatic transport lines charged particles can agglomerate and adhere to the walls, thus reducing the efficiency [3–5]; high electrification degree may cause discharging, inducing explosions or fire; pharmaceutical powders can also become charged when flowing during processes, causing issues related to agglomeration and non homogeneous dosages [6,7]. Also, many applications have been developed involving controlled charging of powders: examples are electrophotography [8], electrostatic powder coating [9], controlled powder flow rate [10], the development of an 'electromechanical valve for solids' [11] or promising new methods such as triboelectric separation for granular plastic waste recycling [12]. Contact charging may represent an hazard in space applications, e.g. due to intense electric fields generated in dust storm/dust devils, as it can damage electronic equipment via discharging or deplete their functionality [13–16]. Geologists also face situations related to contact charging: in volcanology, explosive eruptions are seen to generate lightnings within the volcanic ash plume [17, 18] and high charge densities associated with electric potential gradient have been measured in volcanic plumes [19, 20]. The dominant charging process for volcanic ash has been associated to fractoemission from fresh crack surfaces as a result of material fracture [21]. Electrostatic forces may play a relevant role in wind-driven dust resuspension processes, e.g. enhancing or depleting adhesion forces between dust/sand particles in deserts [15] or volcanic ash deposited subsequently to an eruption [22].

Despite being relevant in such various fields, our understanding of contact electrification is still poor: in literature several different experimental works are present, but there is often little agreement upon the mechanisms of charge transfer and inconsistent results are reported upon the magnitude (and sometimes even the polarity) of the charging process [23, 24]. The most basic approach for predicting the direction of charge transfer is based on the use of the triboelectric series, an entirely empirical ordering of materials based on their tendency to acquire a negative/positive charge. However triboelectric series are not reliable: an example contradicting the triboelectric series is the observation of cyclic triboelectric series [25], or the contact charging happening with two chemically identical materials [23]. Also, the triboelectric series has been shown not to be entirely reproducible, with different experiments determining different ordering of materials [23]. There are in fact many different

factors that may affect the reproducibility of an experiment: for example, the material surfaces often present impurities like dust particles on large surfaces, or defects at a nano/micro scale on fine powders, which can affect the magnitude of contact charging [26]. Generally, chemical-physical surface properties and environmental conditions play an important role [24, 25].
Focusing on dust (micron-sized) particles represents an additional complication, as it gets more difficult to study individual particles. However, understanding contact charging of such materials is fundamental due to its practical relevance, even for non-pure surfaces and irregular/unknown shapes: as Harper writes in his influential review, "*it must not be forgotten that the technologists may be more concerned, in the field of static charging, with the behaviour of dog food, for example, than with that of super-pure germanium*" [26].
Understanding how a material can acquire a net charge after contact requires understanding what species was transfered, the mechanism driving the transfer and the reason why such transfer came to an end [26]. Clearly, a complete picture of such process would require a deep use of quantum theory of solid state, whether for practical applications a classical approach may be enough for interpreting experimental results and derive a size and composition dependence upon the magnitude of charge transferred, as it will be done in this thesis.

It is well known that electrically conducting or insulating materials behave differently. In metals, electrons are free to move as their valence and conduction band overlap, and transfer of electrons happens in partially-filled (conduction) bands; in insulators electrons are not free to move as they have a high band gap, and electrons are normally not able to jump from the valence to the conduction band.
It is widely accepted that contact charging in metals is due to electron transfer, and the amount of charge transferred is linearly dependent on the electron work function ϕ of the two contacting surfaces [26, 27]: when two metal surfaces get in contact, the Fermi levels of both metals come to the same energy and electrons are transferred from the material with the lower to the one with the higher work function. The contact potential difference between the two surfaces is expressed as [24]:

$$V_c = -\frac{\phi_1 - \phi_2}{e} \tag{1.1}$$

where ϕ_1 and ϕ_2 are the work function values and e is the electron charge. The amount of charge transferred can be approximately calculated using the

following relation [24,26]:

$$\Delta q = C_0 V_c \tag{1.2}$$

where C_0 is the capacitance between the two bodies at the critical cut-off distance for charge transfer (i.e. the separation between the two surfaces after contact). Recently Peljo et al. [28] investigated the Fermi level equilibration after contact charging, to understand how much charge is transferred and where it is located. They showed that most of the charge transferred is retained at the interface as a dipole, and that the charge at the outer surfaces is inducing a potential difference which is equal to the difference in work function between the two materials. They also discussed the influence of the contacting surfaces geometry over the net transferred charge.
However, work function values found in literature may vary substantially due to the experimental techniques used to measure it, the presence of an oxide layer on the surface [24] and also because they have a dependence on crystal orientation [29]. In the work of Harper [26] and Lowell [27] a linear correlation between charge and work function for several metals was attained only after measuring directly the work function of the contacting surfaces used in their experiments [26]: this is somehow self consistent, because measuring the work function as a contact potential difference already implies that charge has been transferred to equalize such contact potential.

For insulators the picture is far more complicated, as electrons are not free to move: when a net negative charge is found over the surface of an insulator it is not clear whether it is due to an excess of electrons or negative ions; conversely, a positive charge may be due to a deficit of electrons or an excess of protons. Three alternative processes are debated to be responsible for contact electrification in insulators:

1. Electron transfer
2. Ion-material transfer
3. Ion-contaminant transfer

A brief review of these models is presented in the following subsections.

1.1.1 Electron transfer models

For explaining electron transfer in insulators, it is useful to start with the case of contact electrification between a metal and an insulator: some work has been done trying to derive an 'effective work function' for insulators [30] as a

function of the charge exchanged when in contact with a metal, trying to ascribe the charge exchange mechanism to a physical process similar to the well understood metal-metal contact [24]. The main criticism moved to these models is that electron transfer is energetically not plausible, as in insulators the distance between the valence band and the conduction band (i.e. band gap) is much larger than the available thermal energy $k_B T$ (k_B is the Boltzmann constant and T is the temperature) [23, 25]. Also Harper [26] in his review claimed that for insulators the charge carriers are never electrons, and put forward an ion-transfer mechanism. To answer this criticism, originally Lowell and Rose Innes [31] in their review introduced the theory that non-equilibrated electrons in trapped states within the band gap may be responsible for the charge transfer in insulators. From thermoluminescence and phosphorescence measurements [32, 33] there is an evidence for the existence of these non equilibrated electrons in insulators [33], although there is still uncertainty about the origin and nature of these trapped states [23]. Such electron states are assumed to be localized at the surfaces and directly relate to the effective work function [34]. Duke and Fabish [35] proposed a 'molecular ion-state model', suggesting that electron states in a polymer are spread over a wide range of energy: these polymers have donor and acceptor states, and electrons can be transferred via tunneling into a narrow range of energy around the Fermi level of the contacting metal or, when contact is between insulators, charge is transferred in an energy window between the centroids of the two energy distributions of the two insulating materials [24, 35]. Waitukaitis et al. [36] demonstrated that, in the specific case of contact between two identical surfaces, the surface density of trapped electrons is not enough to account for the observed charge transfer.
Quantum chemical calculations have also been performed supporting electron transfer, [37], and also other recent experimental and numerical work supports the electron transfer mechanism in insulators [38–40].
McCarty and Whitesides state that experimental observations appear to go against the electron-transfer model, as it "*does not correlate with bulk electronic properties, such as the dielectric constant, or atomic properties, such as ionization energy, electron affinity or electronegativity*" [25, 41]. However, there are other experimental works that contradict this view relating contact charging with electronegativity [42, 43], as well as our results in Section 4.1.

1.1.2 Ion-material transfer models

In the special case of ionic materials (i.e. materials having covalently bonded ions and mobile counterions) charge transfer is thought to be possible in the

form of mobile ions [25]. This mechanism was well explained in the review from McCarty and Whitesides [25]: they proposed a model in which mobile ions at the surface may move from one surface to another due to thermal activation by surmounting a potential energy barrier. When the two surfaces are sufficiently distant apart, the potential barrier is high enough to kinetically trap ions on the surfaces. They also extensively showed experimental evidences of how ion transfer happens when mobile ions are present on the surface of insulating materials [25]. In the reviews [23, 25] the transfer of mobile ions characteristic of certain material surfaces is named 'ion transfer', here this mechanism is referred as 'ion-material transfer', since the transferred species directly comes from the ionic material and therefore it can be considered as a form of what is generally called 'material transfer'.
In the work of Baytekin et al. [44], Kelvin Force Microscopy (KFM) was used to image surface potentials of various contacting surfaces after separation: it was shown how each surface acquired a random "mosaic" of positively and negatively charged regions of nanoscopic dimensions, while still showing a certain net charge. The specific nano-scale regions showed significantly higher values of surface charge concentration than usually observed, whereas the net charge over the entire surface was still within the typical observed limits. Such mosaic has been interpreted as one form of material transfer, "*driven by chemical and micromechanical properties of the material surfaces that are not homogeneous at a nano/atomic scale*" [23] and may be interpreted as broken bonds producing a positive and negative ion pair. Baytekin's work shed light over the possible reason why contact electrification is often so unpredictable, even when the experimental conditions are apparently the same.
In order to avoid confusion, it is worth remarking that the term 'material transfer' is also more generally referred as the transfer of relatively large material fragments from one surface to another [23], typically as the result of friction: in literature it is often considered as an additional effect and not as a primary source of electrification [24, 26, 31]. However, the two definitions may be considered equivalent, since material transfer as a charge carrier is the effect of bonds breaking [23] and, in fact, the transfer of ions resulting from it.

1.1.3 Ion-contaminant transfer models

In normal atmospheric conditions all surfaces have contaminants that may come from surface impurities, water layer or the surrounding gas. These contaminants might be transferred from one surface to another in the form of ions, thus carrying charge. The most common and widely present surface contaminant is adsorbed water, and it appears that it may play an important

role in the electrification of certain materials. Hydroxide ions (OH^-) are often seen to accumulate at water/solid interfaces [25], segregating from cations (H^+) that are left in solution. A similar phenomena is observed for ionic materials contacting through water bridges, forming an electrical 'double layer' between immobile cations at the surface and mobile anions in solution. The electrical potential at the double layer interface is defined as 'zeta potential', and has been seen to correlate with contact charging [25]. Here this process is defined 'ion-contaminant transfer', as it requires the presence of a third element (i.e. the contaminant, in this case water) to transfer charge between two surfaces, whereas ion-material transfer can also happen in the absence of water (or other surface contaminants).
However it is not clear yet why contact charging is sometimes seen also for surfaces under extremely dry conditions, suggesting that ionic and non ionic materials may exchange charge differently, possibly with different species being transfered (electrons and/or ions). Surfaces in a gaseous environment may form contacts through water-bridging due to the ambient humidity. In the work of Pence et al. [45], mobile ion-containing polymers showed almost no charge for relative humidity $RH \approx 0\%$ and increasing charge up until $RH = 30\%$, with subsequent decrease for $RH > 40\%$, suggesting that water is necessary for the transfer of mobile ions; conversely Nieh and Nguyen [46] observed increasing charge towards low RH for glass beads (which do not contain mobile ions) flowing in a copper pipe. Also our study (Section 5.4) indicates that high contact charging is measured with oxides at extremely low RH ($\ll 1\%$). Such discrepancies again indicate that surface properties also play an important role.

We may state at this point that the picture is far from being clear: lacking general agreement, one likely explanation is that electrons and/or ions can be transferred depending on the material properties, environmental conditions and contact mechanisms.

1.1.4 Contact charging with particles of the same composition

It has been observed experimentally [2, 16, 36, 47–51] that in chemically identical contacting surfaces small particles tend to acquire a negative charge and bigger ones a positive charge. Lacks and co-workers suggested that this phenomenon might be due to the presence of trapped electrons in high energy states [50, 52], similarly to the idea presented by Lowell and Truscott [33]. However it has been demonstrated that the surface density of trapped electrons is not enough to explain the observed electron transfer following the trapped-

electron model [36], suggesting that ion transfer is the driving mechanism. In a recent work the electrification in same-particle contacting has been studied as a function of the air relative humidity [53], the results showed that this phenomenon is substantially depleted at high RH, essentially disappearing at $RH \approx 50\%$. It has also been recently shown that two identical (in composition and size) polytetrafluoroethylene sheets contacting together usually led to a random direction of charge transfer, but when one of the two samples was subjected to plastic deformation they were systematically charged in one direction [54]. The authors interpreted these results as to be due to macroscopic formation of voids (from nm to mm in size) and not to changes in the molecular structure of the material.

1.1.5 Magnitude of the measured contact electrification and limiting mechanisms

Despite such uncertainties over the mechanisms of charge transfer, in many different experimental work general agreement is found over the order of magnitude of the maximum charge concentration that a particle surface can attain (usually ranging from $0.01 - 0.1 mC/m^2$) [14, 33, 55, 56]. Such a limit is often calculated dividing the charge by the total particle surface area (typically assumed to be spherical even for irregular shapes for simplicity). However, some researchers have attempted to estimate the effective contact area relying on simple models [57], as the charge is obviously exchanged at the contact site and, in insulators, is assumed not to be readily redistributed over the entire particle surface.
In the work of Oguchi and Tamatani [42] a linear relationship was found between a 'generalized electronegativity' χ_G and the measured contact electrification seen with oxide (shown in Fig. 1.3), fluoride, and sulfide particles. The concept of generalized electronegativity is explained in Section 1.1.6. Their interpretation of the observed dependence was based upon ion exchange, i.e. on the acid-base properties in aqueous or gaseous phase. They also observed increasing charge-per-mass with the reciprocal of particle size ($1/r$) with r the particle radius (Fig. 1.2): this implies that a specific (mean) surface charge concentration is generated (as shown in Section 2.5). Interestingly, there is extremely good agreement between the results found in [42] and this work, as it will be discussed in Section 6.4.
In the work of Merrison et al. [16] surface charge concentration values within the expected limits $0.01 - 0.1 mC/m^2$ and approximately equal number of negatively and positively charged grains were seen, independently of the sample composition.

Repeated impacts of particles have been seen to increase the surface charge concentration. For example a large synthetic rubber sphere (31mm) impacting repeatedly against a metal plate showed increasing charge exponentially reaching a plateau [58]; similar behaviour has been observed for a large population of fine particles [10], or for large surfaces [59,60].
In [57,61] a dependence upon the impact velocity of particles (pharmaceutical powders and glass beads, $\approx 500\mu m$) colliding against a reference surface was observed.
This general agreement over the order of magnitude of surface charge concentration presumably has to be due to a limiting mechanism: for example electrical breakdown through gas between two surfaces can happen when the electric field is high enough according to the Paschen curve (Fig. 1.1), as it has often been observed experimentally [62–64]. Alternatively, even in the absence of gas at extremely high electric fields ($> 10^9 V/m$) electron field emission may happen after separation of two contacting surfaces [25,26].
Inside a material when high surface charge concentrations are present, the high electric field may cause the dielectric breakdown of the insulating material (e.g. around $3 \cdot 10^7 V/m$ for SiO_2). In this case, the material cannot be considered anymore as a classical insulator [65]. A phenomenon of this type is sometimes referred as *lateral charge spreading*.

As an interesting remark, here is quoted the epilogue of the influential Lacks review who perfectly depicted the difficulties found by researchers when studying contact electrification: "*The first studies on contact electrification were carried out over 2500 years ago, when experiments showed that rubbing amber and wool caused the two materials to become oppositely charged. Our scientific understanding of contact electrification has not progressed very far in the intervening 2500 years—it is still not known what species is being transferred between the wool and amber to generate the charge, and how rubbing influences the process. A review paper such as this often concludes with a discussion of open questions, but we feel that virtually all questions involving electrostatics are in fact open questions. Hopefully, more progress will be made in the next 2500 years*" [23].

1.1.6 Electronegativity

The definition of electronegativity (χ) is the tendency of an atom or ion to attract electrons, and represents its energy change (E) with the change of electron number (N); $\chi = -dE/dN$ [68]. It quantifies the bonding energy between atoms or molecules, as it expresses the affinity that an atom/ion has

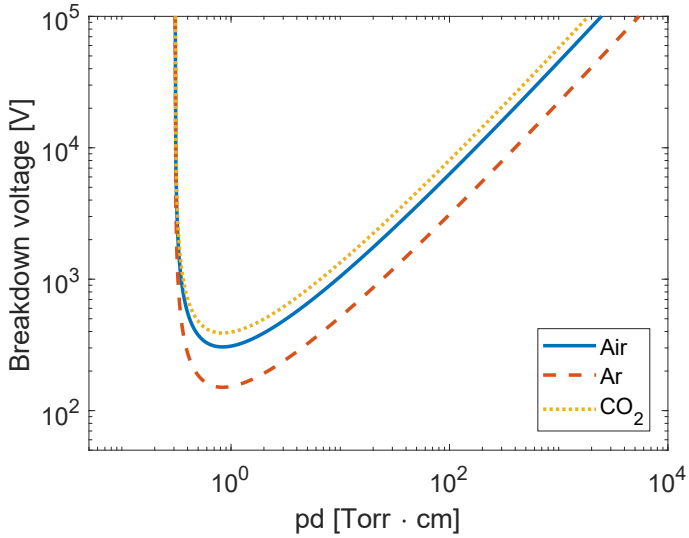

Figure 1.1: Pashen breakdown curve estimated for air, Ar and CO_2, following the Paschen's law: $V_B = \frac{Bpd}{ln(Apd) - ln[ln(1+1/\gamma)]}$. The A, B constants are taken from [66] and [67]; $\gamma = 10^{-2}$ is kept constant due to the lack of data in literature.

for electrons. In atoms, electronegativity is typically expressed in the non-dimensional Pauling's scale (χ_P) relative to Hydrogen, and is known for most elements [69].
Two years after Pauling, another expression in an absolute scale was developed by Mulliken, also called 'absolute electronegativity'. It is the mean of ionization potential and electron affinity expressed in energy per unit charge (kJ/mol or eV/e). Its physical meaning is "*the energy change which accompanies the removal or addition of one electron*" [68], but differently from Pauling's scale is not known for all elements as electron affinity is in some cases unknown. However, as the two magnitudes are closely related, empirical relations have been developed linking Mulliken's and Pauling's electronegativity. In [70] a linear transformation is presented:

$$\chi_M = (\chi_P - 0.03)/0.322 \tag{1.3}$$

Where χ_P is the electronegativity expressed in Pauling's units and χ_M is in Mulliken's scale.
Iczkowski & Margrave [68] and Tanaka & Ozaki [71] extended the concept of electronegativity to describe molecules and ions by including valence: this

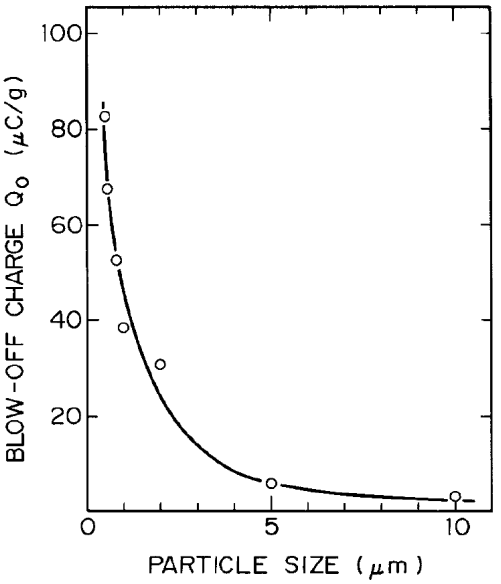

Figure 1.2: Specific charge measured for Al_2O_3 powder sorted in different mean particle sizes. Figure reprinted with permission from the work of Oguchi and Tamatani, 1986 [42].

quantity, named 'generalized electronegativity' (χ_G), represents the electronegativity of an atom in a molecule:

$$\chi_G = (1+2Z)\chi \tag{1.4}$$

Where Z is the valence of the element bound in a molecule.
This generalized expression in Eq. 1.4 can then be applied for two surfaces in contact, i.e. the relative electronegativity between two materials: using Mulliken's scale, this leads to an expression which we named 'absolute generalized relative electronegativity' (χ_{AGR}):

$$\chi_{AGR} = (1+2Z_1)\chi_{M,1} - (1+2Z_2)\chi_{M,2} \tag{1.5}$$

Where $\chi_{M,1}$ and Z_1 refer to surface 1 and $\chi_{M,2}$ and Z_2 refer to surface 2.
χ_{AGR} can be physically interpreted as a contact potential difference. As will be shown in this work there is an experimental dependence of this quantity upon the observed contact electrification (see Section 4.1). This may then lead to the development of a physically meaningful predictive model for contact electrification also in insulators based upon electron transfer, as it will be

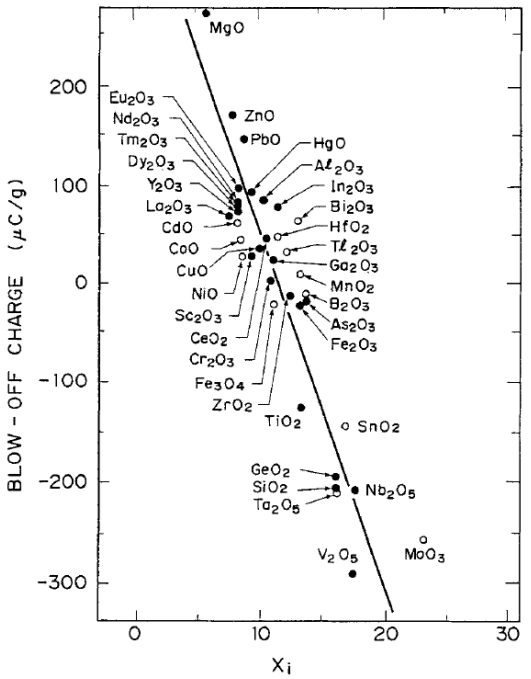

Figure 1.3: Specific charge measured for a set of oxide powders as a function of generalized electronegativity expressed in Pauling units. Figure reprinted with permission from the work of Oguchi and Tamatani, 1986 [42].

discussed in Section 6.1. Such close relation between contact electrification and generalized electronegativity (Eq. 1.4) has also been previously observed in the work of Oguchi & Tamatani [42].

1.1.7 Techniques in quantifying contact electrification

Several experimental techniques have been developed through the years to measure contact charging. While many of the studies found in literature deal with contact of large surfaces, here the focus will be on the experimental techniques and main results obtained in measuring fine particles (µm sized) contact charging.
The most common, simple and reliable technique uses a Faraday cage, which is a metal enclosure electrically insulated, here a charged particle entering or exiting the cage induces an image charge in its inner wall. When the Faraday cage is connected to an electrometer/oscilloscope, the mirrored charge

on the outer wall flows to ground generating a current which is measured to determine the inner charge. Faraday cages have been used in various geometries: particles electrified after contact with a reference plate were collected in Faraday cups [43], or as an array of through-type Faraday cage connected to fluidized beds [72]. The Faraday cage principle was also used to measure the charge of single particles before and after impact against a reference target [57, 61].
Electric fields have often been used in order to separate particles depending on their charge. An electrode collection system was employed by applying an uniform DC electric field to collect aerosolized dust particles [16]. Laser Doppler velocimeter [73] and high-speed imaging [51] have also been used to measure the velocity of oscillating particles under DC electric fields. In particular in [36] a free-falling camera imaged a bimodal distribution of charged particles falling under vacuum and drifted by an electric field, measuring a relatively low charge (around $10^6 e$ for particles ranging from 250 to 320 µm). In a similar electric field-based separation system, contact electrification is measured using Faraday cup collectors, where particle are electrified blowing compressed air through a particle bed ('fountain' technique) in order to investigate particle-particle contact charging, and trying to eliminate every particle-wall interaction [47, 48, 53].
A technique similar to that used in this thesis is found in the work of Oguchi and Tamatani [42, 43]: they used a 'blow-off' aerosolization method in which large reference particles (iron oxide $44-74\mu m$, aluminium $74-149\mu m$, quartz $250-840\mu m$) were placed on a stainless steel mesh, and smaller particles (typically around 0.4µm in diameter) were blown using compressed nitrogen against the reference ones. Small particles could pass through the mesh sieve/filter and were collected in a Faraday cup connected to an electrometer to measure the total developed charge, while the reference material stayed on the mesh filter.

1.2 Multiphase flows

The experimental techniques utilized in this project are based upon the aerosolization of micrometer-sized particles into a large environmental chamber. The aerosolization takes place with the rapid decompression of a gas reservoir into the low-pressure chamber through a long pipe, which disperses (aerosolizes) the particles. A particle-laden flow is typically called a multiphase flow [74] (in this case the term particle is referred to solid powder, but it can be also liquid droplets in a gas flow or gas bubbles in liquid flow). The particles elec-

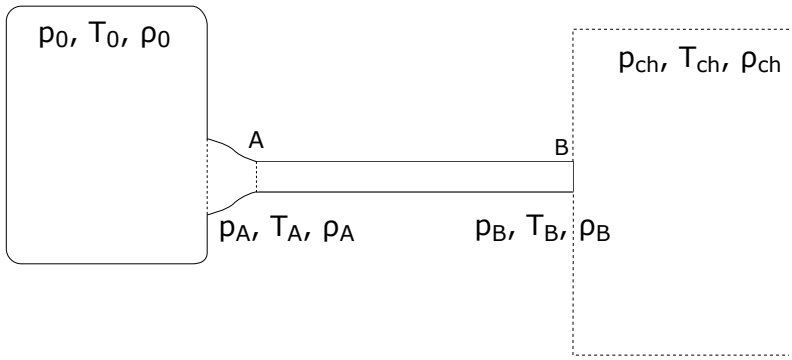

Figure 1.4: Schematic drawing of the setup: reservoir quantities are characterized by the subscript $_0$, tube entrance by subscript $_A$, tube outlet $_B$, and chamber (ambient) values $_{ch}$.

trification mainly takes place when they interact/contact with the aerosolizing tube. For this reason, it is necessary here to introduce aspects of the aerosolization (injection) process, analyzing the flow behaviour during decompression within the injector tube and particle interaction with the gas and the injector tube. The gas phase during the injection will be analyzed from a theoretical point of view, followed by a brief introduction to the particle-laden jet forming inside the chamber and the subsequent settling of particles under gravity.

1.2.1 The thermodynamics of the injection process

This subsection deals with the gas decompression from the reservoir and the flow generated in the tube. Here a qualitative analysis of the evolution of thermodynamic variables along the injector tube is presented using a 1D approach. The geometry of the injector system (see Fig. 1.4) consists of a gas reservoir (characterized by the subscript $_0$) connected through a convergent section to the entrance of the injector tube (subscript $_A$) with a constant diameter. The exit of the injector tube (subscript $_B$) is connected to a large chamber (subscript $_{ch}$) where pressure p_{ch}, temperature T_{ch} and density ρ_{ch} can be considered constant far away from the flow perturbation. It is assumed that the chamber pressure is much lower than the initial reservoir pressure ($p_{ch} \ll p_{0i}$).

The Mach number M is a dimensionless number defined as the ratio be-

tween the flow velocity U and the local speed of sound:

$$M = \frac{U}{\sqrt{\gamma RT}} \tag{1.6}$$

where $\gamma = c_p/c_v$ is the ratio of specific heats at constant pressure and volume and R is the specific gas constant.
The Reynolds number Re is defined as the ratio of inertial to viscous forces, and relatively to the tube section is expressed as:

$$Re = \frac{\rho UD}{\mu} \tag{1.7}$$

where D is the tube diameter and μ is the dynamic viscosity.

The flow expansion in the (short) *convergent section* from the gas reservoir to the tube entrance, may be considered isentropic [75]. Pressure, temperature and density at the tube entrance (subscript $_A$) with respect to reservoir values (subscript $_0$) are expressed as a function of the tube entrance Mach number M_A using the isentropic gas expansion relations:

$$\frac{p_0}{p_A} = \left(1 + \frac{\gamma - 1}{2} M_A^2\right)^{\frac{\gamma}{\gamma-1}} \tag{1.8}$$

$$\frac{T_0}{T_A} = \left(1 + \frac{\gamma - 1}{2} M_A^2\right) \tag{1.9}$$

$$\frac{\rho_0}{\rho_A} = \left(1 + \frac{\gamma - 1}{2} M_A^2\right)^{\frac{1}{\gamma-1}} \tag{1.10}$$

The *tube section* may be treated as a Fanno flow [76], where viscous friction due to shear stress at the wall changes the thermodynamic properties along the tube. A Fanno flow is based under the assumption of an ideal gas, adiabatic flow, quasi-1D and quasi-stationary flow, neglecting gravitational forces. The Fanno model applies to both incompressible/compressible and subsonic/supersonic conditions.

The Fanno line on the Gibbs plane relating entropy and enthalpy has the following (dimensionless) form:

$$\frac{\Delta s}{c_p} = ln\left[\left(\frac{1}{H} - 1\right)^{\frac{\gamma-1}{2\gamma}} \left(\frac{2}{\gamma - 1}\right)^{\frac{\gamma-1}{2\gamma}} \left(\frac{\gamma + 1}{2}\right)^{\frac{\gamma+1}{2\gamma}} H^{\frac{\gamma-1}{2\gamma}}\right] \tag{1.11}$$

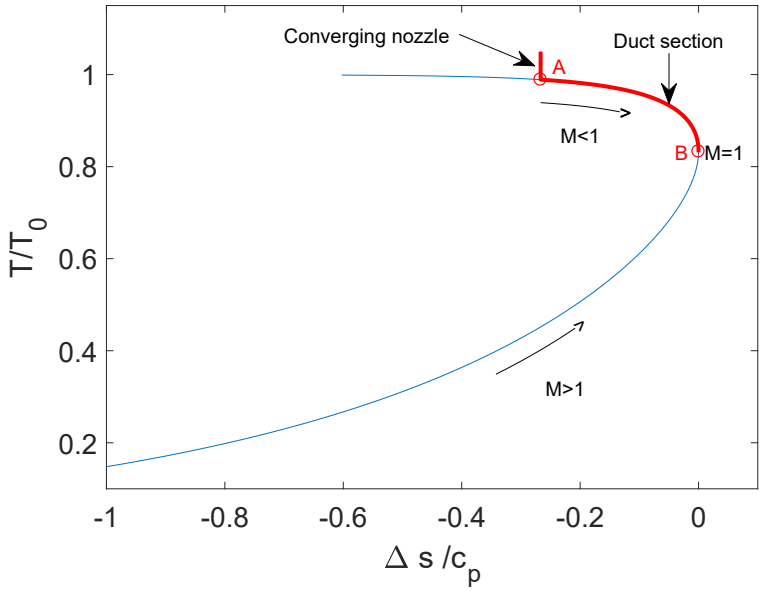

Figure 1.5: Fanno line (in blu), from Eq. 1.11. The vertical (isentropic) red line represents the fluid thermodynamic transformation along the short converging section connecting the reservoir and the tube. The flow in the tube section follows the Fanno line (from point A to point B) increasing its Mach number eventually until choked conditions are reached (if the tube is long enough).

where $H = c_p T / c_p T_0$ is the dimensionless enthalpy ratio, with T the temperature along the tube and T_0 the reservoir temperature. The Fanno line, plotted in Fig. 1.5, shows that a subsonic flow entering a tube with friction will have an increase in its Mach number. Conversely the Mach number of a supersonic flow will decrease as effect of viscous friction. In both cases, $M \to 1$ (choked condition). The flow may eventually become choked only at the end of the tube due to viscous friction effect, if the tube is sufficiently long enough. This phenomenon is sometimes referred as 'friction choking'.
In Fig. 1.5 the isoentropic flow in the (short) converging section is shown with a vertical red line, whereas by moving on the Fanno line entropy increases between the tube entrance (A) and exit (B), until choked conditions are reached.

The Fanno relation (Eq. 1.12) expresses the change in Mach number M along the tube axis dx ($x = 0$ is the tube entrance, $x = L^*$ is the tube exit) ac-

cording to the following relation [76]:

$$\frac{M^2-1}{\gamma M^2\left(1+\frac{\gamma-1}{2}M^2\right)}\frac{dM^2}{M^2}=-4f\frac{dx}{D} \tag{1.12}$$

where f is the Fanning friction factor. The friction factor is a function of the flow Reynolds number and the tube's relative roughness.
From Eq. 1.12 it can be seen that if the flow in a generic tube's section is subsonic ($M<1$) then $dM/dx>0$ and vice versa. As the nozzle is purely convergent, the flow entering the tube must be subsonic and accelerate along the tube, eventually reaching choked condition ($M=1$) only at the tube exit. $M=1$ at the tube exit is reached if p_0/p_{ch} is above than a certain critical value depending on the tube length L, diameter D and friction factor f. When choked conditions are reached, $p_B>p_{ch}$ and the tube exit can be considered underexpanded generating a supersonic jet [77]. Supersonic expansion will take place in the vicinity of the tube exit allowing the pressure to match with the chamber pressure. When p_0/p_{ch} drops below the critical value, the flow becomes subsonic and the pressure at the tube exit nearly equal the ambient pressure $p_B\simeq p_{ch}$. This condition applies because large pressure differences cannot occur over small distances in a subsonic flow.

The Reynolds number along the tube (Eq. 1.7) can be estimated from the initial condition, assuming choked flow at the tube exit. From the Moody's chart, depending on the tube's relative roughness and Reynolds number, a Fanning friction factor f is obtained. Eq. 1.12 is then solved between a generic Mach number and the critical Mach number ($M=1$) at the tube outlet, in order to find the Mach number at the tube entrance ($M_{x=0}=M_A$) as a function of a critical length L^* (i.e. the real experimental tube length):

$$\frac{4fL^*}{D}=\frac{1-M_A^2}{\gamma M_A^2}+\frac{\gamma+1}{2\gamma}ln\left(\frac{\frac{\gamma+1}{2}M_A^2}{1+\frac{\gamma-1}{2}M_A^2}\right) \tag{1.13}$$

Pressure, temperature and density at the tube entrance (subscript $_A$) are calculated with respect to reservoir values (subscript $_0$) using Eq. 1.8, 1.9, 1.10 knowing the entrance Mach number M_A from Eq. 1.13.
p_A, T_A, ρ_A can then be used to calculate the exit (choked) values p_B, T_B, ρ_B and their evolution along the tube by using the following relations valid for the Fanno flow along the tube axis x [75]:

$$\frac{p(x)}{p_B}=\frac{1}{M(x)}\sqrt{\frac{\gamma+1}{2}\left(1+\frac{\gamma-1}{2}M(x)^2\right)^{-1}} \tag{1.14}$$

$$\frac{T(x)}{T_B} = \frac{\gamma+1}{2}\left(1+\frac{\gamma-1}{2}M(x)^2\right)^{-1} \tag{1.15}$$

$$\frac{\rho(x)}{\rho_B} = \frac{1}{M(x)}\sqrt{\frac{2}{\gamma+1}\left(1+\frac{\gamma-1}{2}M(x)^2\right)} \tag{1.16}$$

For $M_{x=0} = M_A$, $p_{x=0} = p_A$ and p_B is obtained. Same procedure is applied to temperature and density.
Once all the thermodynamic variables are known, the tube Reynolds number can be computed and used to calculate again the friction factor. However, from Moody's chart it can be seen that f approaches a constant value for high Re and relative roughness (i.e. fully developed turbulence).
Whereas p_0, T_0 and ρ_0 change over time as the gas reservoir discharges, Eq. 1.14, 1.15, 1.16 remain valid until the flow is choked at the tube outlet. The initial values are known (p_{0i}, T_{0i} and ρ_{0i}). In order to determine the time evolution of these variables additional hypothesis need to be formulated in the reservoir (e.g. adiabatic or isothermal).
These set of equations will be applied in Section 2.3.1 to the experimental injector system used in this work for a predictive estimate of the gas-phase behaviour (M, p, T, ρ).

1.2.2 Lift/adhesion force balance against the injector tube wall and aggregation/cohesion

Whether a particle lying on a surface in gas flow will be resuspended or will stay attached to the surface depends on the force balance acting on a particle, which in its most simple form is composed by the balance between the adhesion force and the flow-induced lift force (gravity is typically neglected for micron-sized particles as the adhesive force is much larger).
For micrometer sized particles in contact with a surface, determining the adhesion force is challenging and requires sensitive measurement techniques. The most successful one has been atomic force microscopy (AFM), where a sample (e.g. a single particle) is mounted on a cantilever: the tip of the AFM gets in contact with the particle, the adhesive force (F_{adh}) is measured when the cantilever force overcomes the adhesive tip–sample interaction, i.e. the so-called 'pull-off force' [78]. Jones et al. [79, 80] and Heim et al. [81] measured adhesive forces of micrometer-sized particles. Results showed that F_{adh} linearly increases with particle size [81]; the effects of surface roughness and relative humidity are important, and hydrophobic/hydrophilic materials behave differently [79].

Contact between two solid spherical particles is usually described by either the model of Johnson, Kendall and Roberts (JKR) [82], valid for large and soft bodies with high surface energies, or by the Derjaguin, Muller and Toporov (DMT) model [83] which is more accurate for small hard particles with low surface energy and accounts also for non-contact forces in proximity of the contact area. The adhesive (pull-off) force in these two models is written as $F_{\mathrm{JKR}} = 3\pi r\gamma$ and $F_{\mathrm{DMT}} = 4\pi r\gamma$, where r is the particle radius (in case of particle contacting against a much larger surface) and γ is the effective solid surface energy [80, 81].
Semi-empirical models have also been developed [15, 84], where adhesion force F_{adh} is written as:

$$F_{\mathrm{adh}} = 2C_{\mathrm{adh}}r \tag{1.17}$$

with C_{adh} the adhesion coefficient, empirically determined. The adhesion force is typically considered as a combination of van der Waals, electrostatic, capillary and chemical bonds [78], i.e. electrostatics may play an important role, as observed in fluidized beds and pneumatic transport lines (see Section 1.1). Cohesive agglomerates of particles (which in this work will usually be referred as aggregates) are constituted by multiple particles sticking together due to the effect of the adhesive force. Here effects of humidity and electrostatics may be very important.
The flow-induced lift force F_{L} is expressed as:

$$F_{\mathrm{L}} = C_{\mathrm{L}}\rho U_*^2 r^2 \tag{1.18}$$

where C_{L} is the lift coefficient, ρ is the fluid density, U_* is the friction speed [15]. Pitot tube or laser Doppler velocimeter are typically used for measuring the turbulent boundary layer profile, in order to determine the surface shear stress, defined as:

$$\tau_{\mathrm{f}} = \rho U_*^2 \tag{1.19}$$

Experimental determination of the threshold shear stress for particle detachment provide a useful tool in understanding the force balance acting on particles: e.g. in the work of Matsusaka et al. [85] it was examined the undisturbed wind speed necessary for removing a monolayer of micron-sized particles as a function of particle size. In our recent work [22] the effect of humidity and particle size was studied together with high speed imaging of the detachment dynamics.
The friction speed may also be estimated by knowing the undisturbed flow velocity (e.g. at the tube center), using the standard boundary layer theory and

empirically determined constants from [86]:

$$U(z) = U_*(a\ln\left(\frac{zU_*}{\nu}\right) + b) \tag{1.20}$$

where z is the height from the tube surface, ν is the kinematic viscosity, $a = 2.5$ and $b = 5.5$ [86].
The flow shear stress can be compared to the experimentally determined threshold shear stress τ_{th} necessary for particle detachment, using the models developed in Merrison, 2012 [15] and Shao & Lu, 2000 [84]:

$$\tau_{\text{th}} = \frac{2C_{\text{adh}}r}{C_{\text{L}}r^2} \tag{1.21}$$

The two empirical parameters can be approximately estimated as $C_{\text{adh}} \approx 1.5 \cdot 10^{-4}$ and $C_{\text{L}} \approx 160$ [84].
The threshold shear stress and fluid shear stress can be compared in order to predict whether a particle can be resuspended from the injector tube surface by a gas flow. This will be useful when analyzing results in Section 5.2.

1.2.3 The jet

This subsection deals with expansion of the gas at the tube outlet into the low pressure chamber (Fig. 1.4). As discussed in subsection 1.2.1, as long as the tube outlet is choked it can be considered as an underexpanded nozzle generating a supersonic jet [77]. Here the term underexpanded means that the gas pressure could not expand enough to match the ambient pressure. The pressure is then adjusted to the chamber pressure through a series of shock waves and expansion waves, forming the so-called shock cell structure depending on the injector geometry and the pressure ratio between the reservoir and the chamber [77]. The initial pressure release through the tube forms a compression wave at the tube outlet. The large velocity gradients initially generated lead to the formation of a vortex ring, growing until a critical size and successively propagating along the axial direction [77]. The vortex ring detaches from the trailing jet (when present) propagating further, and successive vortices in the shear layer are generated.
The Reynolds number at the tube outlet can be estimated in first approximation using the Fanno flow relations (Section 1.2.1), and in the experimental setup specific for this work depends mainly on the initial reservoir-to-ambient pressure ratio (p_{0i}/p_{ch}). As the chamber pressure is always low ($p_{ch} = 2.5 - 10mbar$), the controlled reservoir pressure determines whether the generated jet will be fully turbulent. Dimotakis [87] reported that $Re > 10000$ is needed

for a fully turbulent jet.
In Section 2.3.2 observations of the experimentally produced jet are discussed.

1.2.4 Settling: Stokes and Epstein (molecular) regime

The terminal settling velocity for spherical particles is reached when the gravitational force $F_g = \rho_p \frac{4}{3}\pi r^3$ is balanced by the drag F_d force of the surrounding gas acting on a particle:

$$F_g = F_d \tag{1.22}$$

Stokes derived a relation expressing the drag force acting on a sphere, valid when the particle Reynolds number Re_p is considerably smaller than 1:

$$Re_p = \frac{\rho_f 2 r U_p}{\mu} \ll 1 \tag{1.23}$$

The particle Reynolds number tends to zero when the particle characteristic length 2r is small, its velocity is low, the surrounding medium has an high viscosity or the gas has a low density.
In this flow condition, also called Stokes flow, the Navier-Stokes equation for incompressible flows can be simplified neglecting the non-linear terms, while the viscous terms are still present: this results in a linear differential equation with an analytical solution. In Stokes flow, only the viscous force is acting on the particle.
Stokes expressed the drag force as:

$$F_d = -6\pi\mu r U_p \tag{1.24}$$

This equation, also called Stokes law, was derived under the assumption that the sphere is rigid, there is steady-flow condition around it and there is no-slip at the sphere's surface.
However, the no-slip condition is valid only while the flow can be considered to be in the continuum regime and it leads to the failure of the Stokes law in rarefied gases, i.e. for gases where the mean free path of the gas λ is larger than the size of the sphere $2r$. This happens when the Knudsen number Kn is larger than unity:

$$Kn = \frac{\lambda}{2r} > 1 \tag{1.25}$$

For $Kn > 1$ the gas can not be considered anymore as a continuum medium, but it rather consists of individual gas molecules colliding with the sphere's surface. This condition is relevant for micron scale aerosols in the upper troposphere, where the air has a low density, and also in normal atmospheric

condition ($p = 1bar$, $T = 293K$) for ultra-fine particulate (e.g. $PM_{0.1}$, namely particles $< 0.1\mu m$), where the mean free path is $\lambda = 67nm$.
Cunningham first proposed a correction factor to Stokes law for non-continuum flows taking into account for slip at the particle surface [88], later modified by Knudsen and Weber. This correction includes 3 empirical parameters (α, β and γ), successively measured by Millikan [89,90]. This is also called Cunningham slip correction factor, given by the expression:

$$C = 1 + Kn\left(\alpha + \beta e^{-\frac{\gamma}{Kn}}\right) \tag{1.26}$$

Epstein in 1924 [91] used kinetic theory to calculate the drag force on a sphere in the free molecular regime ($Kn \gg 1$). This has the advantage of having a physically meaningful expression with only one free empirical parameter δ which expresses the type of surface scattering, i.e. $\delta = 1$ for specular scattering and $\delta = 1$ for diffuse scattering. The drag force was expressed by Epstein with the following equation:

$$F_{\mathrm{d,Eps}} = -\frac{4}{3}\pi\delta r^2 \rho_g \overline{c} U \tag{1.27}$$

where $\overline{c}$ is the mean molecule speed from the Maxwell-Boltzmann distribution:

$$\overline{c} = \sqrt{\frac{8k_B T}{\pi m_{mol}}} \tag{1.28}$$

where k_B is the Boltzmann constant and m_{mol} is the molecular mass of the gas. In the work Alois et al. 2017 [92], differently from Epstein work, $\overline{c}$ has been considered as the root mean square velocity of the gas molecules, following the equation:

$$\overline{c}_{\mathrm{rms}} = \sqrt{\frac{3k_B T}{m_{mol}}} \tag{1.29}$$

with $\overline{c}_{\mathrm{rms}}/\overline{c} = 1.0854$. In this thesis the classical definition from Epstein will be used.
The scattering parameter δ was calculated by Epstein deriving several expressions depending on how the gas molecules were scattered by the surface of the sphere. In this work, an experimentally measured value for the slip parameter $\delta = 1.15$ is used, based on a previous study on settling speed performed by Andreas Boes Jakobsen [93].
By knowing the analytical expression for the drag force in the molecular regime,

the settling velocity as a function of time $U(t)$ can be derived by solving the differential equation:

$$m\dot{U} = F_{\mathrm{d,Eps}} - mg \tag{1.30}$$

where m is the mass of the particle.
By imposing the initial condition $U(0) = 0$, the equation is solved analytically as:

$$U(t) = \frac{mg}{k}\left(1 - e^{-\frac{kt}{m}}\right) \tag{1.31}$$

By writing the particle mass $m = 4/3\pi r^3 \rho_p$, the time constant $\tau = m/k$ gives the expression:

$$\tau = \frac{\rho_p r}{\rho_g \bar{c}\delta} \tag{1.32}$$

and the terminal settling velocity $U_t = mg/k$ is:

$$U_t = \frac{\rho_p g r}{\rho_g \bar{c}\delta} \tag{1.33}$$

Epstein model has been extensively used in this work, as the velocity of particles settling in a low pressure chamber (where $Kn \gg 1$) has been measured using a Laser Doppler Velocimeter (LDV) in order to derive their size (details are shown in Section 2.4).

CHAPTER 2

EXPERIMENTAL TECHNIQUES AND MATERIALS

2.1 Aarhus wind tunnel simulator II (AWTSII)

The main facility that has been used during this project is an environmental chamber named 'Aarhus Wind Tunnel Simulator II' (AWTSII)[1] [94]. It is a recirculating wind tunnel originally designed to reproduce atmospheric conditions (e.g. on the Martian surface), and well suitable for research on aerosols. The facility is a cylindrical vacuum chamber (2.1m inner diameter and 10m length, with a total volume of 35m^3, see Fig. 2.1) and allows precise and independent control over atmospheric parameters, i.e. pressure, temperature, humidity, wind speed and gas composition. Importantly, aerosolized particles can be dispersed in the chamber. The facility is equipped with multiple flanges both on the sides and at the top of the chamber. They can be used for windows, cable connections and for an aerosol injection system (Section 2.3). This allows particles to be aerosolized inside the chamber while simultaneously controlling atmospheric parameters of the surrounding gas. These characteristics make this facility particularly suitable for studies of aerosols and contact electrification, where atmospheric parameters need to be constrained.
The gas composition can be controlled by evacuating the chamber down to a minimum of $\approx$ 0.02mbar and re-filling it with gas until the desired pressure is reached. A capacitance-type pressure sensor (Pfeiffer APR 250) is used to mon-

[1] http://marslab.au.dk/windtunnel-facilities/wind-tunnel/

itor the chamber pressure for pressures above 1mbar, and is independent of the gas composition. For pressures below ≈ 1mbar, a Pirani gauge (Pfeiffer TPR 280) is used: this sensor is accurate at low pressure and has a reliable range of around 0.01 – 100 mbar, though it is specifically designed for air and becomes highly inaccurate when measuring other gases, in particular at pressures above 1 mbar [94].
Humidity can be controlled both in the environmental chamber and in the injector (aerosolizing) system. The chamber is equipped with an Honeywell thin polymer film sensor measuring the relative humidity (RH) [94]. Generally, low humidity ($RH < 2\%$) are reached when using air at the typical working pressure of these experiments (≈ 2.5mbar) due to the low partial pressure of water in the chamber.
The chamber temperature is monitored using Pt100 sensors [94]. Cooling of the gas inside the chamber can be achieved by flowing liquid nitrogen into two cooling plates in aluminium (2m × 1.8m × 5cm for 480kg) constituting the test section, or by using another heat exchanger in aluminum that can be placed inside and removed from the test section, allowing the wind flow to cool down by convection.
A Laser Doppler Velocimeter (LDV) (see Section 2.4) is used to measure dust particles velocity, and is suitable also to measure the flow velocity for dust particles that are coupled with the flow.
It is possible to operate a high speed camera within the AWTSII using a small (length: 42cm, diameter: 25cm) pressurized chamber, connected to a flange through two tubes allowing cabling and ventilation.
The facility has been extensively used when performing experiments with the LDV-based technique (Section 2.4) and the Faraday tube technique (Section 2.5).

2.2 Aarhus Wind Tunnel Simulator I (AWTSI)

The 'Aarhus Wind Tunnel Simulator I' (AWTSI) is an earlier prototype of the AWTSII developed at Aarhus University [95]. It can control environmental conditions similarly to AWTSII (i.e. pressure, temperature, humidity, gas composition) and can be equipped with the same aerosolizer system described in 2.3. The chamber (see Fig. 2.2) is around 0.8m wide and 3m long, with a cylindrical central wind tunnel (0.4m in diameter and 1.5m long) and a total volume of $\approx 1.3 m^3$. It can be evacuated down to ≈ 0.03mbar.
Some of the experiments performed in this chamber needed a control over relative humidity (Section 5.4): low RH ($\ll 1\%$) could be achieved by filling

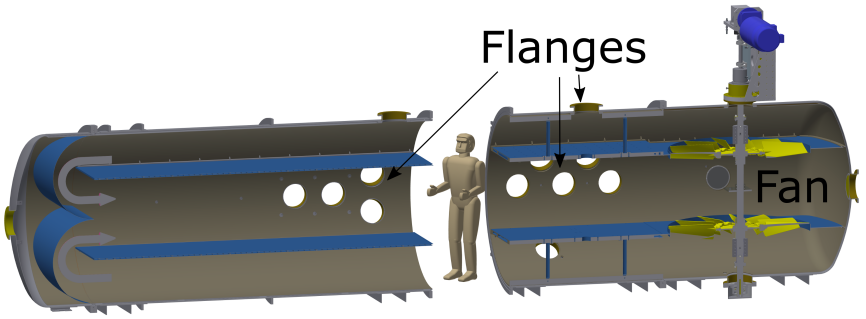

(a) 3D CAD of AWTSII

(b) Picture of AWTSII

Figure 2.1: 3D CAD of AWTSII (a) and a picture of it (b).

the chamber with dry gas (e.g. Argon); high relative humidity (e.g. $RH \approx 50\%$) was achieved by evacuating the chamber ($p < 0.05$mbar) and re-filling it with the desired partial pressure of pure water vapor, from which RH can be determined at room temperature (20°C). This facility has been extensively used for experiments using the Faraday cage technique (2.5), while the LDV technique (2.4) requires the use of the AWTSII (2.1) due to its bigger volume allowing settling of particles.

2.3 The aerosolizing system

An aerosolizing injector system has been developed in order to disperse a mass of particles into the environmental chamber (AWTSII or AWTSI). This was used for investigating the contact electrification generated after particle/particle and particle/wall (i.e. the internal surface of the injector tube) contact. The aerosolization process was achieved by the rapid decompression of a small ($\approx 24\text{cm}^3$) gas reservoir into the environmental chamber. The gas passed through the injector tube (4mm internal diameter, 500mm long) aerosolizing around 10 – 15mg of the sample (Fig. 2.3).
An injection cycle was began by placing the powder sample into the T piece section. This section was sealed and carefully evacuated into the chamber by opening valve 4-5. Successively the ball valve (2) was opened. The pressure in the gas reservoir section was adjusted by using valves 3, 5 and 6 and was monitored by a Pirani pressure sensor (Pfeiffer TPR 280) placed between valves 3 and 5. The injection was initiated by opening an electronically-controlled pneumatic valve 1 which caused flow of the gas volume into the chamber, dispersing (aerosolizing) the particles. The flow generated a particle-laden jet expanding into the chamber. Care was taken to clean the injector tube when changing sample in order to avoid contamination. The decompression pressure ratio between the reservoir and the AWTSII chamber ($p_{0\text{i}}/p_{\text{ch}}$) controlled the pipe flow and particle-laden jet dynamics (see Section 1.2.1 and 1.2.3).
The injector system could be oriented in angular direction by carefully adjusting two analogue Palmer micrometers: this allowed the jet to disperse into a specific chamber region, e.g. where the electrostatic analyzer system was placed (Fig. 2.4). The aerosolizing system could be installed either on side flanges of AWTSI and AWTSII, or on the top flange of AWTSII. When injecting from the top, the injection tube was bent by 90° allowing the particles to be emplaced in the T piece.
The injection tube and the T piece were electrically insulated from the envi-

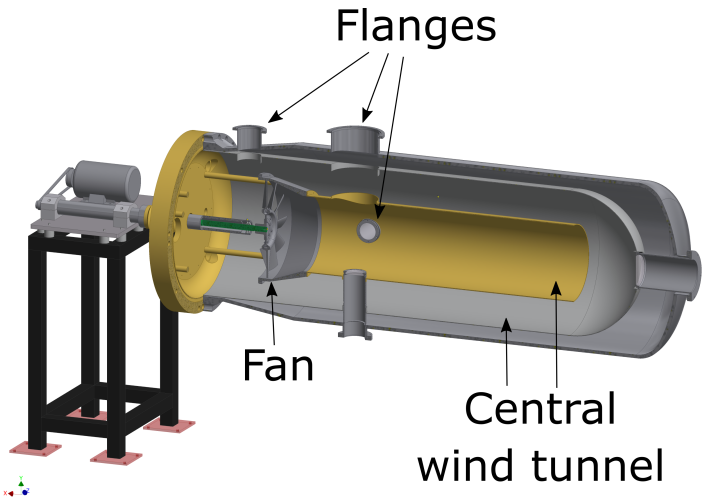

(a) 3D CAD of AWTSI

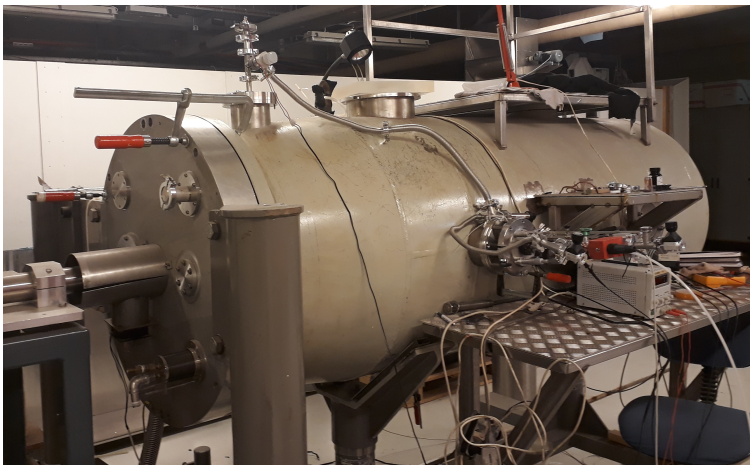

(b) Picture of AWTSI

Figure 2.2: 3D CAD of AWTSI (a) and a picture of it (b).

ronmental chamber and other parts of the injection system; this was achieved using plastic O-rings/clumps.
Various injector tube materials have been used (stainless steel 316L, copper, borosilicate glass, quartz and alumina). When using non-conductive injector tubes they were enclosed in conductive (copper) foil, thereby functioning as a Faraday cage. Valve 2 was made of stainless steel (≈ 2cm long, i.e. 4% of the total injector tube length, 50cm), and electrification measurements could have been affected by contact between particles and the inner valve surface; nevertheless, specific tests to quantify this effect were performed where the ball valve was floating and the charge generated in the T piece and long tube section was studied individually (see Fig. 5.8, Section 5.5). Results showed no change in the charge leaving the T piece and entering the long tube section, i.e. the ball valve effect on charge measurement is negligible.

In the case of injection at low over pressure some of the particles could not be dispersed and either remained inside the injector tube or were injected as aggregates, which were observed to be as large as mm size. After repeated injections evidence has been seen for a gradual accumulation of microspheres within the injector tube, specifically: particle dispersion increased after repeated injections, and aerosol generation was observed even without adding further powder material. When injecting with high overpressure (e.g. 1000mbar in the gas reservoir and 2.5mbar in the environmental chamber) many of these phenomena were no longer observed. Theoretical considerations over adhesive/lift forces within the injector tube and experimental quantification of the degree of aggregation for silica microspheres are presented respectively in Section 1.2.2 and 3.3.
Electrical breakdown was sometimes observed between the particles and injector tube. This was seen as sudden changes in measured injector tube voltage and/or from the light emitted with the use of an high speed camera (results are shown in Section 5.3).

2.3.1 Evolution of the thermodynamical parameters along the tube and particle cooling

Based on theoretical considerations made in Section 1.2.1, the thermodynamical quantities for this specific injector system have been derived. This will help understanding the dynamics of the injection process and interpreting the results. Note that it is not expected that the adiabatic and quasi-stationary flow approximations used here are highly accurate for this experimental case, so

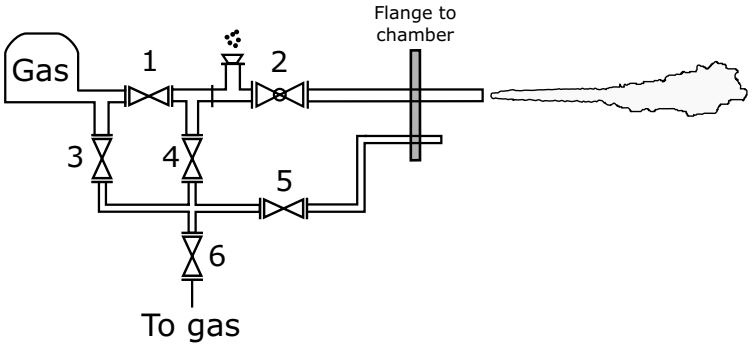

(a) Schematic setup

(b) Picture

Figure 2.3: A schematic of the aerosolizing system (a) and a picture of the aluminium oxidide T piece and injector tube (b). In this picture the tube is enclosed in conductive copper foil, except for the last 2 cm.

the following calculations will only provide an order-of-magnitude estimate and serve as guidelines in absence of direct experimental measurements.
The gas phase will be examined, the presence of particles (i.e. the inter-coupling between the gas phase and the solid particles) is neglected for simplicity. The highest decompression ratio case will be considered, in which the reservoir pressure is initially set at ambient pressure ($p_{0i} = 10^5$Pa) and discharges into the atmospheric chamber set at $p_{ch} = 250$Pa. Given such decompression pressure ratio $p_{0i}/p_{ch} = 400$, the Mach number at the tube outlet is expected to be $M = 1$. With regard to possible adiabatic cooling effects this is a 'worst case scenario' case.
An average Reynolds number of $Re_D = \rho UD/\mu \approx 3.5 \cdot 10^4$ is estimated at the tube outlet, where $M = 1$ and the fluid density and temperature are derived from the initial reservoir conditions using Eq. 1.9 and 1.10. Assuming a smooth tube, from Moody's chart a Darcy friction factor $4f \approx 0.025$ is obtained.

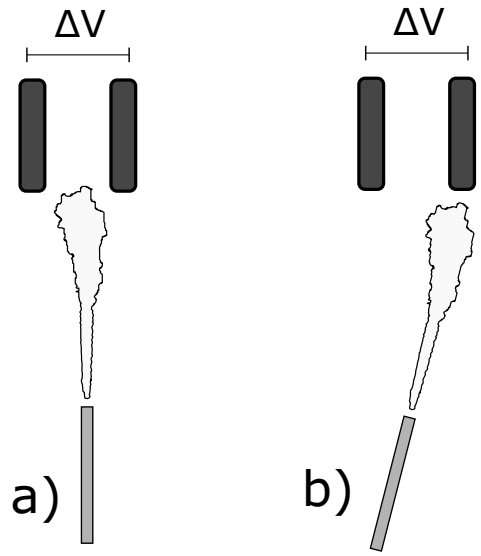

Figure 2.4: Schematic representation of the effect of tilting the injector system with respect to the electrodes region: a) straight injector, the jet core settle within the electrodes region b) tilted injector, the outer part of the jet settles in the electrodes region.

By imposing $L^* = 0.5$m (i.e. the real tube length of our experimental setup) a Mach number at the duct entrance $M_A \simeq 0.36$ is found from Eq. 1.13. The Mach number successively increases along the tube, finally reaching $M = 1$ at the tube outlet.
The Mach number and thermodynamic parameters relative to the reservoir (p/p_0, ρ/ρ_0 and T/T_0) have been calculated as explained in Section 1.2.1. The results are shown in Fig. 2.5 between the duct entrance (point 'A') and outlet (point 'B'). These calculations are valid while the flow is choked.

Fig. 2.5 shows that substantial cooling happens only towards the end of the tube: for an initial reservoir temperature $T_{0i} = 293$K, the maximum gas cooling at the end of the tube is estimated as $\Delta T_{\max} \simeq 49$K. It is important to note that experimentally the measured charge is not seen to vary significantly with the tube length after $\simeq 38\%$ of the total tube length (see Section 5.5) or with the initial reservoir pressure in the range $p_{0\mathrm{i}} = 10^4 - 10^5$Pa (see Section 5.2): this strongly indicates that temperature changes of the gas/particle during the injection process do not affect the measured charge (electrification).

It is useful to estimate the Stokes number, which expresses the ratio be-

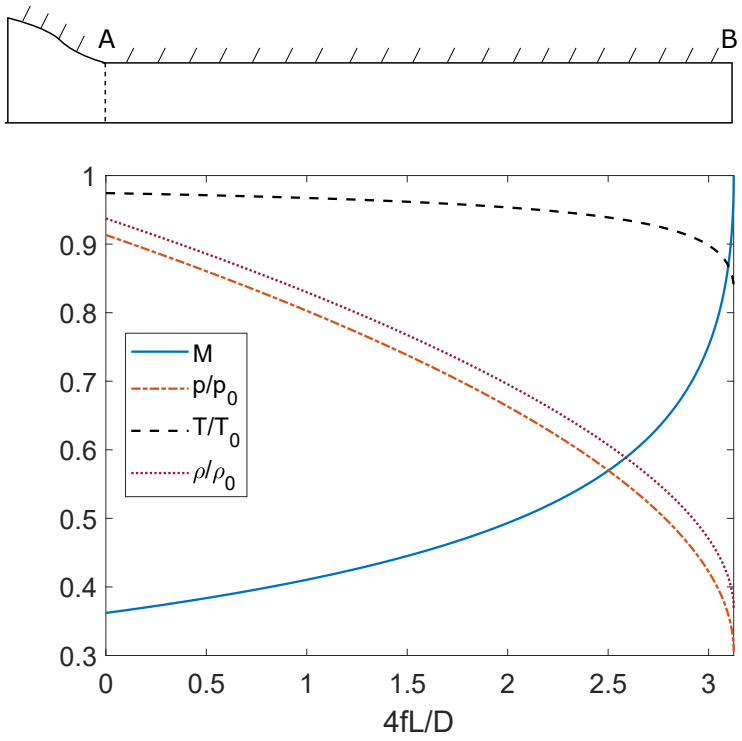

Figure 2.5: The evolution of Mach number, pressure, temperature and density ratio with respect to their reservoir values, as a function of the non-dimensional duct section $4fL/D$. The nozzle-duct system is represented schematically on top.

tween particle and flow characteristic time:

$$St = \frac{\tau_p U}{D} = \frac{\rho_p d_p^2 U}{18\mu D} \tag{2.1}$$

Where U is the fluid velocity and D is the tube diameter. For $St \ll 1$ a particle follows the flow, for $St \gg 1$ particles detach from the flow, especially under large velocity gradients.
The second expression in Eq. 2.1 is valid for low particle Reynolds number $Re_p = \rho_f (U - U_p) d_p / \mu < 1$, i.e. for low relative velocity between the particles and the gas flow (e.g. ≈ 3m/s for a 10μm particle). As the relative velocity between the gas and the particles is unknown it should be noted that, if $Re_p > 1$, Eq. 2.1 would then result in an overestimate of the Stokes number [96].
An order-of magnitude calculation for a Silica particle computed using the

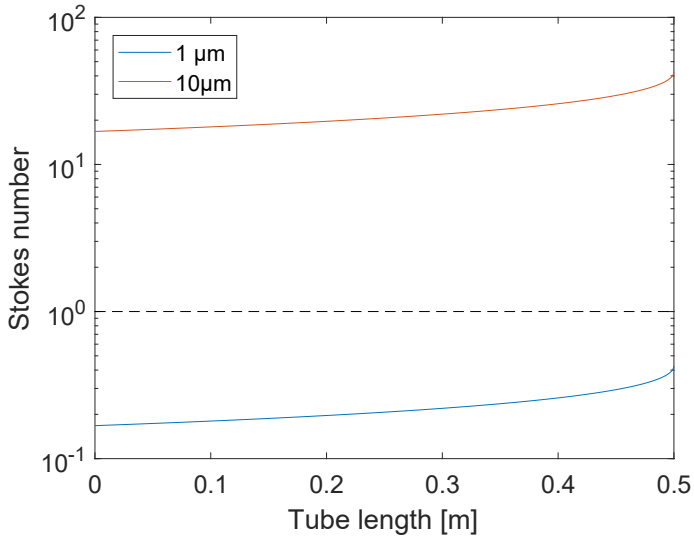

Figure 2.6: Stokes number along the tube for a 1μm and a 10μm Silica particle.

Fanno flow relations for the gas flow with the initial reservoir conditions used here, indicates that a 1μm particle should be well coupled with the flow, while a 10μm particle should already have a Stokes number larger than 1 (Fig. 2.6).

In the experimental work of Lau et al. [97, 98] measurements were performed in order to determine the particle concentration at the exit of a pipe flow, here it was shown that particles with $St < 1$ tend to accumulate in the near-wall region while particles with $St > 10$ tend to be more concentrated in the bulk region (i.e. the center of the tube). This implies that there may be expected structure observed in the particle-laden jet depending on the varying flow conditions and particle size.

2.3.2 Experimental observation of the jet

After leaving the injector tube, the gas phase coupled with particles form a particle laden jet. The characteristics of the jet were seen to be dependent on the reservoir and chamber pressure. When injecting with atmospheric pressure ($p_{0i} = 1000$mbar) and low chamber pressure ($p_{ch} = 2.5-10$mbar) a highly turbulent jet was seen, and particles were dispersed in a large portion of the AWTSII chamber. When performing low pressure injections ($p_{0i} \simeq 10$mbar, $p_{ch} \simeq 2.5$mbar) an (apparently laminar) vortex ring and trailing jet was visible

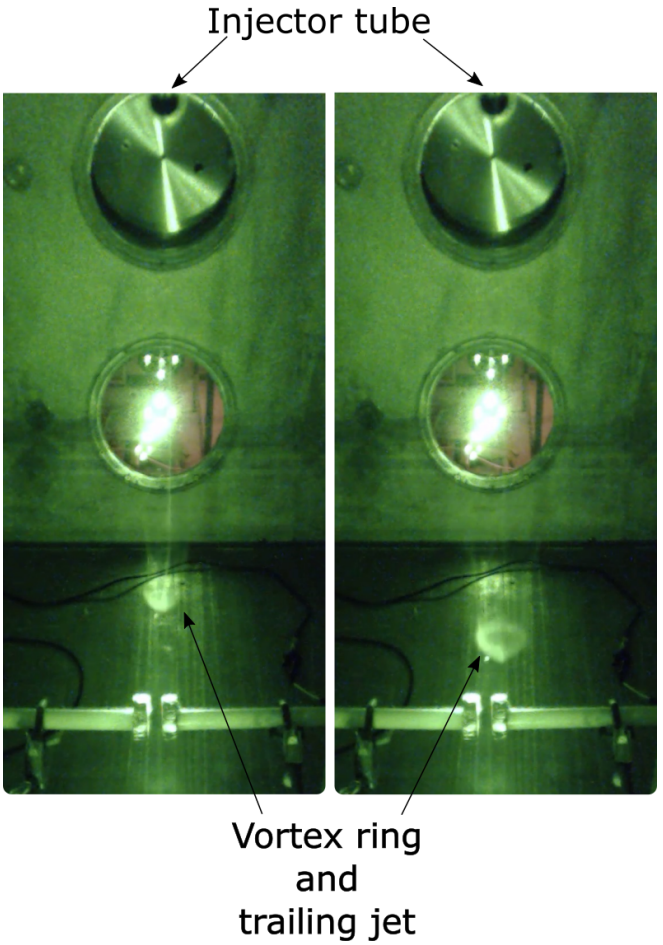

Figure 2.7: Snapshots from a camcorder video filming the injection process. The injector tube is placed in the flange at the top of the image. The jet has a low Reynolds number due to the low pressure in the chamber and the low overpressure it was generated with. A particle-laden jet settles in AWTSII.

and could be imaged with the use of a camcorder (screenshots are shown in Fig. 2.7 and 2.8). In the case of such a low-pressure injection the jet region was seen to have a lower spreading angle and stayed confined in a narrower region.

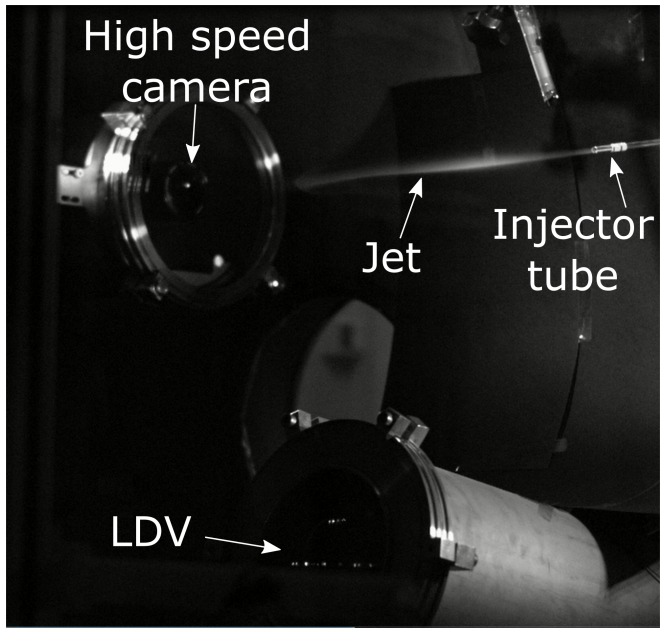

Figure 2.8: Experimental setup including the injection tube generating a laminar jet, a box with an high speed camera at the top left and a laser Doppler velocimeter at the bottom. This picture is a still shot from an high speed camera video filmed from an outer window of AWTSII

2.4 System for single-particle electrification measurements (LDV-based technique)

During the injection process contacts between particles and the injector tube lead to a net transfer of electrical charge. The experimental techniques used in this work for quantifying the contact electrification of particles will be shown in the following sections. The first measurement technique presented here has been developed specifically for this work: a 2D Laser Doppler Velocimeter (LDV) capable of measuring the vertical and horizontal velocity of single particles, allows the simultaneous determination of size and electrical charge of individual particles (see schematic setup in Fig. 2.9). The particle-laden jet (particle cloud) formed during the injection process settles through a pair of parallel electrodes across to which an electric field is applied (Fig. 2.10). Alternating polarity is used typically with a frequency of 10Hz, in order to avoid drift of the electrified particles out of the measurement volume and collision with the electrodes. The electrodes have a separation of 2.2cm and a diameter

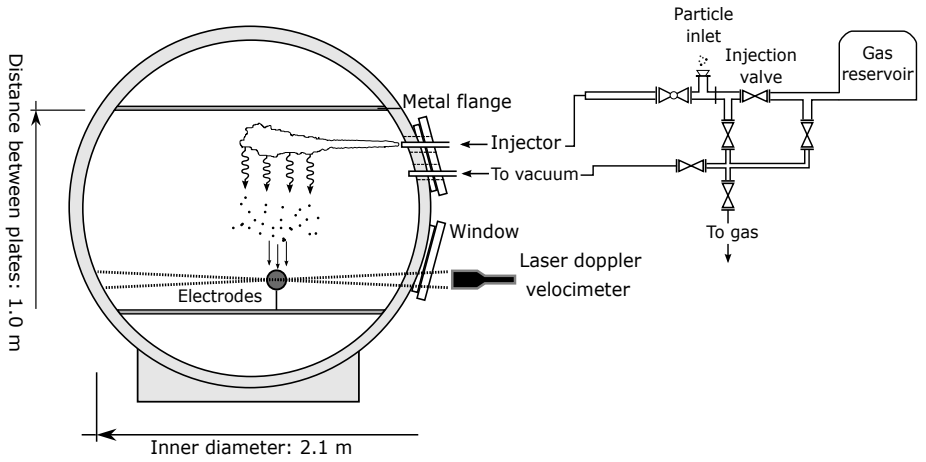

Figure 2.9: A schematic of the LDV-based technique setup.

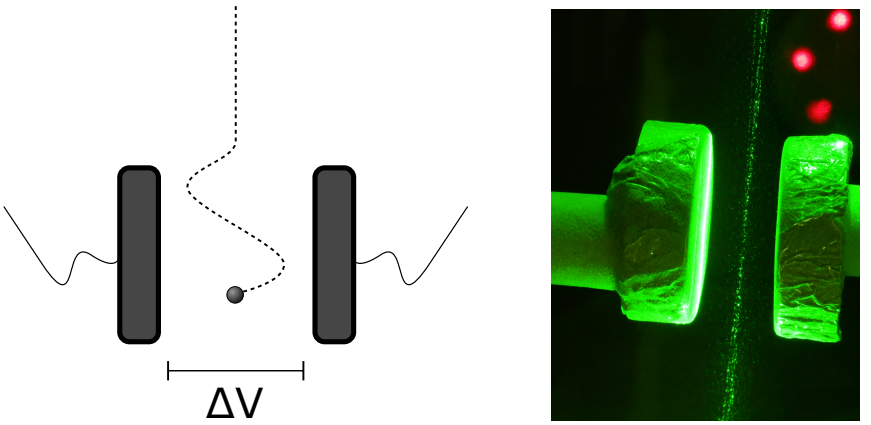

(a) Schematic setup

(b) Picture

Figure 2.10: A schematic of the electrodes (here the oscillating settling particle path has been exaggerated for better visualization) (a) and a picture of it (b).

of 5cm. Voltages between 15V - 600V were used (typically 30V) corresponding to electric fields in the range $7 \cdot 10^2$V/m – $2.7 \cdot 10^4$V/m.

The system was tested and calibrated by turning on and off the electric field on the electrodes while measuring the horizontal velocity of individual settling particles: in Fig. 2.11 a clear change is shown when 0V or 30V AC (10Hz) were applied. The AC voltage was driven by an analog electronic system synchronized with the LDV system. This allowed the polarity of the ap-

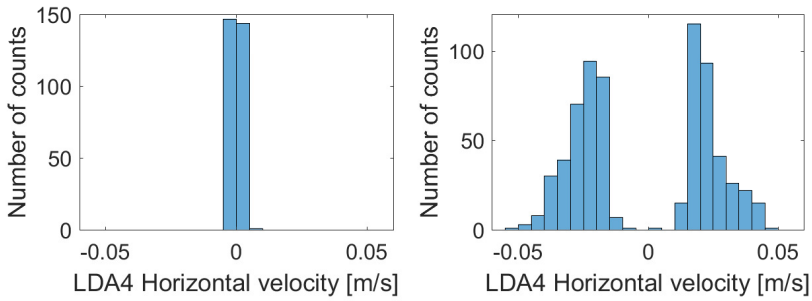

Figure 2.11: Histogram of measured horizontal velocity with the LDV. Left: 0V applied. Right: 30V AC at 10Hz applied.

plied voltage to be determined for each detected particle velocity.

Typically the aerosol injector was oriented horizontally 1m from and 0.6m above the electrodes. Experiments have been performed also injecting from the top of the chamber. A Palmer micrometer system was used to control the orientation of the jet with respect to the electrode region (2.3) such that the electrification of different regions within the jet structure could be sampled. Typically chamber pressures of 2.5 – 10 mbar and injection pressures of 8.5 – 40 mbar were used. The pressure was chosen so that the settling velocity was within a desirable measurable range (0.1–5cm/s). Injecting with low pressure also had the benefit of reducing turbulence in the measurement region (i.e. low Reynolds number).

A 2D Laser Doppler Velocimeter (Dantec LDV - 2D flowlite1) measured instantaneously the horizontal (U_x) and vertical (U_y) velocity of individual particles. The LDV had 4 laser beams (2 each for measuring the vertical and horizontal velocity component) crossing in the interception volume, which consists of a fringe pattern due to the interference of the two laser beams. The two beams are slightly shifted in frequency, so that the fringes created by the interference pattern are moving with constant velocity: this allows both the positive and negative velocity vectors to be measured. When a particle passes through the laser beam interception it back-scatters the laser light into the LDV photodetector. The shift in the light frequency due to the particle velocity (Doppler shift) causes a shift in the frequency of the detected light signal (re-shift of the observed fringe pattern) from which the particle velocity can be calculated. The system should not need any calibration and should be extremely precise. The laser beam interception point depends on the lens used: typically in this study a lens with 1500mm focal length was used, due to the setup geometry (i.e. measuring approximately in the middle point of the chamber). The disad-

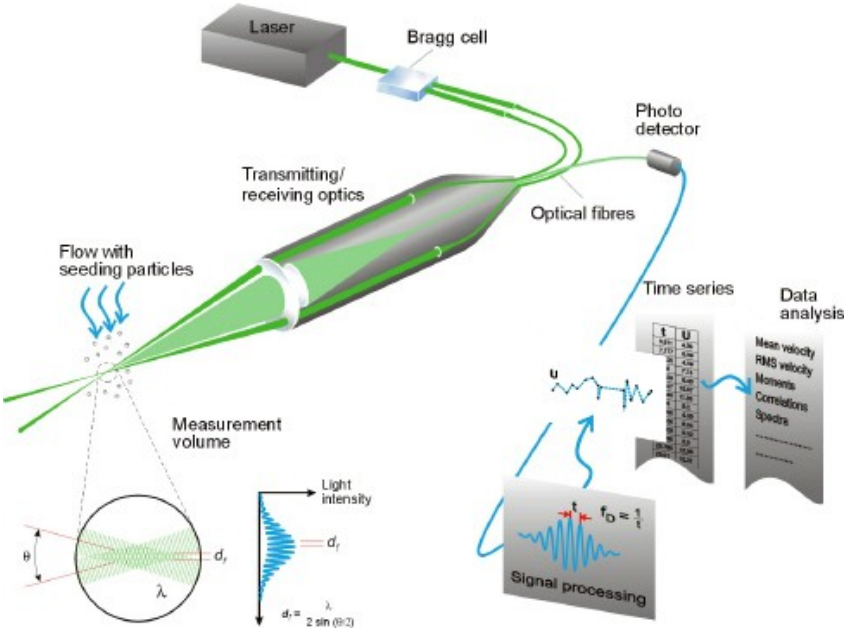

Figure 2.12: A schematic representation of the LDV system. Figure reprinted from DANTEC website[2].

[2] https://www.dantecdynamics.com/measurement-principles-of-lda

vantage of using such a long focal length is the reduced intensity of the scattered light from the particle surface. The measurement volume given by Dantec [99] is 1.3mm^3.

Assuming the particles are spherical U_y and U_x are used to derive the respective electrical charge (q) and radius (r) of individual single grains applying a simple force balance expression. The differential equations governing the motion on a sphere can be written in a Cartesian system by applying a force balance in the two directions (the vertical direction y - gravitational settling, and the horizontal direction x - electric field drift) as:

$$m\dot{\vec{U}}_y + \vec{F}_{\mathrm{D,Eps},y} + m\vec{g} = 0 \tag{2.2}$$

$$m\dot{\vec{U}}_x + \vec{F}_{\mathrm{D,Eps},x} + q\vec{E} = 0 \tag{2.3}$$

Given the particle size and gas density, drag is described by molecular scattering (see Section 1.2.4) as it is characterized by a Knudsen number always

greater than 3 ($Kn = \lambda/2r > 3$). Here $\vec{F}_{\mathrm{D,Eps}} = -k\vec{U}$ is the molecular drag force using Epstein expression [91], with $k = \frac{4}{3}\pi\delta r^2 \rho_g \bar{c}$; m is the mass of a particle; g is the gravitational acceleration; q is the electrical charge on a particle; E is the applied electric field.
By imposing the initial conditions for Eq. 2.2:

$$U_y(0) = 0 \tag{2.4}$$

and for Eq. 2.3:

$$U_x(0) = U_{\mathrm{T,x}} = \frac{qE}{k} \tag{2.5}$$

These first-order ordinary differential equations can be solved giving the solutions:

$$U_y(t) = U_{\mathrm{T,y}}\left(1 - e^{-\frac{kt}{m}}\right) \tag{2.6}$$

$$U_x(t) = U_{\mathrm{T,x}}\left(1 - 2e^{-\frac{kt}{m}}\right) \tag{2.7}$$

$U_{\mathrm{T,y}} = \frac{mg}{k}$ and $U_{\mathrm{T,x}} = \frac{qE}{k}$ are the terminal velocity respectively in the vertical and horizontal direction.
The particle time constant τ is defined as:

$$\tau = \frac{m}{k} = \frac{\rho_p r}{\rho_g \bar{c}\delta} \tag{2.8}$$

Particles counted within a time $< 2 \cdot \tau$ (typically $\tau < 10^{-2}$s) before and after the polarity-switch time were deleted from the results. Given a typical settling velocity $U_{\mathrm{t,y}} = 2$cm/s for a 4μm particle, the electrodes diameter of 5cm and the frequency of the oscillating electric field 10Hz, a particle is expected to be drifted more than 10 times during its settling through the electrodes. The analytical solution for the velocity $U_x(t)$ and position $x(t)$ profiles over time is shown in Fig. 2.13.

Particle radius and charge are calculated using the equations:

$$r = \frac{U_y \delta \rho_g}{g\rho_p}\sqrt{\frac{8k_{\mathrm{B}}T}{\pi m_{mol}}} \tag{2.9}$$

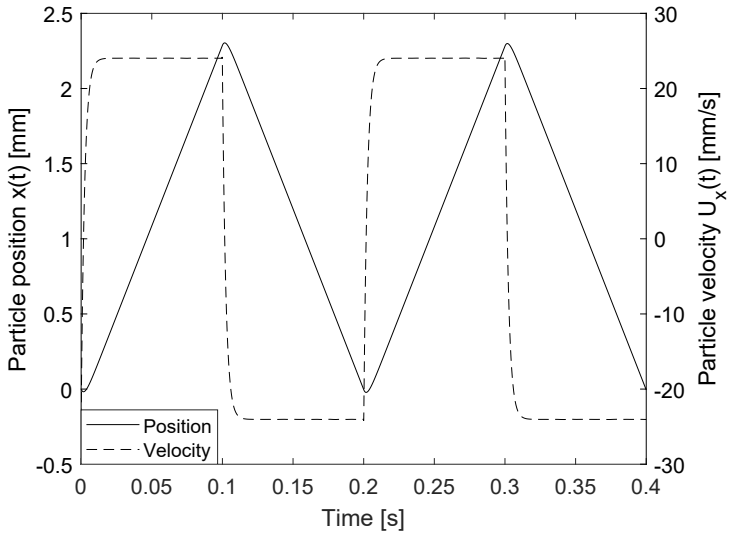

Figure 2.13: Horizontal velocity and position profile of a typical particle used during the experiments (silica microsphere, $d = 4\mu$m, 30V applied at the electrodes changing polarity with a frequency of 10 Hz and $q = 3100e$).

$$q = \frac{4\pi\delta\rho_g r^2 U_x}{3E}\sqrt{\frac{8k_B T}{\pi m_{mol}}} \tag{2.10}$$

Where μ is the molecular viscosity of the gas, ρ_g is its density, m_{mol} is its molecular mass, k_B is the Boltzmann constant, T is the temperature ($\approx 300K$), E is the electric field and ρ_p is the particle mass density. The free parameter in Epstein's drag model has been taken from a previous study of settling speeds [93] as $\delta = 1.15$.
As discussed in Chapter 1, it is useful to calculate the surface charge concentration on a single particle (assuming it is spherical and the charge is spread over the entire surface) using the relation:

$$\sigma = \frac{q}{4\pi r^2} \tag{2.11}$$

Limitations with the use of the LDV technique

There are several physical factors which potentially significantly could affect the accuracy of the LDV measurements and for which care was taken during measurement taking and analysis. These will be discussed here:

- *Measuring sub-μm particles:* It is problematic to use this technique with particles smaller than 1 μm, as the LDV becomes insensitive at such small scales. This is due to the insufficient amount of light reflected into the detector. The detector efficiency is heavily dependent on particle size: it was experimentally observed that individual grains significantly less than 1 μm in diameter could not be measured reliably, as the number of single grains counted drops towards zero despite the higher number of injected particles. It should be noted that some particles (e.g. Fe, Zn, W) would be expected to absorb light due to their dark colour, causing reduced light scattering efficiency.

- *Non-spherical particles:* In the determination of size and charge, the particles are assumed to be spherical. However in some cases non-spherical particles were used. This will be a source of uncertainty due to the different drag coefficient with respect to a spherical particle.

- *Jet-induced turbulence:* Turbulence induced by the injection process may introduce random fluctuations in velocity measurements if the perturbation reaches the electrodes region. An example of such jet-induced turbulence on LDV measurements is shown in Fig. 2.14. Turbulence can be considerably reduced by lowering the decompression pressure ratio between the gas reservoir and the chamber. It has been observed experimentally that a pressure ratio of ≈ 10 generally produces undisturbed results.

- *Chamber gas turbulence (Brownian motion):* Turbulent velocity fluctuations of the gas inside the chamber are always present, independently from the aerosolizer induced flow. These are typically significant only for high chamber pressure and/or small particles where the measured velocities are low ($\ll$ 1cm/s). Assuming the distribution of these fluctuations is a Gaussian function, the mean value of the measurements would not be affected, but will rather increase the variance of the velocity distributions. An example of this effect is shown in Fig. 2.15.

- *Aggregation:* Particle aggregation (cohesion) would be observed as a distribution of particles measured with increased size (asymmetry in the size distribution, see Fig. 2.16). Such observation are commonly made especially with the smallest particles ($\leq 1\mu$m). This will be studied in detail in Section 3.3.

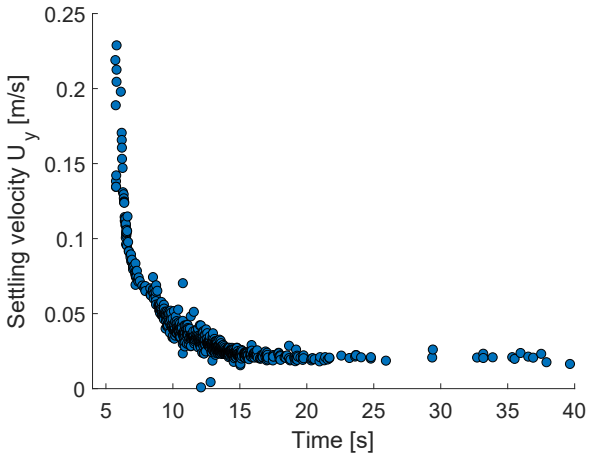

Figure 2.14: An example of jet-induced turbulence for the measured vertical velocity profile U_y of 2μm Silica microspheres spheres as a function of time. The first measured particles are driven by the jet turbulence, and the measured velocity is higher than what would be expected for such particles (i.e. the velocity reached after 15 s, around 2cm/s).

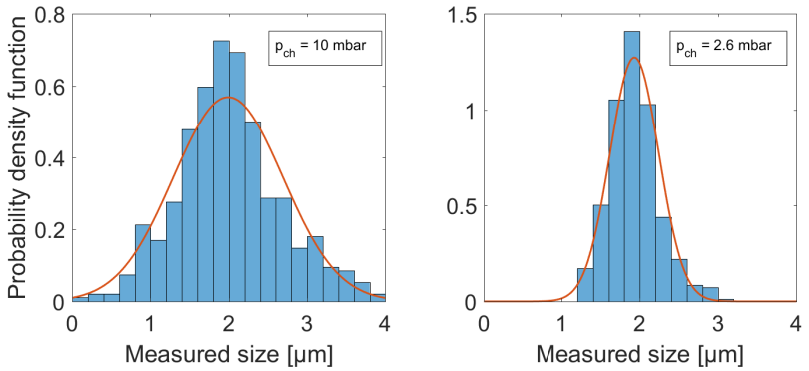

Figure 2.15: Histogram and underlying probability distribution for respectively 2 µm Silica microspheres settling in air at 10 mbar (left) and 2.6 mbar (right). Lower gas pressure in the chamber reduces the chamber gas turbulence.

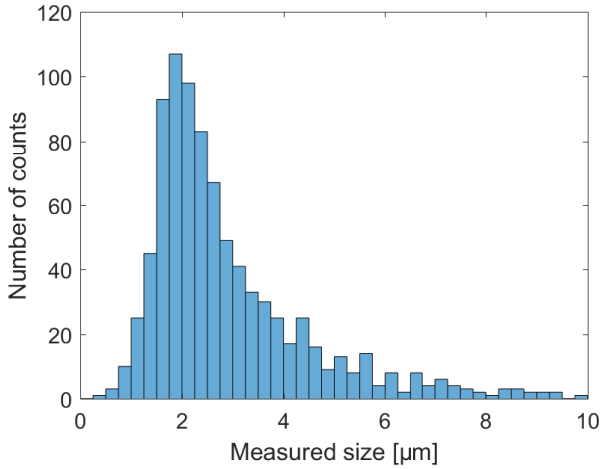

Figure 2.16: Aggregation seen as a tail in the distribution of 2 μm Silica microspheres.

Other factors potentially affecting the results:

There were several factors which could have contributed to inaccuracy of this LDV-based technique, but were found not to be significant. These will be discussed here:

- *Particle characteristic time:* A particle can potentially reach the electrodes region before reaching its terminal settling velocity (i.e. before drag force equilibrates gravity force). In this study the 'worst case' would be a 10 μm silica microsphere settling in air with gas pressure of 2.5 mbar. Its characteristic time calculated using Eq. 2.8 would be $\tau \approx 7ms$. After $\approx 3\tau$ such a particle has reached 95% of its terminal velocity (around 7cm/s) and has traveled for around $2mm$. Such distance is much shorter than the vertical distance between the injector and the LDV/electrodes measurement region ($\approx$ 60cm). Each measured particle should therefore have reached its terminal velocity in the LDV (electrodes) measurement region if jet-induced turbulence is negligible.

- *Error on measured velocity due to rotation:* as the LDV measures the surface velocity of a particle, particles rotating could induce a broadening in the measured velocity distribution. However, accurate measurements of mono-sized Silica microspheres suggest that this factor does not play an important role (Fig. 2.17).

- *Contamination with other powder sample:* Adhesion of particles within the injector tube was observed (see Section 3.4). Cleaning the injector tube when changing sample was seen as an effective solution in order to avoid contamination.

- *Drag coefficient modification due to particle shielding:* a high concentration of particles may in principle alter the drag coefficient due to mutual interactions. In the continuum regime, where Stokes law is applicable, this would be due to the overlapping of the boundary layer of individual particles. In the molecular regime this effect is due to the change in gas molecules scattering on the particle surface as a result of nearby particles shielding. For a typical injected mass of 20mg of 1 µm particles, the number of injected particles is less than $N_p < 10^{10}$, dispersed over a volume of approximately 0.2m^3. This results in a number concentration of $n < 5 \cdot 10^{11}$ particles per cubic meter. An average particle separation may be estimated as $(1/n)^{1/3} \simeq 125\mu$m, which is more than 100 times larger than the particle diameter. It may be concluded from this order-of-magnitude calculation that the drag coefficient is unlikely to be affected by shielding. No direct observation for this effect was observed experimentally, as confirmed by correct size measurements (Fig. 2.17)

- *Particle fracturing:* This would appear as a distribution of grains with reduced size (or asymmetry). No such observation were made when measuring the size distribution of mono-sized Silica microspheres.

2.5 Average charge measurement over the whole particle cloud (Faraday tube technique)

The use of Faraday cage, cups etc. have been often applied in studies about contact electrification [42, 61, 72, 100], and it represents a reliable tool for directly measuring particles electrical charge. Applying it to an aerosolizing jet allows to quantify directly the total net charge acquired by the whole particle cloud during the injection process and also its time dependence. Nevertheless, information about single-particle charge may be lost.
In this study the injector tube is electrically isolated. In the case of non conductive injector tubes they are enclosed in conductive copper foil which functions as a Faraday cage. Here electrical charges entering or exiting the tube generate a time-dependent voltage between the injector and the (grounded)

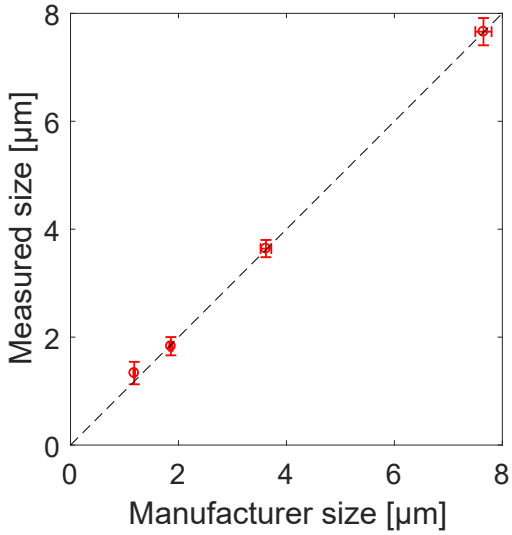

Figure 2.17: Particle size provided by the manufacturer plotted against the measured size (using the LDV), for mono-sized spherical SiO_2 particles. Horizontal and vertical error bars represent the standard deviation of the distribution, respectively from the manufacturer data sheet and from the measured distribution. Mean and standard deviation for both the manufacturer and measured size are also reported in Table 3.1.

vacuum chamber. This was measured using an oscilloscope (Tektronix DPO 2002B). By integrating this voltage $V(t)$ over time (typically $< 150ms$) the total net charge Q leaving the injector system is obtained:

$$Q = \int -I(t)dt = \int -\frac{V(t)}{R}dt \tag{2.12}$$

Where $I(t)$ is the injector discharge current, R is the impedance between the injector and chamber ($R = 10\text{M}\Omega$) and the minus sign is to take into account of the opposite charge of the particles with respect to the injector tube.
A second oscilloscope probe was used to monitor possible electrical charges exiting from the gas injection side, this was possible if particles accidentally contaminated the gas reservoir (e.g. in Fig. 2.19).
The particle electrification as a function of transit through the injector tube could also be studied. This was done either by electrically isolating the T piece from the long tube section (i.e. two individual Faraday systems) and study the Q transferred to each section, or by modifying the length of the copper foil

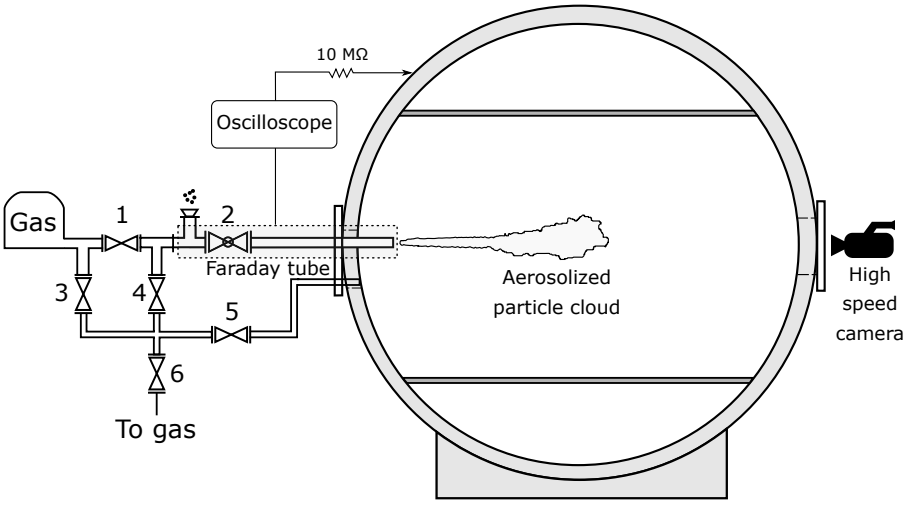

Figure 2.18: A schematic of the Faraday tube technique setup.

enclosure around insulating injector tubes. Results are presented in Section 5.5.

The capacitance of the injector system could be quantified by applying a voltage on the injector tube (e.g. with a 9V battery) and measuring the time constant of the exponential decay to 0 on removal of this voltage (Fig. 2.20). An exponential best-fit method of the form $V(t) = V_0 e^{-t/RC}$ is used to derive the capacitance (C) of the system, with $RC \simeq 4.3 \cdot 10^{-4}$s and $C \approx 43$pF.

The total injected mass M of each measurement was obtained by weighing using a scale (Sartorius CP224S) with an accuracy of 0.1mg, typically as the mean value of a set of 3 injections. By knowing the mean particle radius r and the particle mass density ρ_p, it is possible (assuming the particles are spherical) to derive a mean value for the surface charge concentration σ on a single particle using the relation:

$$\sigma = \frac{q}{4\pi r^2} = \frac{Q\rho_p r}{3M} \tag{2.13}$$

Where q is the charge on a single particle, and Q is the total charge of the entire injection calculated using Eq. 2.12.

Random and systematic uncertainties when calculating surface charge concentration using the Faraday tube technique are:

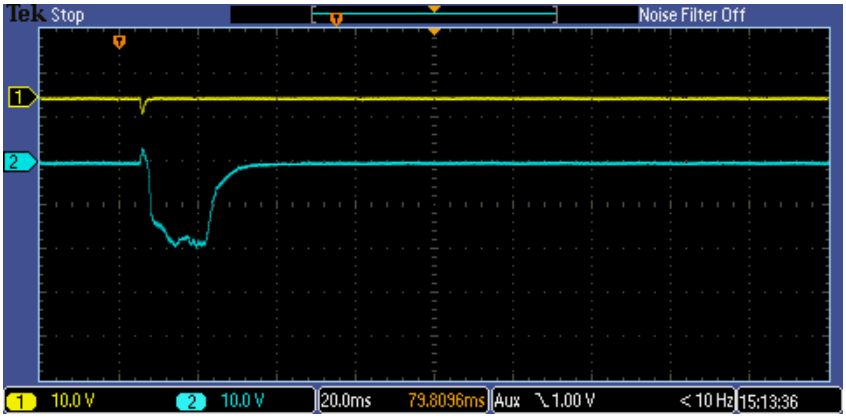

Figure 2.19: A screenshot from the oscilloscope Tektronix DPO 2002B. Channel 2 (blue line) shows the measured voltage on the Faraday tube. Channel 1 (yellow line) monitors the gas reservoir voltage for possible contamination of charged particles entering the Faraday tube. If present (as in this case), they also appear as a mirrored signal on Channel 2.

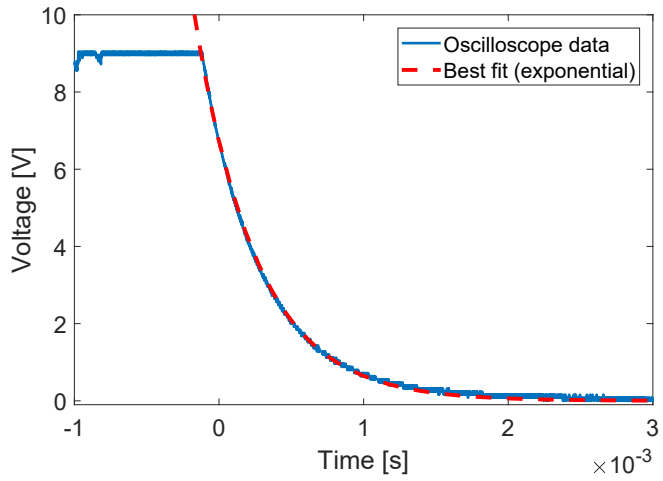

Figure 2.20: Calibration of the injector tube's capacitance. The voltage measured on the injector system after breaking the contact with a 9V battery is shown (blue line), together with an exponential best fit (dashed line): $V(t) = V_0 e^{-t/\tau}$, where $V_0 = 8.785V$ and $\tau = 4.3 \cdot 10^{-4} s$.

- *Electrical discharges:* electrical discharges through gas breakdown between particles and the injector tube and/or between sections of the injector tube and the chamber have been observed and can lead to alteration of the measured Q. This was systematically investigated in Section 5.3.

- *Background noise in the oscilloscope signal:* background noise in the measured voltage was seen to be significant for low signals (i.e. $< 1V$) sometimes causing a '0 offset' in the measured signal (e.g. see Fig. 5.8). The magnitude of this noise is dependent on the selected voltage range on the digital oscilloscope. Its effect was removed from the results by calculating the mean voltage in a time range before the triggering signal (i.e. $t = 0$, corresponding to the electrical trigger initiating the opening of the pneumatic valve 1 in Fig 2.3).

- *Uncertainty on the injected mass:* when placing the powder into the funnel down to the T piece a fraction of the particles can stick to the funnel/scoop walls. This effect was quantified as $\approx 4\%$ of the total mass M by measuring with a precision scale the mass of powder transferred between two containers, using the same scoop and funnel.

2.6 Aggregates size/charge determination using high-speed imaging

A high-speed camera (Edgertronics) was used to film the injection process at the nozzle outlet. The light source was typically a laser sheet, and an LED lamp was added when additional light was needed. The camera could be placed both outside the AWTSI (see Figure 2.18) filming the cross-section perpendicular to the jet axis at the nozzle outlet (Fig. 2.21 - a) or in a dedicated box inside AWTSII at atmospheric pressure, filming the cross section parallel to the jet axis (Fig. 2.21 - b).

The camera and the oscilloscope were synced with an electrical triggering signal from the pneumatic injection valve (Valve 1, Fig. 2.3). The high-speed camera was used to:

1. Determine the number/size of observable aggregates ($> 100\mu$m) and their mass fraction with respect to the total injected mass

2. Correlate the observed (time dependent) particle flux with the measured electrical current leaving the nozzle

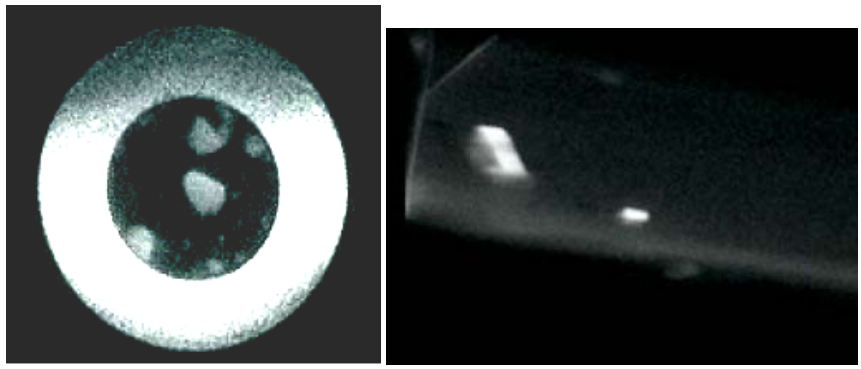

(a) Front view (b) Side view

Figure 2.21: Snapshots from high speed camera videos. (a) Front view and (b) Side view.

3. Quantify the charge of observable aggregates

These results are presented in Section 3.3.
In order to detect the size of observable aggregates, a video post-processing was performed using the software 'Fiji – ImageJ' [101, 102] using the 'Analyze particles' tool after careful adjustment of the image threshold.
Limitations for this technique are the camera resolution/frame rate, the available lens type, the power/position of the light source and the setup geometry (i.e. the distance between the camera and the nozzle outlet).

2.7 Materials

In this work micron-sized powder samples in the range 1-45 µm were used. The samples can be subdivided in 3 categories:

1. Insulating particles (Oxides)
2. Conductive particles (Metals)
3. Volcanic ash particles

All the materials used here are non-ionic and non-organic, i.e. do not contain mobile ions at the surface (see Section 1.1.2 for the definition of an ionic material and their role in contact charging).
Most of the samples were commercially available and purchased from companies. Volcanic ash samples have been collected in the field and analyzed in

another work by Vogel et al. [103] where the mean particle size, shape (aspect ratio) and bulk/surface chemical composition were investigated. The mean size of these volcanic ash samples used here is different from the one reported in [103], as in such study the authors reported a particle number-weighted size distribution, whereas for this study a volume-weighted size distribution was more sensible to use. The mean size used here derives from Laser Diffraction measurements performed by Andreas Vogel.
Although some of the samples are spherical (Silica microspheres in Fig. 2.22 and Soda Lime Glass spheres are known to be spherical) others are non spherical, adding uncertainty in the mean size assigned to each sample. A list of the materials used in this thesis is presented in 2.1 together with their mean particle size, the supplier and the sizing technique.
Metals size distribution was poorly constrained by the manufacturer data sheet and therefore their sizes were measured via settling velocity.
Injector tubes were also available in different compositions:

- Insulators: Quartz (SiO_2) and Alumina (Al_2O_3)
- Conductors: Stainless steel 316L and Copper

In most of the experiments the contact electrification between insulating or conductive materials (particle/injector) were studied. Some combination of oxide powders in stainless steel or metal powders in borosilicate glass were also tested.
In the case of copper tube and copper powder it is expected that this (reactive) metal generates an oxidized surface after exposure to air (as would also be expected for Fe particles). In fact interestingly initial measurements of copper particles with an untreated copper injector tube (clearly oxidized) gave charge values of around $Q = +3.9 \pm 1.3 \cdot 10^{-8} C$ (surface charge concentration $\sigma = +14 \pm 5 e/\mu m^2$). However in the results presented in Section 4.2 a freshly deposited copper inner tube surface by chemical deposition, a ball valve (valve 2 in 2.3) internally coated with copper and using freshly purchased Cu particles gave a significantly different $Q = -1.5 \pm 0.2 \cdot 10^{-8} C$ (surface charge concentration $\sigma = -6 \pm 0.6 e/\mu m^2$), i.e. changing polarity. In the results presented in Section 4.2, only the non-oxidized copper measurements will be shown.

2.8 Sizing techniques

Whilst the LDV technique provides a direct measurement of particle size through settling velocity (see Section2.4), an accurate determination of the mean par-

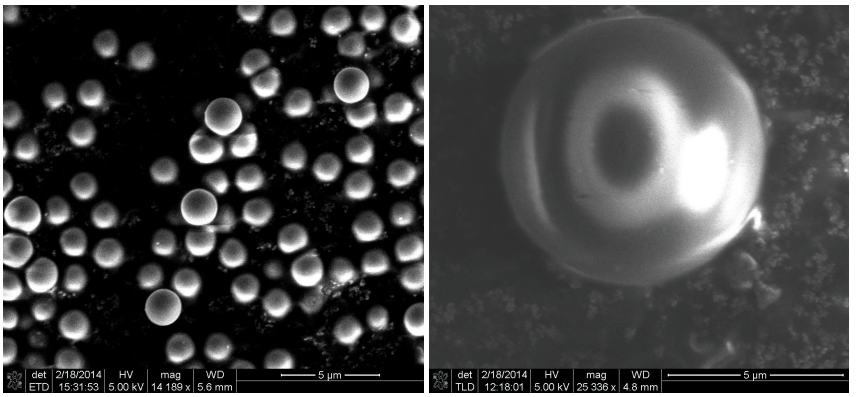

(a) $d = 2\mu$m (b) $d = 8\mu$m

Figure 2.22: SEM images of Silica microspheres from Cospheric®. Images are reprinted with permission from [93].

ticle size is crucial in determining surface charge concentration values when using the Faraday tube technique (Section 2.5). As a particle sizer is not available in our facility, the only possibility for sizing was through settling speed measurements using the LDV. Some of the size measurements rely on data sheet, published measurements in other works or sizing from collaborators. The sizing techniques used in this study are:

1. LDV measurement of terminal settling velocity (Section 2.4)
2. Laser Diffraction instrument. The size distribution of the Al_2O_3 sample have been measured in [104, 105] using a Coulter Multisizer.
3. Multiwavelength separation analyzer (LUMISizer®). This instrument measures the extinction profile of the transmitted light of sedimenting particles in a water-diluted suspension. The particle size distribution is obtained using Stokes' law from the extinction profiles [106].

In Table 2.1 a list of samples used is presented together with the respective sizing technique.

Table 2.1: Sample list

Category	Sample	Mean size [μm]	Sizing technique	Supplier
Insulators	SiO_2	0.166, 0.250, 0.500 1.18, 1.86, 3.62, 7.75	Manufacturer	Cospheric
	Al_2O_3	4.6, 9.4, 17, 27	Coulter Multisizer	[104, 105]
	Soda Lime Glass	4.5, 11.8, 47	Settling in air (LDV)	Cospheric
	TiO_2	6.1	Multiwavelength separation analyzer	AppliChem GmbH
Metals	Pt	1.8	Settling in air (LDV)	Goodfellows
	Fe	4.1	Settling in air (LDV)	Goodfellows
	W	7.9	Settling in air (LDV)	Goodfellows
	Cu	3.4	Settling in air (LDV)	Goodfellows
	Zn	7.5	Settling in air (LDV)	Goodfellows
Volcanic ash	Sakurajima	25	Multiwavelength separation analyzer	[103]
	Eyjafjallajökull	29.7	Multiwavelength separation analyzer	[103]
	Grims	42.3	Laser Diffraction	[103]
	Kelud	34.3	Laser Diffraction	[103]
	Mount St. Helens	17.2	Laser Diffraction	[103]
	Spurr	23.1	Laser Diffraction	[103]
	Chaiten	19.2	Laser Diffraction	[103]

CHAPTER 3

RESULTS: SIZE DEPENDENCE OF CONTACT ELECTRIFICATION IN OXIDES

In this chapter the contact electrification dependence upon particle size for fine solid aerosol particles ($< 50\mu$m) is investigated. For 'particle size' it will always be intended the diameter of the equivalent sphere. In the following sections the measured charge dependence on single-particle size is investigated through a combination of novel experimental techniques. This will include:

- Section 3.1 - *single-particle charge measurement (LDV technique):* the size dependence is studied by measuring simultaneously single-particle size and charge.
- Section 3.2 - *Size dependence over the whole particle cloud using the Faraday tube technique:* here an average size dependence is investigated upon all particles injected.
- Section 3.3 - *Aggregates charge and size:* the charge of cohesive powders forming agglomerates is studied using a high speed camera, the voltage measured on the injector tube and the LDV.
- Section 3.4 - *Adhesion to the injector tube wall:* in this section observations over particle adhesion to the injector tube wall and its effect over charge measurements are presented.

3.1 Single-particle charge measurement (LDV technique)

The LDV technique (Section 2.4) allows the simultaneous determination of size (r) and charge (q) of individual grains. The jet structure, aerosol concentration (dispersion) and average electrification are all sensitive to injection geometry and pressure. When using the LDV measurement technique relatively low injection pressures ($< 100 mbar$) and low chamber pressures ($\leq 10 mbar$) were required in order to: 1) obtain sufficiently high terminal velocities, 2) reduce turbulence 3), allow the particle cloud to reach the electrodes region. Low reservoir gas pressures were sometimes not able to disperse properly the whole mass of powder placed in the T piece and break up the aggregates: this phenomena was observed to be size dependent and was especially pronounced for small (sub-µm) particles.
The system was tested in nominal working conditions by measuring spherical mono-sized silica microspheres, for which the size is known. Results in Fig. 2.17 show how the mean size is measured correctly, despite a broader spread of the size distribution with respect to the manufacturer data sheet, presumably due to turbulence as shown in Section 2.4.

As discussed in Chapter 1, the most useful parameter in electrification studies is the surface charge concentration calculated using the simple relation:

$$\sigma = \frac{q}{4\pi r^2} \tag{3.1}$$

The surface charge concentration σ was seen to be dependent on the particle position in the jet's spacial structure: it consists of an inner, highly concentrated central jet and a more diffuse and divergent outer part. By controlling the injector direction with respect to the LDV/electrode system these different components could be studied separately. This can be seen in Fig. 3.1 where the two distributions have been obtained by changing orientation of the injector tube while keeping constant other parameters (particle size/composition, injection pressure, gas pressure/composition, relative humidity): it was observed that the outer particles are relatively highly electrified whereas those in the central jet have a lower charge/particle. This behaviour is presumably due to interaction (contacts) that particles experience against the aerosolizing injector tube.

The aerosol generation process has a complex dynamics: it is constituted by the rapid decompression of the gas within the reservoir into the injector tube (i.e. a pipe flow) followed by the formation of a particle-laden jet; even-

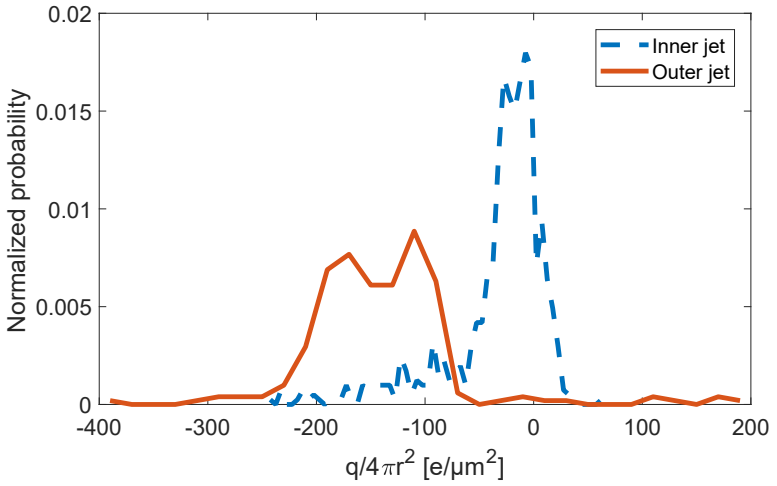

Figure 3.1: Surface charge concentration (charge per surface area) determined for aerosolized particles (2μm silica microspheres). In this figure particles within the inner portion of the jet (blue dashed line) and particles within the outer portion of the jet (red line) are shown. These different portions could be measured separately by careful adjustment of the injector tube orientation with respect to the electrodes region (i.e. also the measurement volume).

tually the particles settle in the vacuum chamber reaching the electrodes region. Different factors affecting the results are discussed in the following subsections.

Charge sorting in the injector tube

It was observed that particles interacting with the injector tube surface became highly electrified, whereas particle-particle contact led to lower electrification.
Evidences for this phenomena can be seen by measuring single-particle charge. Specifically, when the injector tube was aligned with the electrodes region/LDV laser beams (i.e. the inner jet settles in the measurement region), interesting features in the horizontal velocity (U_x) time-series could be observed. Being mono-sized, silica microspheres have very similar terminal settling velocity, so the jet region is expected to settle down encountering the LDV measurement volume progressively scanning the entire particle cloud generated after aerosolization. In particular, settling may be interpreted as particles encountering the LDV beams with a) lower part of the outer jet, b) jet core, c) upper

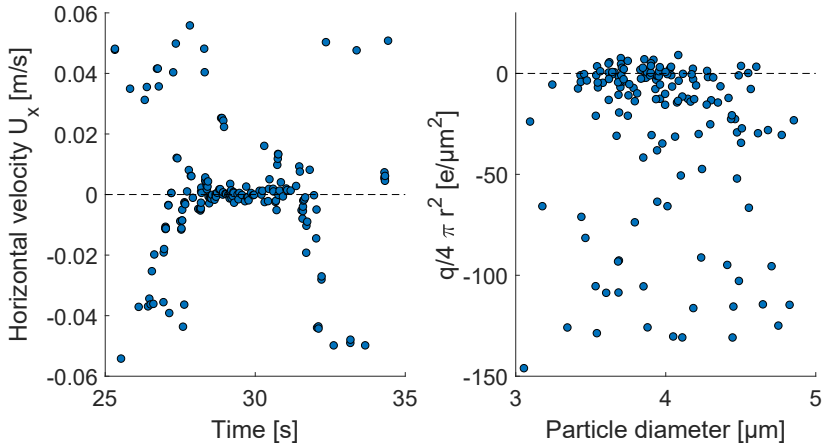

Figure 3.2: Monodisperse 4μm silica microspheres. Left panel: time series of the horizontal particle velocity (U_x). Right panel: surface charge concentration as a function of particle size.

part of the outer jet. This features could be often observed, e.g. in the left panel in Fig. 3.2.
The surface charge concentration as a function of particle size is calculated using Eq. 3.1 (right panel in Fig. 3.2) with initially highly electrified particles, followed by a large population of almost-neutral ones, followed again by electrified grains.
When the injector tube is tilted (see Fig. 2.4), particles in the inner-jet region settle outside of the electrodes/LDV region and mostly electrified particles are measured (Fig. 3.3).

A clear distinction between different jet regions can also be observed sometimes when using particles with a relatively broad size distribution ($1-8\mu$m Soda Lime Glass spheres, injected from the top of AWTSII) measuring portions of both the inner and outer jet cloud (Fig. 3.4). This distinction is sometimes less obvious depending on the dynamics of the injection and on particles interaction with the injector tube.

Evidences described above may be due to:

- Different chemical composition: when the two contacting surfaces have a different composition, a net charge is exchanged. This is often the case when particles and injector tube are chemically different, while is not

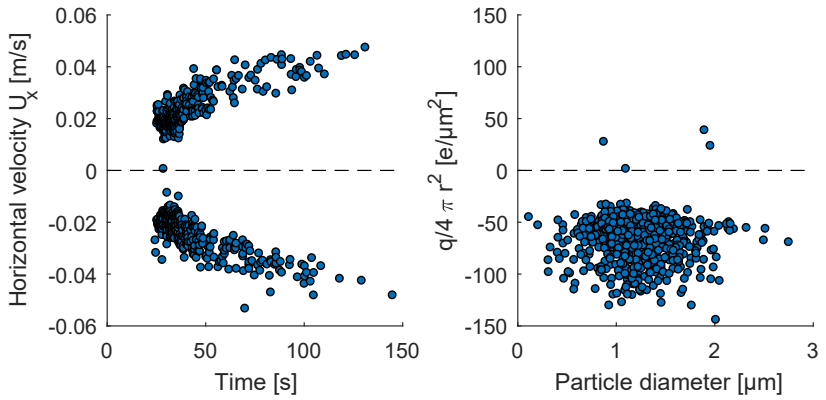

Figure 3.3: Monodisperse 1μm silica microspheres. Left panel: time series of the horizontal particle velocity (U_x). Right panel: surface charge concentration as a function of particle size.

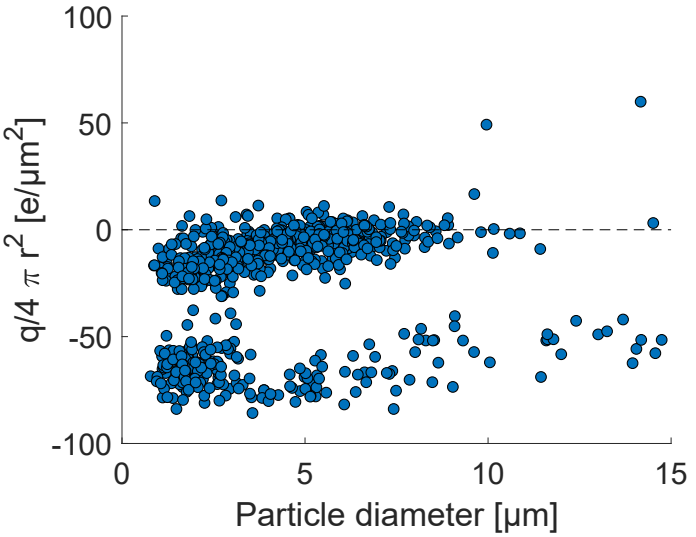

Figure 3.4: Surface charge concentration of individual Soda Lime glass microspheres (1–8μm) plotted against particle size, for a single injection. In this experiment, both the inner (with a relatively low σ) and outer (high σ) portions of the jet were measured. In this case, the aerosolizing system was placed above the electrode system at the top of AWTSII and carefully aligned with the LDV measurement region.

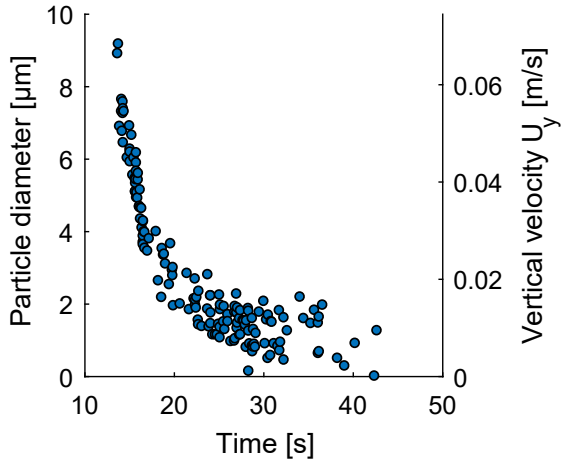

Figure 3.5: $1-8\mu$m Soda Lime Glass spheres (100V AC, 10Hz). Time series of: measured particle size ($2r \propto U_y$) (left axis) and vertical settling velocity (right axis).

the case for particle-particle contact, as they are all chemically identical. The effect of chemical composition is specifically investigated in Section 4.1.

- Change in the contact area: even for two chemically identical particles contacting, a certain amount of charge exchange is expected, and might depend on the effective contact area. The contact area is expected to be larger for particle/wall contact rather than for particle/particle contact. This aspect will be discussed in Chapter 6, Section 6.1.

Gravitational and drag-induced size separation

For samples with a non-uniform particle size distribution, bigger particles have a higher terminal settling velocity, reaching the electrodes region before smaller particles (left panel in Fig. 3.5). In case of settling within the molecular (Epstein) regime (Section 1.2.4) the particle size is directly proportional to the terminal velocity (Eq. 1.33) and therefore inversely proportional with settling time $r \propto U_y \propto 1/t$.

Size sorting happens also along the jet axis direction due to the different drag coefficient between small and big particles. This effect is present when the injector is horizontally placed: small particles are likely to settle down

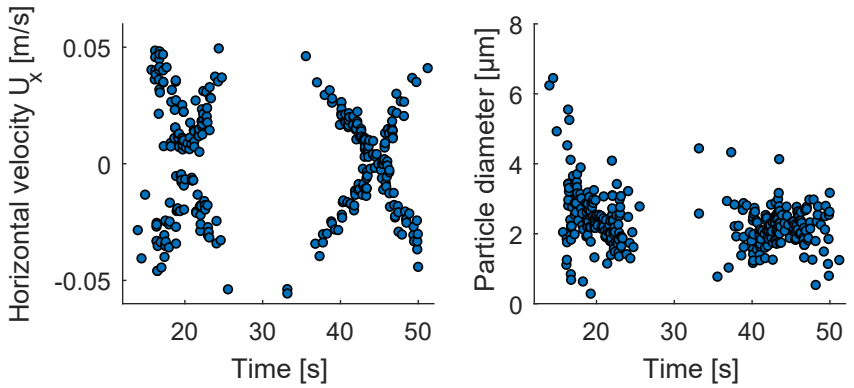

Figure 3.6: 4+2μm silica microspheres (120V AC, 10Hz). Left panel: time series of the horizontal particle velocity (U_x). Right panel: time-series of particle radius.

closer to the injection side than big particles.
Turbulent mixing in the jet region represents an additional complication to this process: particles were observed in some cases to settle down in "bursts", well separated in time. An interesting example is presented in Fig. 3.6 where a bimodal distribution of $4+2\mu$m silica microspheres was injected. Settling particles were measured in two distinct time intervals: in the first settling cloud a mixture of 2μm and some 4μm were measured; in the second group mostly 2μm particles were measured.

3.1.1 Focus on highly electrified particles

As showed above, the injection process is rather complex and different factors may influence the results. In order to obtain experimentally reproducible data it is necessary to focus only on a specific jet region, being consistent with injection parameters. Different jet regions can be investigated separately by carefully adjusting the micrometer system orienting the injector tube (Section 2.3).
The main focus of this section are results published in the work Alois et al., 2017 [92], where the outer jet region (highly electrified particles interacting with the injector tube) was investigated.
When looking only at the outer highly electrified particles, they are all charged with the same polarity and show a similar surface charge concentration independently on particle size (Fig. 3.7): in other words, the charge on a particle q increases with r^2 (i.e. its surface area). This value is measured to be

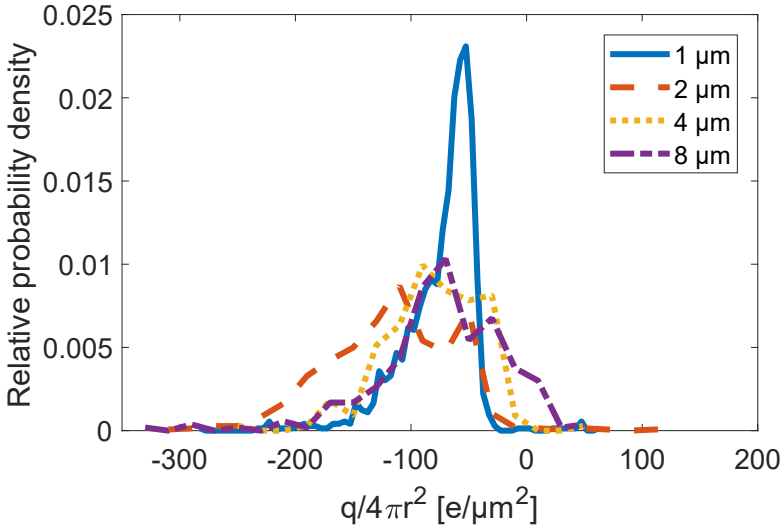

Figure 3.7: Results for the surface charge concentration ($\sigma = q/4\pi r^2$) for multiple experiments of 4 different sizes of spherical silica micro-spheres (1, 2, 4 and 8 μm). Despite a certain width in the distributions and the presence of some relatively low electrified particles, a common central high concentration is observable with a value around -100 $e/\mu m^2$.

around $\pm 100 e/\mu m^2$ ($\pm 0.02 mC/m^2$) if the charge is assumed to be uniformly distributed over the entire particle surface. The results here typically consisted of several repeated injections with the same particle type and injection conditions, with 20 - 700 individual grains counted per injection. In Fig. 3.8 the respective size distributions for silica microspheres are shown: specifically for the 1 μm sample, a second peak towards higher size is observable, presumably due to the effect of aggregation as also discussed in Section 3.3.
Although a maximum electrification per particle was expected from previous studies (Section 1.1.7), for μm size particles to attain a narrow range and size-independent surface charge concentration was unexpected. The charge/grain of around $500 - 30000e$ is in reasonable agreement with previous studies, e.g. [16].

Other combinations of powder sample/injector tube material have been tested, specifically: soda lime glass spheres (SLG) in steel, tungsten in borosilicate glass, aluminium oxide in quartz and copper in borosilicate glass (Table 3.1). Results (Fig. 3.9) show a similar (i.e. same order of magnitude) maximum surface charge concentration of around $\pm 100 e/\mu m^2$. This is not peculiar to

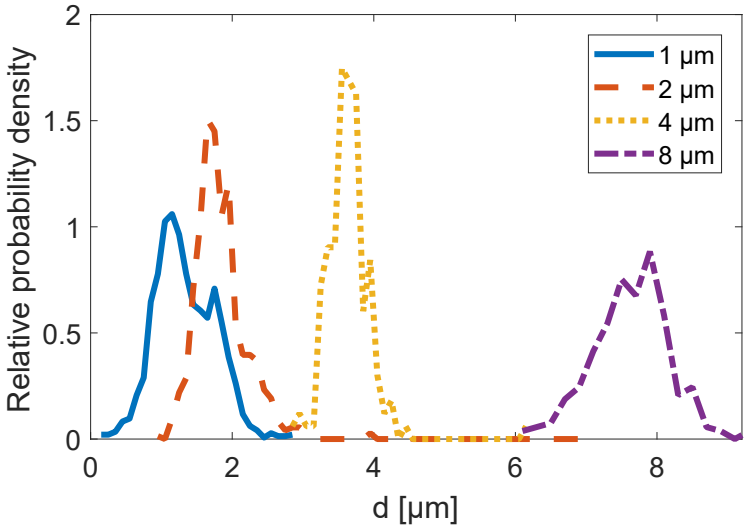

Figure 3.8: Measurements of the size (diameter) of silica microspheres using the LDV-based technique (Section 2.4) for particles with nominal sizes of 1, 2, 4 and 8 μm (shown as respectively; blue solid, red dashed, yellow dotted and purple dash-dot lines).

the use of a specific combination of tube/particle material, and indicates that for most of the combination used here a maximum limit was reached for the surface charge concentration on a single particle. Interestingly Al_2O_3 and Cu particles were positively electrified (oppositely to every other combination). Measured values are listed in Table 3.1

In Figure 3.10 the size of individual SiO_2 microspheres is plotted against surface charge concentration σ. Next to the x and y axis are shown the respective KDE (Kernel Density Estimate), which estimates a probability density function.
From Fig. 3.10 it can be seen that some of the measured particles were positively electrified. The ratio:

$$\frac{N(\sigma_-)}{N(\sigma_+)+N(\sigma_-)} = 0.985 \tag{3.2}$$

expresses the fraction of negatively charged particles with respect to the total number of counted particles, where $N(\sigma_-)$ and $N(\sigma_+)$ are respectively the number of negative and positive grains. It is unlikely that these positively mea-

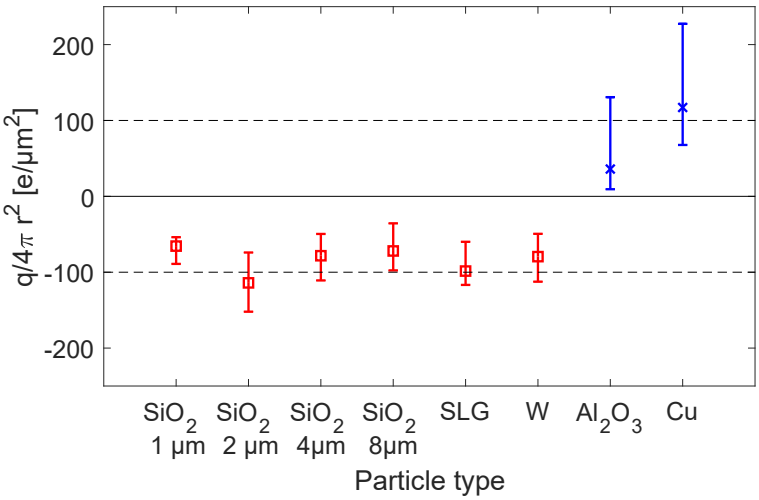

Figure 3.9: Surface charge concentration for repeated measurements of various combination of particle/injector tube composition and particle size (more information in Table 3.1). For the surface charge concentration σ the median value is presented, and error bars denote the first and third quartiles (i.e. 50% of the distribution) expressing the width of the distribution. Quartiles are used instead of the standard deviation, because typically these distributions are asymmetrical. The standard error on the median value was typically between 1-10%.

sured particles can be the result of uncertainty in the experimental measurements: counts within a time $t = 2\tau$ before and after the polarity switch time were in fact deleted from the measurement, and from Eq. 2.7 it can be seen that for $t = 2\tau$ particles should have already changed their direction of motion and reached $\approx 73\%$ of their terminal velocity in the horizontal direction. It is then statistically likely that all particles have reached the correct polarity during their motion. Moreover, it should be noted that the polarity-switch period is ≈ 0.1s (10Hz), much larger than the time constant τ, typically of the order of $1-2$ms for a 4μm particle.

The focus in this section was on the charge exchanged between particles and the injector tube wall, whereas in order to look for particle-particle electrification the setup should be modified. This can potentially be done e.g. applying a higher voltage on the electrodes in order to enhance drift velocity (particle-particle contact develops lower charging), and somehow modify the

Table 3.1: In this table results are reported for the simultaneous measurements of size and particle electrification using the LDV-based technique (Section 2.4). The combinations used for particle composition, particle size and injector tube composition are listed. For the size, the mean and standard deviation are given both as quoted by the manufacturer and as measured. Note that for copper and tungsten the size given by the manufacturer was found to be poorly constrained (see Section 2.8). For the measured charge (q) and surface charge concentration (σ) per particle the median value is given together with the first and third quartiles (in brackets) as an expression of the width of the distribution rather than the standard deviation, because of the typically asymmetric distributions.
[1] The samples are not spherical
[2] Injected from the top of the environmental chamber

Particle type	**Injector material**	**Nominal d** [μm]	**Measured d** [μm]	**q** [$10^3 \cdot e$]	**q/4πr²** [e/μm^2]
Silica 1 μm	Steel	1.18 (0.03)	1.33 (0.42)	-0.4 (+0.1 -0.2)	-66 (+12 -23)
Silica 2 μm	Steel	1.86 (0.06)	1.85 (0.44)	-1.1 (+0.4 -0.6)	-114 (+40 -38)
Silica 4 μm	Steel	3.62 (0.2)	3.64 (0.32)	-3.1 (+1.0 -1.0)	-78 (+29 -33)
Silica 8 μm	Steel	7.75 (0.3)	7.63 (0.54)	-12.3 (+5.8 -5.3)	-72 (+36 -26)
Soda lime glass	Steel[2]	1-8	2.19 (1.55)	-0.9 (+0.4 -0.6)	-98.5 (+39 -18)
Copper	Glass[2]	< 5	4.90 (3.54)	+5.1 (+11.5 -2.8)	+117 (+110 -49)
Tungsten[1]	Glass[2]	1-5	7.22 (4.67)	-7.6 (+5.7 -15.2)	-80 (+30 -33)
Al Oxide[1]	Quartz	4.6 (mean)	4.54 (1.35)	+2.7 (+3.9 -2.1)	+36 (+95 -27)

aerosolizing system to reduce particle-wall interactions.
Conversely, increasing the decompression pressure ratio (i.e. the mass of aerosolizing gas) would be expected to enhance the probability of collisions between particles and the injector wall (see Section 5.2), ideally reaching a plateau where every particle has experienced one or multiple contacts with the tube (i.e. has reached a maximum charging). However, when using the LDV technique, high decompression pressure ratio lead to the generation of an highly turbulent jet inducing velocity fluctuations in the electrodes region, thus affecting the results.

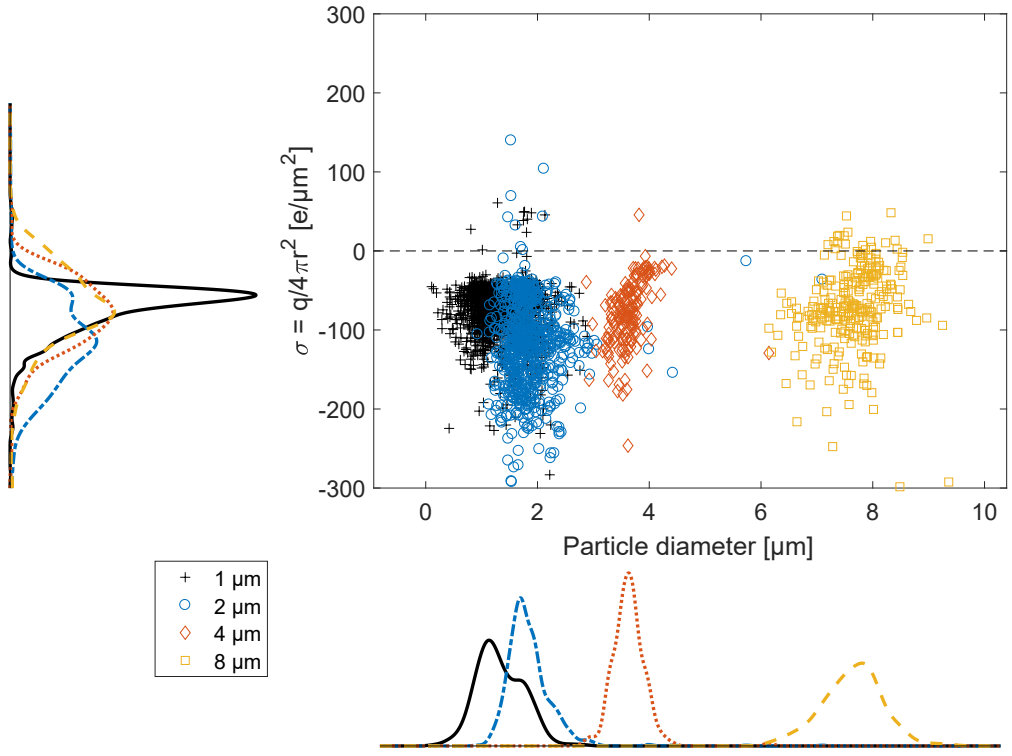

Figure 3.10: Scatter plot of the measured surface charge concentration against particle diameter of individual 1,2,4 and 8 μm silica microsphere particles. Next to the axis are plotted the respective distributions with the same color code.

3.2 Size dependence over the entire particle cloud

Simultaneous determination of size and charge of single grains in the previous Section (3.1) have shown how the charge on a particle scales linearly with its total surface area (i.e. $q \propto r^2$) and that a maximum surface charge concentration $\sigma = \pm 100 e/\mu m^2$ is reached for particles interacting with the injector tube surface.
In this Section, the average charge is measured over the entire particle cloud (inner + outer jet) using the Faraday tube technique (Section 2.5). These results have been published in Alois et al., 2018 [107]. When using this technique, the probability of contacts between particles and the injector tube wall is greatly enhanced as the injection over-pressure is higher (p_{0i} = 1000mbar and p_{ch} = 2.5mbar): this observation is supported by results shown in Section 5.2.
Various particle compositions were investigated with several mean particle sizes (Table 3.2); specifically they were SiO_2, Al_2O_3 and Soda Lime Glass (SLG). The total measured charge is expected to be dependent upon the mean size of the powder sample and the particles/injector chemical composition.
In order to isolate the size dependence (excluding the dependence upon chemical composition) these sets of measurements were normalized to the charge measured using a mean particle size of $\approx 4\mu$m, for which all compositions were available. In this way it is possible to look exclusively for the relative trend of particles sorted in different size ranges. The relative charge/volume variation with mean particle size is shown in Fig. 3.11, using both injectors in Al_2O_3 and SiO_2.
The mean particle surface charge concentration is calculated using Eq. 2.13, reported here for convenience:

$$\sigma = \frac{Q\rho_p r}{3M} \tag{3.3}$$

Where Q is the total measured charge (should not be confused with the single particle charge q), ρ_p is the particle density, r is the mean particle radius and M is the total injected mass.
If a constant surface charge concentration σ is expected, the total measured charge per volume $Q\rho_p/3M$ should vary as $1/r$ (see Eq. 3.3). Results showed in Fig. 3.11 confirm this trend for grains larger than around 1μm.
However, for sub-micron particles the charge per volume was seen to decrease (apparently linearly) with size. A likely explanation is that in this size range ($< 1\mu$m) the particles strongly cohere (i.e. form aggregates) or adhere to the injector tube wall and can not be fully dispersed, causing reduced aerosolization:

Table 3.2: A list of the samples used during experiments using the Faraday tube technique. Mean particle size, absolute generalized relative electronegativity and measured surface charge concentration values are reported. Silica microspheres generally have narrow particle size distribution, whereas other samples have broader distributions (see Table 2.1 for more details).

Sample	**Mean diameter** [μm]	χ_{AG} [eV/e]	**Al_2O_3 injector** σ [e/μm^2]	**SiO_2 injector** σ [e/μm^2]
SiO_2 (spherical)	0.166	52.2	-4 ± 1	-3 ± 0.4
SiO_2 (spherical)	0.260	52.2	-7 ± 3	-8 ± 1
SiO_2 (spherical)	0.500	52.2	-25 ± 8	-23 ± 6
SiO_2 (spherical)	1.18	52.2	-49 ± 11	-22 ± 2
SiO_2 (spherical)	1.86	52.2	-156 ± 43	-15 ± 5
SiO_2 (spherical)	3.62	52.2	-97 ± 20	-30 ± 2
SiO_2 (spherical)	7.75	52.2	-142 ± 20	-45 ± 5
Al_2O_3 (non-spherical)	4.6	34.3	-16 ± 2	+90 ± 7
Al_2O_3 (non-spherical)	9.4	34.3	-30 ± 2	+63 ± 5
Al_2O_3 (non-spherical)	17	34.3	-14 ± 5	+26 ± 1
Al_2O_3 (non-spherical)	27	34.3	-15 ± 2	+37 ± 2
SLG (spherical)	4.5	36.6	-63 ± 6	+52 ± 5
SLG (spherical)	11.8	36.6	-51 ± 8	+77 ± 13
SLG (spherical)	47.0	36.6	-35 ± 3	+41 ± 8
TiO_2 (non-spherical)	6.1	42.2	-55 ± 11	+6 ± 1

both physical processes would be expected to reduce the measured charge per volume and are supported by direct experimental observations, shown in the next Sections 3.3 and 3.4.
For this reason, samples with a mean size in the sub-micron range have not been included in the composition dependence study (Section 4.1). The measured σ values including sub-micron particles are reported in Table 3.2.
In addition to the measurement uncertainties (errors on M and Q, see Section 2.5), here the use of samples with broad size distribution and non-spherical shape constitutes an additional source of uncertainty on the determination of an effective mean particle size.

3.3 Aggregates charge and size

Cohesive agglomerates of particles (aggregates) can be present in a broad size-range, from two individual grains sticking together to mm size aggregates. Dif-

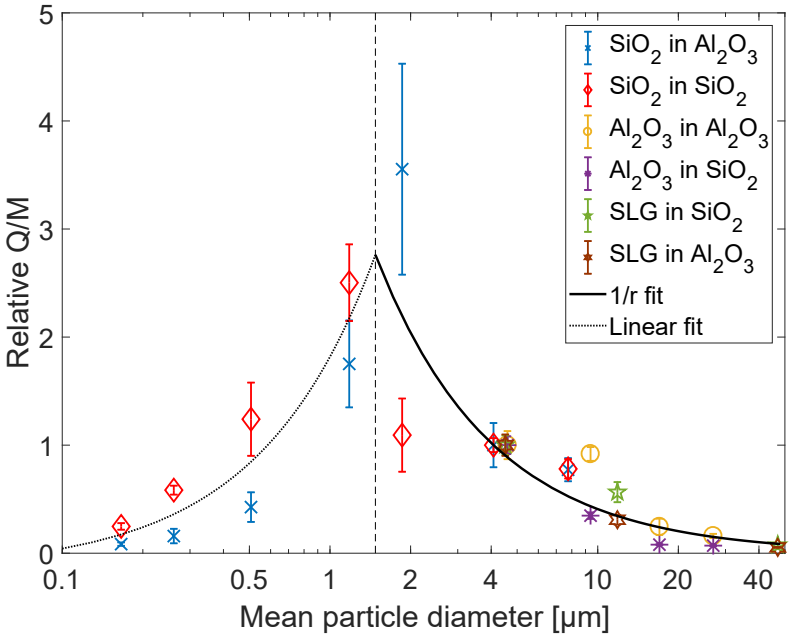

Figure 3.11: Relative charge per mass plotted for various mean particle sizes. The results were normalized to the charge/mass measured for samples with mean particle size of around 4μm, for which all compositions were available. A $1/r$ dependence can be observed for particle sizes > 1.5μm, while a linear decreasing trend is observed for particles < 1.5μm.

ferent measurement techniques are sensitive to diverse aggregate size: the LDV technique is able to measure the charge of aggregated particles with a settling velocity within the selected LDV velocity range (i.e. with a size relatively close to single particles). As discussed in Section 2.4, such aggregates would appear as a distribution of particles with increased size: for this reason, they may be distinguished from single particles only when measuring samples with narrow size distribution and spherical shape.
The charge of large (> 100μm) aggregates could be detected combining the use of an high speed camera and the injector tube voltage measured using the Faraday tube technique. Here limitations are represented by the camera resolution (i.e. the pixel size), the power/position of the light source and the distance between the camera lens and the injector outlet.

For the finer particles (e.g. 1μm diameter) electrified particles with a mea-

sured terminal velocity (i.e. size) larger than the corresponding monodisperse particle size were often seen (see Fig. 3.10): this was presumably due to small aggregated particles, an effect which was also observed in the size distribution (e.g. the size distribution of 1 μm silica microspheres in Fig. 3.8 have a second peak at around 2 μm).

For large aggregates (> 100μm) the voltage generated on the injection tube was combined with an analysis of the high speed camera video during the aerosolization process (Fig. 3.12): the camera films the nozzle from the side (panel b in Fig. 2.21) allowing to quantify the mean pixel intensity (proportional to the mass flow rate of particles leaving the injection tube) for each frame as a function of time, within a volume ($\approx$ 400mm^3) right outside of the nozzle. This technique works best at low overpressure injections, which are less turbulent and last longer, where the camera's achievable frame rate is enough to resolve the particle flux with a good resolution. Aggregates usually began to be ejected later in time with respect to single particles, presumably due to their larger inertia.
Analyzing this time sequence in Fig. 3.12 it can be observed how the net electrical current leaving the tube is correlated with the particle flux exiting the nozzle: when a peak on the injector voltage is associated with mm size aggregate leaving the tube they are assumed to be highly electrified; if they show no detectable variation on the injector voltage they are assumed to be neutrally charged. The variation on the injector voltage caused by an aggregate could be used to estimate in first approximation the charge of the aggregate itself. Highly charged aggregates can be as high as e.g. $q_{\text{agg}} \approx -1.5 \cdot 10^8 e$. This specific aggregate was estimated from high speed video imaging to have a diameter around 1mm. Assuming a spherical shape as an approximation, a calculation of its charge per surface area could be performed and a value of $\approx$ 55e/μm^2 was found. This value is similar (presumably coincidentally) to the maximum single-particle surface charge concentration determined in Section 3.1. For this specific injection the over pressure was around $22 mbar$ and the chamber pressure around $13 mbar$.
From Fig. 3.12 it can be seen that aggregates were typically not significantly electrified. This might indicate that typically they did not interact with the injector tube.

An estimate of the large (> 100μm) aggregates mass fraction with respect to the total mass could also be quantified using the high speed camera [107]. A determination of the number and size of large particle aggregates was obtained by filming into the tube outlet (panel *a* in Fig. 2.21). A laser sheet was

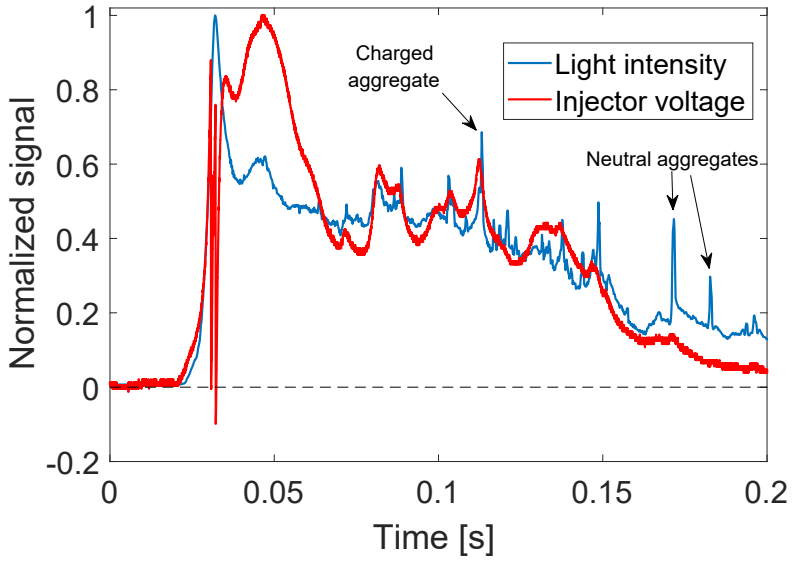

Figure 3.12: The blue line shows the light intensity observed using a high speed camera quantified as a function of time within a small (400mm^3) volume just outside of the aerosol injector nozzle. The red line shows the corresponding voltage measured on the injector tube. In this time sequence one can see that the net electrical flux leaving the tube is correlated with the observable particle flux. In addition, some of the peaks in injector voltage are associated with observable (up to mm size) aggregates leaving the tube (and are therefore assumed to be highly electrified) while others show no detectable variation in injector voltage.

used to illuminate the tube outlet and additional lighting was (if necessary) also provided by an LED lamp. From high speed videos large aggregates could be observed. The video post-processing was done determining frame by frame the number and cross sectional area of visible aggregates, using the 'Analyze particles' tool in the software 'Fiji – ImageJ' [101, 102] (see Section 2.6). This needed careful adjustment of the threshold determining the aggregate boundary. The videos from which data has been extrapolated were performed under the same light conditions (a laser sheet enlightening the nozzle outlet): this allowed to keep the parameters for the image threshold approximately constant. Only the circular portion inside the nozzle outlet was taken into account in order to avoid erroneous particle measurements from the light reflection of

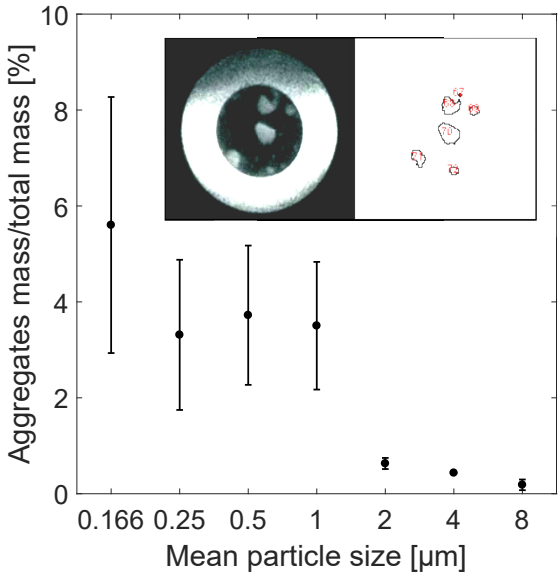

Figure 3.13: Results from image analysis of silica microspheres aggregates (> 100μm) observed with the use of a high-speed camera. The error bar indicates the variation due to repeated experiments (3x). The visible cross sectional area is used to calculate the volume of equivalent spheres, the density of the packed aggregate is measured as $\approx 400 kg/m^3$. This allows a rough calculation of the mass of visible aggregates with respect to the total (measured) injected mass. The top-right image shows a typical example of observed aggregates and the determination of its contour using Fiji-ImageJ.

the injector tube wall. As it can be observed in the top-right panel in Fig. 3.13 large aggregates could be detected with satisfying detail despite the relatively poor resolution of the imaged frames (208x208 pixels, $\approx 50\mu$m/pixel).
Results in Fig. 3.13 confirmed that large aggregates are increasingly present for lower particle size. For Silica microspheres $\leq 1\mu$m a significant increase of the aggregates mass with respect to the total injected mass was observed. These observations might explain the reduced electrification described in Section 3.2 for particles $< 1\mu$m, as the number of single particles contacting with the injector tube wall is substantially reduced due to the effect of aggregation. It should be noted that this technique is insensitive to aggregates smaller than $\approx 100\mu m$, possibly indicating that aggregation might have a larger influence on reducing the total developed charge Q.

3.4 Adhesion to the injector tube wall

The threshold shear stress for particle removal from a surface is inversely proportional with particle size $\tau_{th} \propto 1/r$ (see Section 1.2.2, Eq. 1.21). Experimental observations supporting increased adhesion for smaller particles are discussed here.
Particles < 1μm were observed to form an adhesive layer sticking to the injector tube, even for injections at high over pressure (p_{0i} = 1000mbar in the gas reservoir and p_{ch} = 2.5mbar in the chamber). When using a quartz (transparent) injector tube a white thin layer of silica microspheres was seen after injection. Another indication for this phenomena was the generation of aerosolized particles even when injecting without adding further material.
Also, when injecting with low overpressure (e.g. p_{0i} = 10mbar and p_{ch} = 2.5mbar) using a clean injector tube surface, the first injection was seen to correspond to reduced aerosolization (this was seen both with the use of a camcorder, and from the low voltage detected on the oscilloscope tube). Repeated injections using the same overpressure were observed to increase the amount of aerosolized particles. This effect was presumably also caused by particles adhering to the injector tube surface.
These observations might also explain the reduced electrification for sub-µm particles described in Section 3.2, as it would be expected that adhesion substantially diminishes the number of single particles ejected, therefore reducing the measured charge.

This is also supported by a previous study from Matsusaka et al. [85] where it was shown that even a gas flow above 100 m/s (and >1 bar pressure) was not sufficient to resuspend a monolayer of particles < 1μm in diameter. It is likely that also in their work the fluid shear stress may have not been sufficient to overcome adhesive/cohesive effects between the particles and the surface for sub-micron grains.

Chapter 3

CHAPTER 4

RESULTS: COMPOSITION EFFECTS

In this Chapter, results of composition dependence upon particle charge using the Faraday tube technique (Section 2.5) will be presented according to the following structure:

- Section 4.1 - **Insulators:** measurements focused on the composition dependence upon contact electrification between pure oxide particles and injector tube (insulators) are shown. A linear relation with absolute generalized relative electronegativity χ_{AGR} is found.
- Section 4.2 - **Metals:** measurements of contact electrification between conductive materials (metals) are shown. A dependence over particle work function/electronegativity is investigated.
- Section 4.3 - **Volcanic ash:** the contact electrification of volcanic ash samples against insulating injector tubes is investigated.

4.1 Composition dependence in oxides: σ VS χ_{AGR}

After having determined in Chapter 3 the size dependence for grains in the size range $1-50\mu m$ (a constant surface charge concentration was found, i.e. the charge on a single particle scales with its total surface area), here a dependence on the chemical composition of contacting oxide surfaces is investigated. This was done by using the Faraday tube technique (Section 2.5) for measuring the charge exchanged using a set of various particle and injector materials. Two oxide injector materials were chosen; Quartz (SiO_2) and Alumina (Al_2O_3) and a set of oxide powder samples including SiO_2, Al_2O_3, Soda Lime Glass spheres (SLG) and TiO_2 (see Table 3.2). These results have been published in Alois et al., 2018 [107].

The adapted generalized electronegativity model (χ_{AGR}) described in Section 1.1.6 was seen to appear linearly correlated with the measured surface charge concentration for these oxide samples, as it is shown in Fig. 4.1. An equation linking the surface charge concentration on a particle σ to its absolute generalized electronegativity relative to the injector material is derived applying a linear least square fit method:

$$\sigma = \frac{q}{4\pi r^2} = \frac{Q\rho_p r}{3M} = a\chi_{AGR} + b \tag{4.1}$$

Where $a = 4.7 \pm 0.9 e/\mu m^2/V$, $b = -27 \pm 10 e/\mu m^2$ ($a = 7.54 \cdot 10^{-7} \pm 1.4 \cdot 10^{-7} C/m^2/V$ and $b = -4.29 \cdot 10^{-6} \pm 1.7 \cdot 10^{-6} C/m^2$), with a coefficient of variation $R^2 = 0.86$. A clear correlation is observed between surface charge concentration σ and absolute generalized relative electronegativity χ_{AGR}.
In Fig. 4.1, samples with the same chemical composition but different mean particle size are plotted with distinct marker sizes. It would be expected that these points all coincide towards the same value (i.e. constant σ), although some span can be seen (corresponding to the same span observed for size dependence in Fig. 3.11, Section 3.2). This is presumably due to the measurement uncertainties listed in Section 2.5, uncertainty in the determination of particle mean size and/or the influence of aggregation and adhesion to the injector tube causing reduced aerosolization (investigated respectively in Section 3.3 and 3.4).
Remarkably, the measured surface charge concentration per particle (σ) is generally within the range $\pm 100 e/\mu m^2$, as expected from the limit determined using the single-particle LDV technique in Section 3.1.
The b parameter (i.e. vertical offset in Fig. 4.1) represents the average surface charge concentration that a particle acquires when contacting against the

same injector tube material. Interestingly this behaviour is seen to be consistent also for metals (Section 4.2) and volcanic ash (Section 4.3).
As will be discussed in Section 6.4, this correlation is in good quantitative agreement with previous experimental studies [42, 43] and also with prediction from purely theoretical considerations based upon estimation of the contact area, leading to a predictive equation for estimating contact electrification, shown in Section 6.1.
By expressing electronegativity in an absolute scale (in eV/e) the absolute generalized relative electronegativity χ_{AGR} may be classically interpreted as an effective contact potential difference between the two surfaces, as will be discussed in Section 6.1.

For compound materials (e.g. Soda Lime Glass) the expression for the absolute generalized electronegativity χ_{AG} was adapted to take into account the composition of such compound. An effective χ_{AG} can be estimated by knowing the chemical composition of the compound material using the formula:

$$\chi_{AG} = \sum_{i=1}^{n} (1 + 2Z_i)\chi_{M,i} N_i \tag{4.2}$$

Where $\chi_{M,i}$ and Z_i are respectively the absolute electronegativity and valence for each 'anionic' component of the compound and N_i is the molecule number percentage of each component in the oxide ($N_i = 1$ for pure oxides). This formula assumes that each component contributes linearly with its molecule number percentage to the total electronegativity. The number of molecules for each oxide composing the sample is calculated taking into account the molar mass through the expression:

$$N_i = \frac{w_i}{m_p \alpha} n_i \tag{4.3}$$

where w_i is the weight percentage, m_p is the mass of a proton, α is the molar mass of the compound and n_i is the number of 'anions' in a molecule of the compound (e.g. $n_i = 2$ for Al_2O_3 and $n_i = 1$ for SiO_2).
This quantitative relation can potentially be used to predict the electrification of every compound insulator, knowing its chemical composition.
In the work of Tamatani [108] this idea was already formulated, though only qualitatively, as Tamatani writes: "*the charging tendency of a material even with a complex chemical composition can be predicted, though qualitatively, by taking into account the electronegativities of the constituent metal ions*" [108].

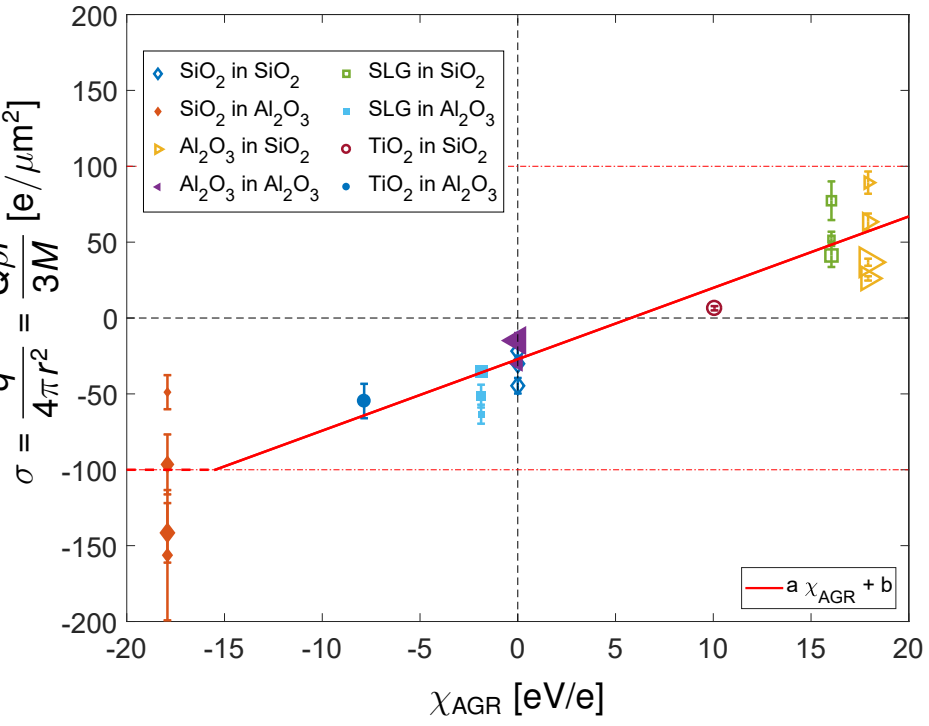

Figure 4.1: The surface charge concentration is plotted against the absolute generalized relative electronegativity (in eV/e). The linear model presented in Eq. 4.1 is plotted in red. Upper and lower limit at $\pm 100 e/\mu m^2$ represents the upper and lower limits for this model, determined using the LDV technique for charge measurement on single particle (Section 3.1). Different marker sizes represents different mean particle sizes (see Table 3.2 for more info).

4.2 Metals

As discussed in the introduction, Section 1.1, in literature contact electrification between metals is commonly accepted to be due to electron transfer, and was shown by Harper [26] to scale linearly with electron work function determined by contact potential difference (CPD). However, work function values found in literature for various elements highly differ depending on the measurement technique and the crystal-face orientation. For our samples, we assume the particles to be polycrystalline. Ideally, the best technique for measuring work function values related to this work would be the contact potential difference (CPD) for polycrystalline metals. Nevertheless, in literature CPD values are not available for every metal. Work function for polycrystalline surfaces has also been calculated with theoretical models (Halas & Durakiewicz, 1998 [29]). A reliable source for measured values can be found in the CRC Handbook of Chemistry and Physics [109].
Here for simplicity a range of 2 values is taken into consideration (see Table 4.1), which do not differ greatly from one another:

- Accepted measured values (CRC Handbook [109])
- Calculated values (Halas & Durakiewicz, 1998 [29])

A set of metal powders (Table 4.1) is measured against two different reference injector materials (Copper and Stainless Steel 316L). The work function of Stainless Steel 316L was taken from a study of Barret et al. [110], where it was measured using X-ray photo-electron emission microscopy and electron backscattering diffraction as a function of the grain orientation. Here a mean value over the work function of each crystal-face orientation is assigned as the effective work function for Stainless Steel 316L.

In Fig. 4.2 the measured charge per volume is plotted against the mean particle size. Differently from the size dependence seen with oxides (Fig. 3.11, Section 3.2), Fig. 4.2 does not exclude the dependence upon particle composition as the samples were not available in multiple mean sizes. Despite composition was not excluded, the plot in Fig. 4.2 shows that a trend of increasing Q with $1/r$ is still observable.
The measured surface charge concentration (σ) values are plotted in Fig. 4.3 as a function of the relative metal work function between injector and particle material, considering as the x axis errorbar the span between work function values found the CRC handbook [109] and in the work of Halas & Durakiewicz [29]).

Table 4.1: List of metal particles used.

Sample	Mean diameter $[\mu m]$	Work Function $[eV]$	χ_A $[eV]$	Copper tube $q/(4\pi r^2)$ $[e/\mu m^2]$	Steel tube $q/(4\pi r^2)$ $[e/\mu m^2]$
Pt	1.76	5.55-5.65	7.0	-147±6	-135±17
Fe	4.1	4.50-4.61	5.6	-58±5	-47±6
W	7.9	4.41-4.55	7.2	-49±4	-73±2
Cu	3.4	4.65-4.69	5.8	-6±1	14±0.4
Zn	7.5	4.65-4.69	5.0	-6±2	-3±1

Interestingly, metal particles seem to resemble many of the aspects observed with oxide particles. The measured surface charge concentration is within a similar range as the one measured for oxide particles (see Fig. 4.1, Section 4.1). Also the fit line correlating work function (W) and surface charge concentration (σ) is expressed here as: $\sigma = a_W W + b_W$, where the fit constants are respectively $a_W = 86\text{e}/\mu\text{m}^2/\text{V}$ and $b_W = -60\text{e}/\mu\text{m}^2$. This shows a negative offset b_W, similarly to what observed for oxides (Section 4.1).
Copper powder in a copper injector tube was the only combination available for a particle electrifying against the same injector material, and interestingly it showed a significantly lower negative charge (around $-6\text{e}/\mu\text{m}^2$) compared to that observed for oxide particles against the same reference material (around $-27\text{e}/\mu\text{m}^2$ using SiO_2 in a SiO_2 tube and Al_2O_3 in Al_2O_3 tube).
The poor determination of work function for this specific set of metal powders/injector tube might explain why the correlation between work function and surface charge concentration in Fig. 4.3 is less clear than the one observed with oxides.
An effort to use clean, non-oxidized surfaces was made in order to avoid contaminations that could change the effective work function. However, it is unlikely that the oxidation process is entirely avoided for some of the samples used here (Cu, Fe, Zn). This might also contribute to the poor correlation seen in Fig. 4.3 (see Section 2.7 for more details).
The measured σ can also be plotted against the absolute relative electronegativity χ_{AR} (Fig. 4.4). Again here a tendency for a linear trend may be observed, expressed as: $\sigma = a_\chi \chi_{AR} + b_\chi$, with the fit constants respectively $a_\chi = 42\text{e}/\mu\text{m}^2/\text{V}$ and $b_\chi = -32\text{e}/\mu\text{m}^2$. Again a negative offset b_χ is seen, surprisingly close to the one observed for oxides ($b = -27\text{e}/\mu\text{m}^2$) (Section 4.1).
Differently from oxides (Section 4.1), here the calculation of a generalized electronegativity using Eq. 1.4 looses its physical meaning because of the differ-

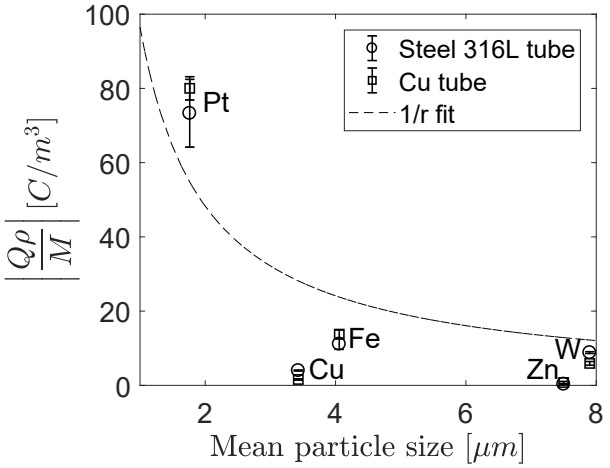

Figure 4.2: Mean particle size of metal powder plotted against the absolute value of charge per volume $\left|Q\rho_p/M\right|$. The fit curve is of the form $f(r) = a/r$ where $a = 48.3$, with a goodness of fit $R^2 = 0.65$.

ence at a molecular level between a metal and an oxide material. It may be argued that for most of the metal samples used here an oxide layer is always present at the particle surface, but this is probably not true for some of the samples (e.g. Platinum) and the eventual oxide layer thickness is unknown, as well as its influence on contact electrification measurements.
Interestingly the absolute electronegativity can be compared with work function for each sample. From Fig. 4.5 it can be seen that these quantities have comparable magnitude, but are not entirely linearly related.

In Section 6.4 the results obtained here will be compared with measurements by Harper [26].

4.3 Volcanic ash

A set of seven volcanic ash samples from different volcanic eruptions (listed in Table 4.2) was studied using the Faraday tube technique (Section 2.5) in order to determine their contact electrification when aerosolized in SiO_2 and Al_2O_3 injector tubes. These samples have been characterized in the work of Vogel et al., 2017 [103], where their size, shape, chemical composition and optical properties were determined. The mean particle sizes reported in Table

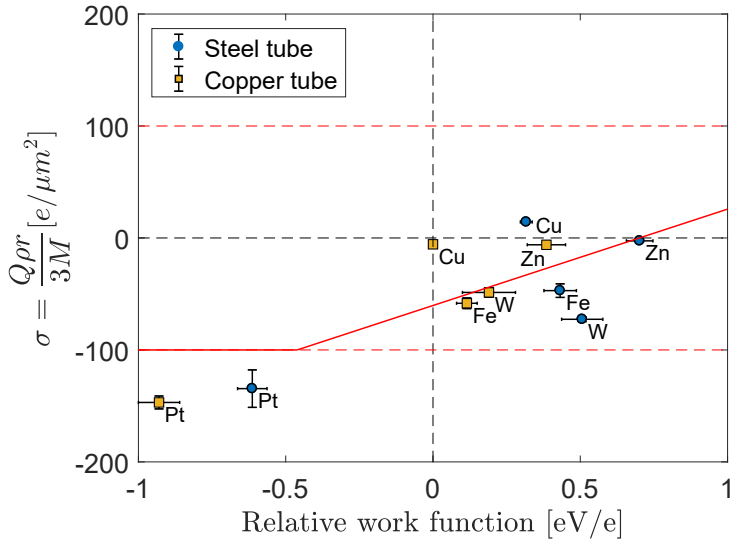

Figure 4.3: Mean Work Function values (W) plotted against particle surface charge concentration σ. The fit line is $\sigma = a_W W + b_W$, with fit constants $a_W = 86\text{e}/\mu\text{m}^2/\text{V}$ and $b_W = -60\text{e}/\mu\text{m}^2$.

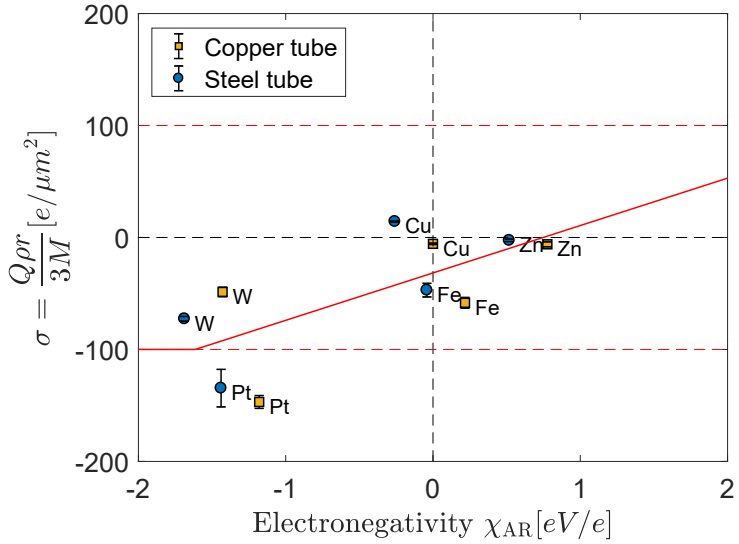

Figure 4.4: Absolute relative electronegativity χ_{AR} plotted against particle surface charge concentration σ. Fit line $\sigma = a_\chi \chi_{AR} + b_\chi$, with fit constants $a_\chi = 42\text{e}/\mu\text{m}^2/\text{V}$ and $b_\chi = -32\text{e}/\mu\text{m}^2$.

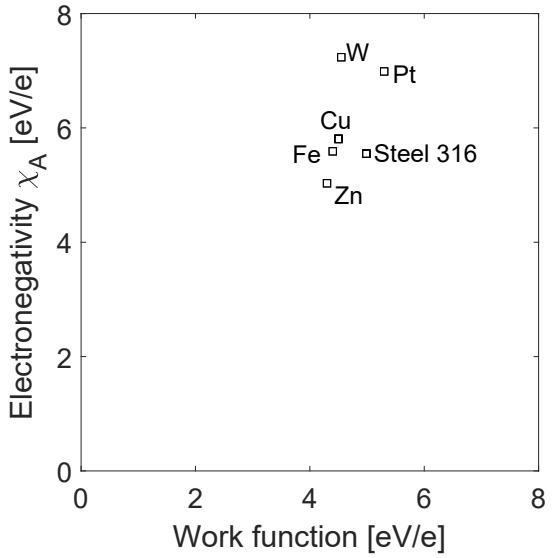

Figure 4.5: Mean Work Function value plotted against Electronegativity in Mulliken's scale χ_A.

4.2 differ from the values reported in [103]: this was done because in [103] the authors reported a particle number-weighted size distribution, whilst for this study a volume-weighted size distribution was more sensible to use.
These samples originally had a broad size distribution, and were sieved using a mesh size of 63μm, therefore obtaining a finer fraction of particles. The volume weighted size distribution was measured for most samples by Andreas Vogel using a Horiba LA 960 laser diffraction particle size analyzer, whereas specifically for the samples Eyjafjallajökull and Sakurajima the size distribution was obtained using a Multiwavelength separation analyzer (LUMISizer®) in the laboratory of INGV-Roma.

Results using the two oxide tubes (Quartz SiO_2 and Alumina Al_2O_3) show that the measured charge per volume increases following a trend inversely proportional with the mean particle size 1/r (Fig. 4.6). The fitting curves $f(r) = a/r$ have the best-fit parameter: $a = 121.6$ for the Al_2O_3 tube ($R^2 = 0.78$) and $a = 71.5$ for the SiO_2 tube ($R^2 = 0.47$). Here, as in the case of metals (4.2), it was not possible to normalize the data to a common mean particle size because the samples were available only in one size distribution, so composition effects are not excluded from the plot in Fig. 4.6. A tendency for the charge per volume to increase as 1/r is observable, indicating that size plays a dominant

Table 4.2: Surface chemical composition, mean particle size and the Dense Rock Equivalent (DRE) density for 7 different volcanic ash samples, from [103]. The mean particle size is volume weighted and the samples have been sieved with a $63\mu m$ mesh.

Sample	SiO_2 **%**	TiO_2 **%**	Al_2O_3 **%**	FeO **%**	MgO **%**	CaO **%**	Na_2O **%**	K_2O **%**	**Size** $[\mu m]$	ρ_{DRE} $[kg/m^3]$
Chaiten'08	71.5	0	16.6	1.8	0.8	2.7	3.8	2.7	19.2	2444
MSH '80	65.7	0	14.4	4.8	5.4	6.6	1.9	1.1	17.2	2611
Kelud '14	65.7	0.1	19.8	3.2	1.2	7.7	2.1	0	34.3	2777
Grims '11	55.8	2.3	15.1	11.2	3.1	7.9	3.3	0.6	42.4	2934
Spurr '92	62.0	1.9	18.2	4.1	2.7	7.6	2.2	1.5	23.1	2709
Sak '14	65.4	0.3	19.9	3.4	1.5	4.3	3.8	1.3	24.9	2801
Eyja '10	58.9	2.0	13.9	11.5	3.9	7.4	1.4	1.1	29.7	2812

role for the electrification of volcanic ash. Also, it can be seen a systematic trend for injections in Al_2O_3 tube to generate more charge than in SiO_2 tube.
In order to investigate the composition dependence, the absolute generalized relative electronegativity χ_{AGR} for volcanic ash samples was estimated in two different ways:

1. χ_{AGR} calculated assigning to every ash sample an absolute generalized electronegativity equal to the one of silica (χ_{AG} = 52.2), i.e. neglecting any minor mineral components (Fig. 4.7, top panel)

2. χ_{AGR} calculated using Eq. 4.2 (Fig. 4.7, bottom panel). This is done by knowing the surface chemical composition of the each sample (see Table 4.2), taken from Vogel et al. 2017 [103]. It should be noted here that in these volcanic samples usually none of the components is actually present in the form of pure oxides, whereas it is a standard technique to give the results of a chemical analysis not as atomic ratios but as oxides percentage. A volcanic ash particle would rather be expected to be a non uniform compound

A reasonable agreement was found with the predictive model for oxides (Eq. 4.1) by considering the particles composed of pure SiO_2 (Fig. 4.7, top panel). Conversely, a less clear correlation was found when considering minor mineral components (Fig. 4.7, bottom panel).
It appears that for volcanic ash the determination of χ_{AGR} using Eq. 4.2 does not provide an improved correlation with surface charge concentration, presumably due to the nature of such materials (which are not in the form of pure

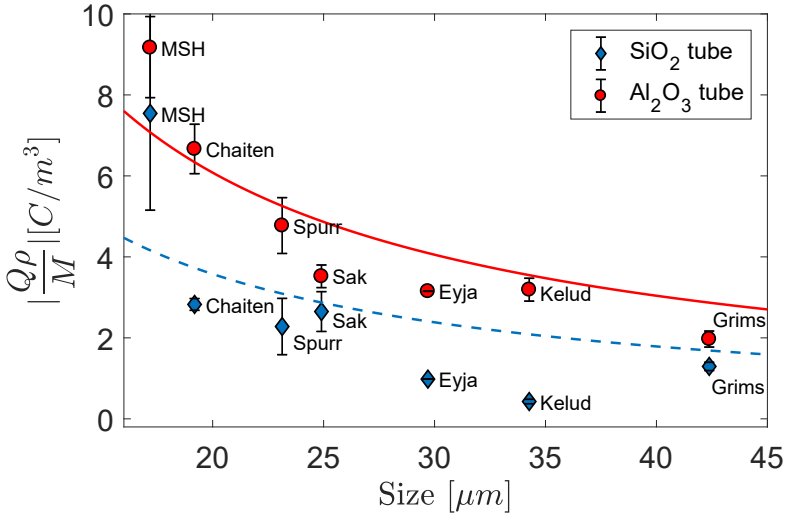

Figure 4.6: Charge/volume of volcanic ash samples in both SiO_2 and Al_2O_3 injector tubes VS mean particle size (equivalent diameter expressed in μm). The fits are of the form $f(r) = a/r$, with $a = 121.6$ for the Al_2O_3 tube ($R^2 = 0.78$) and $a = 71.5$ for the SiO_2 tube ($R^2 = 0.47$)

oxides). It should be noted that in Section 4.1 for the Soda Lime Glass compound good correlation was found using Eq. 4.2 (see Fig. 4.1).
Also, for this set of samples it rather seems that differences in their chemical composition do not lead to large changes in their generated σ, whereas the influence of the mean particle size (i.e. size dependence) appears to have a considerable effect (Fig. 4.6).

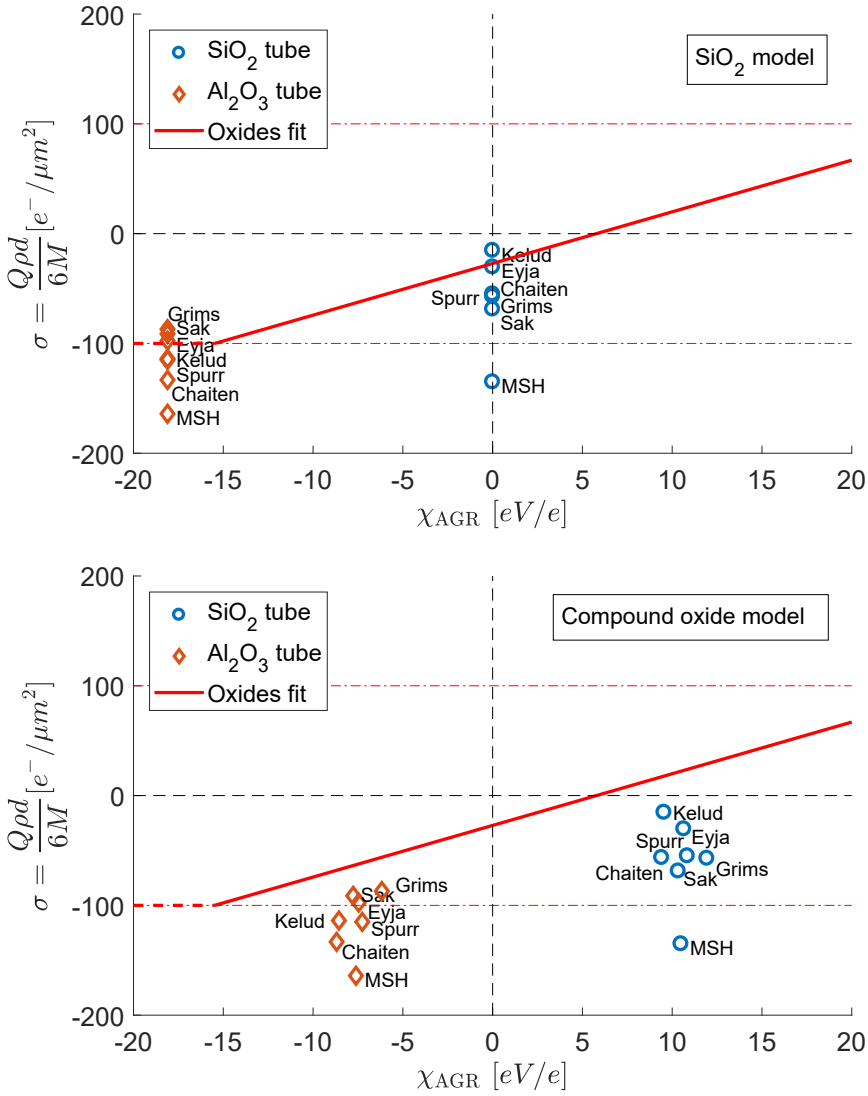

Figure 4.7: Surface charge concentration of volcanic ash samples in both SiO_2 and Al_2O_3 injector tubes plotted against the absolute generalized relative electronegativity χ_{AGR}. The red line is the model determined for oxides (Eq. 4.1). In the top figure χ_{AGR} is calculated by assigning to every ash sample an absolute generalized electronegativity equal to the one of silica $\chi_{AG} = 52.2$. In the bottom figure χ_{AGR} is estimated by taking into account the samples surface chemical composition in Table 4.2.

Chapter 4

Chapter 4

CHAPTER 5

RESULTS: AEROSOLIZING GAS PROPERTIES

In this Chapter, the contact electrification dependence upon the surrounding (aerosolizing) gas is investigated. Results will be presented according to the following structure:

5.1 **Gas dependence:** here the electrical charge acquired by silica microspheres is investigated as a function of the aerosolizing gas composition. Air, argon and CO_2 were tested.

5.2 **Effect of the reservoir gas pressure:** the measured charge is investigated as a function of the reservoir gas pressure, using air as the aerosolizing gas.

5.3 **Electrical breakdown:** electrical discharges, specifically through gas breakdown, were observed combining the measured signal from the injector tube voltage and video from the high speed camera.

5.4 **Relative humidity:** contact electrification dependence upon the gas relative humidity is studied by controlling the RH in the injector system.

5.5 **Particle electrification as a function of transit through the injection tube:** here contact electrification is studied during particle transit within the injector tube by splitting it into different individual Faraday systems or by reducing the total length of the Faraday tube.

5.1 Gas dependence

This study was conduced in order to determine whether the physical process beyond contact electrification is dependent on the aerosolizing gas properties. The dependence upon gas composition was investigated using 3 gases: specifically they were Argon, CO_2 and air. These gases were chosen because of the difference in their minimum electrical breakdown voltages according to the respective Paschen curve (Fig. 1.1). Argon has a lower minimum breakdown voltage ($\approx 140V$) with respect to air ($\approx 330V$), whereas CO_2 has a higher breakdown voltage ($\approx 420V$) [111]. If the maximum surface charge concentration of $\pm 100e/\mu m^2$ found in Chapter 3 and 4 is due to gas breakdown (i.e. discharge through gas molecules), this limit would then be expected to change depending on the Paschen curve characteristic of the aerosolizing gas.
These three gases have been tested using the LDV technique on 2 µm silica microspheres and using the Faraday tube technique on 2 µm and 8 µm Silica microspheres. In these tests the two measurement techniques were run simultaneously. The gas reservoir was set at $\approx 12mbar$, whilst the chamber pressure was $2.5mbar$.
If the process was dominated by gas breakdown, the measured particle electrification and/or the maximum particle surface charge concentration would be expected to increase by around a factor of 3 ($430V/140V$) between injections using Argon and CO_2. Results (Fig. 5.1) showed instead a much smaller variation in the measured charge using the Faraday cage technique: less than 40% increase for 2µm particles and around 80% for 8 µm particles.
Similarly, single-particle measurements using the LDV technique showed an increase in the mean surface charge concentration of $\approx$ 50% between Argon and CO_2 as aerosolizing gases (Fig. 5.2), still considerably less than a factor of 3. Remarkably an similar increasing trend is observed using both measurement techniques.
These observations are useful to constrain the possible processes causing an upper and lower limit of around $\pm 100e/\mu m^2$, which will be discussed in Chapter 6.
In addition, it should be noted that besides the minimum breakdown voltage, also the gas relative humidity may play a role in contact electrification: regarding this data set, Argon and CO_2 may be considered extremely dry; air can also be considered fairly dry (< 2% RH, see Section 5.4) when injecting with low pressure (12mbar in this case).

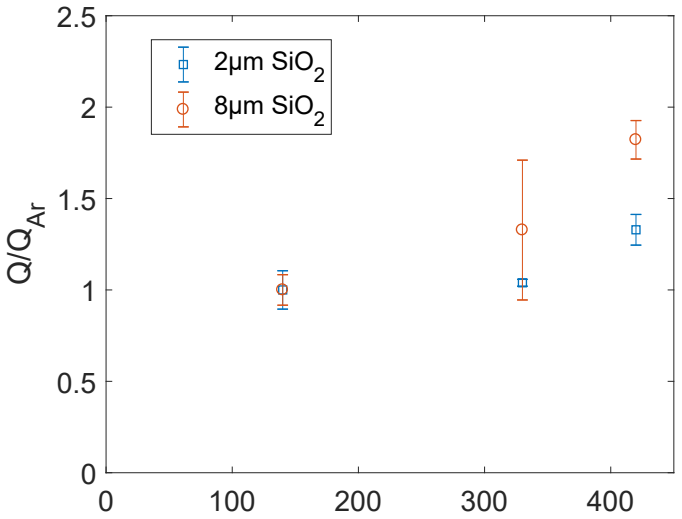

Figure 5.1: Relative measured charge VS Breakdown voltage using the Faraday cage technique of repeated (3x) injections of 2 µm and 8 µm Silica microspheres using respectively CO_2, air and Argon as aerosolizing gas. The charge was normalized to the charge measured in the Argon case, which was the lowest. Around 40% variation for the 2 µm particles and 80% for the 8 µm particles was observed. The gas reservoir pressure was fixed at 12 mbar and the chamber pressure at 2.5 mbar. The breakdown voltages are respectively $\approx 140V$ for Argon, $\approx 330V$ for air and $\approx 420V$ for CO_2 [111].

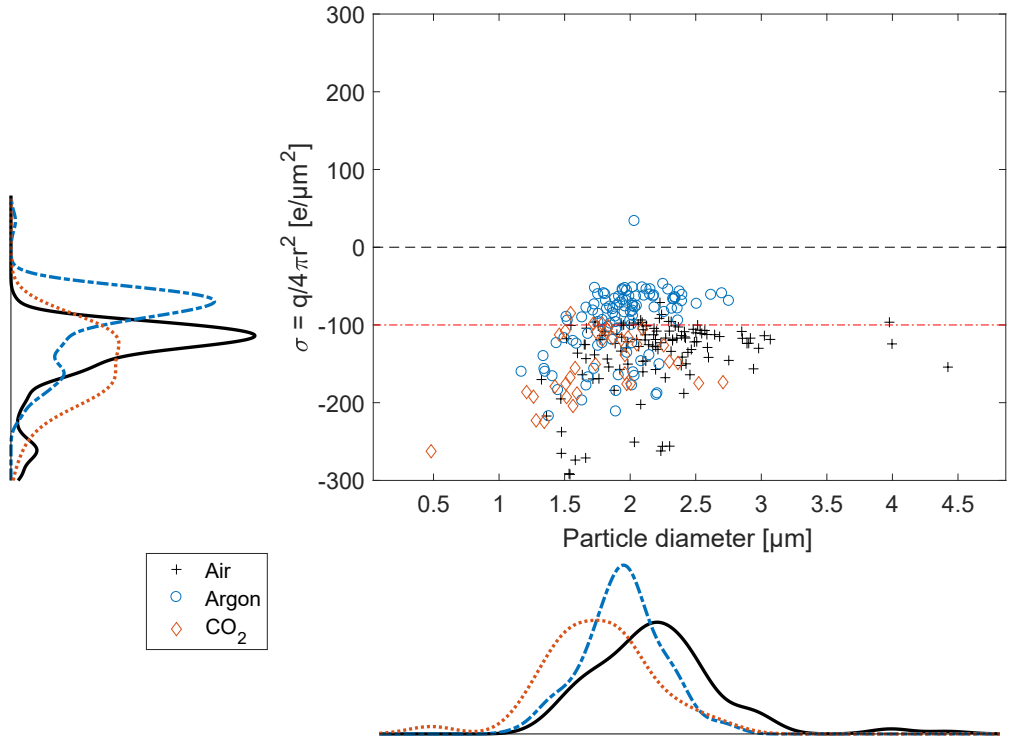

Figure 5.2: Scatter plot of the measured surface charge concentration against particle diameter of $2\mu m$ silica microsphere particles using respectively CO_2, air and Argon as aerosolizing gas. Next to the axis are plotted the respective distributions (air with full line, argon with dash dotted and CO_2 with dotted line) using the same color code.

5.2 Effect of the reservoir gas pressure

The total charge over the entire particle cloud Q was measured using the Faraday tube technique (Section 2.5) as a function of the reservoir gas pressure, using $\approx 11\mu m$ Soda Lime Glass spheres particles and the Al_2O_3 injector.
Results of the mean charge measured as a function of injection pressure are shown in Fig. 5.3: the charge considerably drops for $p_{inj} < 100mbar$, whereas no big variation is observed for higher injection pressure with a maximum value found for $p_{inj} = 100 - 300mbar$.
In Figure 5.4 measured voltage time-series are shown for various injection pressures: the highest voltage reached is observed for the injection at atmospheric pressure ($p_{0\mathrm{i}} = 1000$mbar), and gradually decreases for injections with lower reservoir gas pressure. From Figure 5.4 it can also be seen that charged particles start exiting from the injector tube progressively later in time for lower injection pressures, and keep on flowing longer. This behaviour might be due to the lower mass of gas at lower pressures (the total gas and particle mass are approximately equal at $p_{inj} = 300mbar$), corresponding to a lower amount of energy released; also, particles might keep on flowing longer due to their momentum even when the gas flow has ended, while in the highest pressure case most of the particles might have already been aerosolized inside the chamber when gas was still flowing along the tube.
Interestingly, the Reynolds number characteristic of the pipe flow can be estimated as a function of the injection pressure, solving the Fanno flow equation introduced in Section 1.2.1. The transition Reynolds number for laminar to turbulent flow in a pipe is generally within the range $2000 < Re_D < 4000$ [112]. For initial reservoir gas pressure of $p_{0\mathrm{i}} = 1000mbar$ and $p_{0\mathrm{i}} = 300mbar$ the tube Reynolds number is estimated to be in the turbulent regime (respectively around $Re \approx 3.5 \cdot 10^4$ and $Re \approx 1 \cdot 10^4$), whereas already for $p_{0\mathrm{i}} = 100mbar$ the estimated Reynolds number falls into the transition regime (around $Re \approx 3 \cdot 10^3$), and for $p_{0\mathrm{i}} = 30mbar$ should drop within the laminar regime (around $Re \approx 7 \cdot 10^2$). This might indicate that the number of collision undergoing between particles and injector tube during the injection process is substantially reduced in the laminar flow regime, thus reducing the measured charge.
In addition, an order of magnitude calculation can be performed estimating the threshold shear stress necessary for particle resuspension from the tube surface and the fluid shear stress (see Section 1.2.2). Eq. 1.21 would predict a threshold shear stress $\tau_{\mathrm{th}} \approx 0.3Pa$ for a spherical particle with diameter $2r = 11.8\mu m$. The threshold shear stress τ_{th} can then be compared with the fluid shear stress exerted on the tube surface at a low pressure gas injection (e.g. $p_{0i} = 30mbar$, resulting in a mean gas density in the tube from Eq. 1.16 of

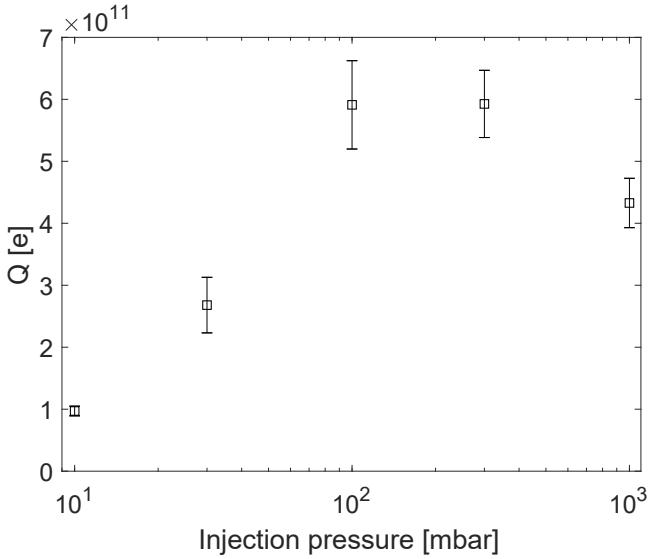

Figure 5.3: Mean and standard deviation of the total measured charge as a function of the injection pressure. A decreasing trend is observed for $p_{inj} < 100mbar$, where a transition from turbulent to laminar flow is expected.

$\rho_g \approx 0.013 Kg/m^3$). By estimating U_* from Eq. 1.20 (Section 2.3.1), this (rough) estimate would give a fluid shear stress $\tau_f \approx 4Pa$. As $\tau_f \gg \tau_{th}$, this calculation would then predict particle resuspension (lifting) from the inner surface of the tube, as experimentally observed.
It is worth remarking that electrical breakdown was seen for $p_{0i} \leq 100mbar$ (see Fig. 5.4) in the form of fast drops in the measured voltage. These aspects will be examined in Section 5.3.

5.3 Electrical breakdown

Electrical discharges could be detected from the measured oscilloscope voltage as rapid and intense downwards spikes, typically $> 1V$, which could not be resolved with the oscilloscope time resolution Δt (usually $\Delta t = 3.2\mu s$).
The discharge signal appears to be different when injecting with high pressure (Fig. 5.5) or with low pressure (panel b in Fig. 5.7) in the gas reservoir: at high pressure they were less in number but with an higher voltage change, at low pressure they appeared to be more frequent but less intense (see also Fig. 5.4). The charge associated with a discharging event could be quantified by integration of the corresponding voltage time-series. Generally, at high pressure

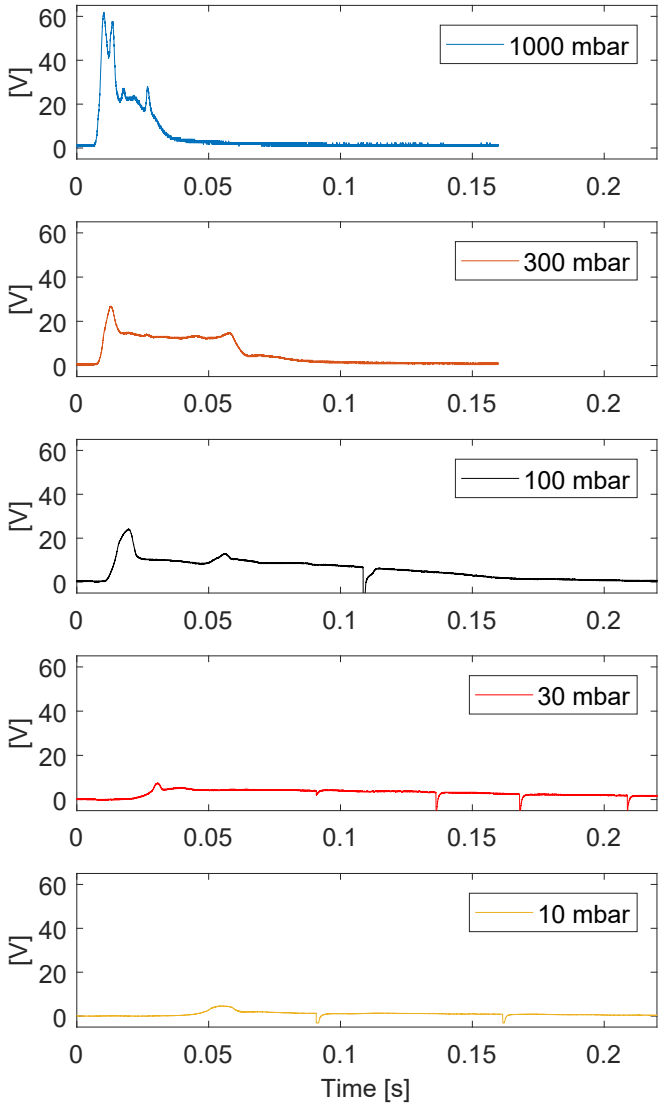

Figure 5.4: Time series of the measured voltage on the injector tube varying the injection pressure. The maximum voltage generated decreases with injection pressure; electrified particles start exiting the injector tube later in time at lower p_{inj}, and they keep on exiting longer.

discharges were observed only in case of high electrification and did not exceed 6% of the total measured charge. In the worst case event (Fig. 5.5) the total charge lost due to discharges was ≈ 16%. Such intense events could also be observed with the high-speed camera, as shown in Fig. 5.6 in the form of light in the nozzle, and they were visible for a single frame (the frame rate was usually 4000 fps). As a discharging event happening within the injector tube would be invisible with the Faraday cage, it is suspected that in these cases the highly electrified particle cloud that already left the tube breaks down through the gas to the tube, even though there is no direct experimental evidence for it. Interestingly, the first three discharging events in Fig. 5.5 are followed by a time interval in which no electrical charges are leaving the tube for around $2.5ms$. This time interval is comparable to the characteristic time that a fluid particle takes for traveling across the injector tube, estimated as $\tau_{gas} = L/\overline{U} \approx 1.9$ms where L is the length of the injector tube and $\overline{U}$ is the mean flow velocity (see Section 2.3.1). This might be due to gas breakdown initiated by the electrified particle cloud that has already been injected into the chamber. Such discharge would then propagate inside the injector tube and discharge particles that are still inside it, which do not show electrical charge when exiting the Faraday tube system.
With injections at low pressure no visible light was associated with a detected breakdown event.
When using insulating injector tubes, the copper tape enclosure was around $2cm$ shorter than the full length of the tube ($50cm$): this was done in order to test if discharging occurred at the tube outlet. No difference was observed after the removal of the last $2cm$ of copper enclosure, indicating that gas discharges do not always occur/initiate at the nozzle.

5.4 Relative humidity effects on electrification measurements

When using the Faraday tube technique with high injection pressure in the gas reservoir, the relative humidity seen by the particles during the aerosolization was poorly constrained. In fact, whereas low-pressure air within the chamber had a low relative humidity due to the low water vapour partial pressure (i.e. $RH < 2\%$), the reservoir gas was at ambient relative humidity (poorly constrained, generally $RH \approx 50\%$). The rapid gas decompression during the injection process within the tube makes it difficult to determine the relative humidity seen by the particles. For this reason, a dedicated investigation was

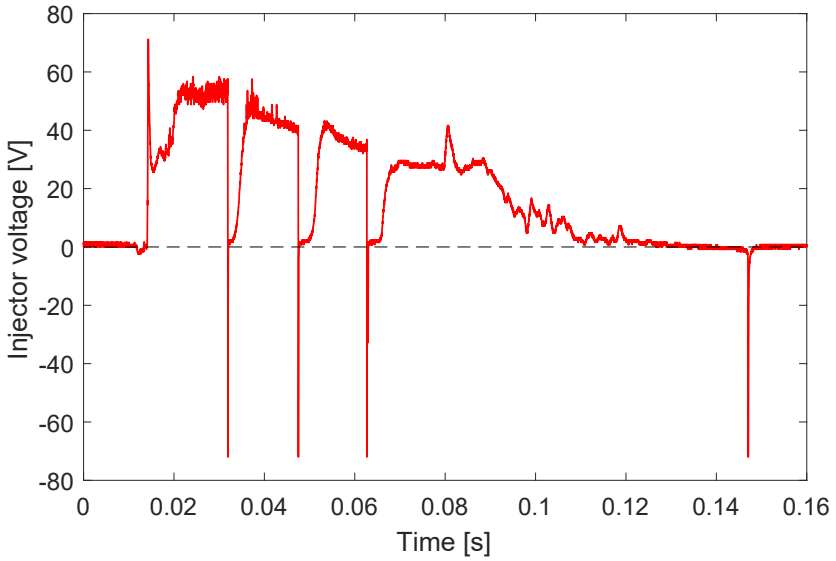

Figure 5.5: An example of the measured injector voltage for Silica Microspheres (μm) in Al_2O_3 tube (Injection pressure: $1bar$. Chamber pressure: $2.5mbar$). The sampling frequency is $625kHz$. In this (extreme) case the total measured charge $Q = -1.64 \cdot 10^{12} e$, and the total charge lost due to visible discharges (lightning) $Q_{lost} = -2.76 \cdot 10^{11} e$. Visible lightning were detected with the high speed camera. The flat region following discharge is interpreted to be as a time interval in which particles exiting the tube are neutral due to the diffuse discharge happened inside the tube.

conduced with a proper control over the relative humidity [107].
$RH < 1\%$ during the whole injection process could be achieved using dry Argon gas both within the environmental chamber and the gas reservoir. $RH \geq 50\%$ was achieved using $\approx 12mbar$ of pure water vapour in the chamber (corresponding to $RH \simeq 50\%$) and ambient air at $RH \simeq 50\%$. With all three conditions (low, high and unconstrained RH) the chamber pressure was kept at $12mbar$.
Two different samples, specifically $4\mu m$ Al_2O_3 and $2\mu m$ SiO_2, have been tested using a SiO_2 injection tube. The results of these tests are shown in Table 5.1. A good agreement upon the measured charge is seen between the low humidity and the unconstrained case, indicating that in these experiments the particles/surfaces may be considered dry as expected. Regarding the high-humidity case, little difference was observed for Al_2O_3, however for the SiO_2

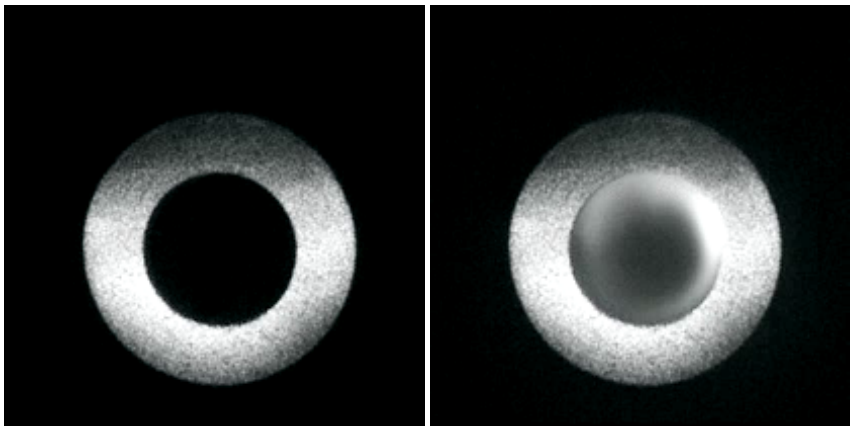

(a) Gas flow (no discharge) (b) Visible discharge

Figure 5.6: Two consecutive frames taken from high-speed imaging of the nozzle outlet at 4000 fps. This injection corresponds to the oscilloscope signal in Fig. 5.5. The visible discharge (b) is the down signal at $\approx 0.15s$ of Fig. 5.5, which was visible for only one frame.

microspheres an almost 10 times enhancement was seen in the measured charge, reaching the maximum surface charge concentration found in Chapter 3 and 4. A possible explanation for this large variation will be discussed in Section 6.1.
In addition, another test was performed in which the T piece containing the powder sample was heated up to 220°C typically for 15 minutes using a heat gun prior to injection, while being in dry condition (at chamber pressure, $\approx 2.5mbar$, using both air and Argon, $RH < 1\%$). Successively, injections were performed when the particles/injector tube were still hot, or after waiting for the system temperature to go back to ambient temperature. This test was made in order to try avoiding completely the formation of a water layer at the particle/surface contact. However, no significant variations were observed on the final charge measurement results.

5.5 Particle electrification as a function of transit through the injection tube

Particle electrification as a function of transit through the injection tube has been studied using the Faraday tube technique (Section 2.5) with two different

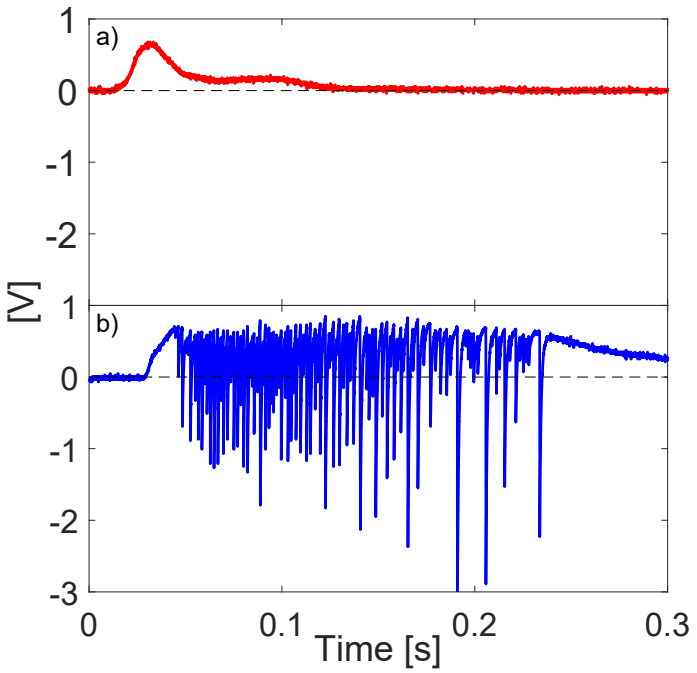

Figure 5.7: Voltage measured on the injection tube during an aerosolizing injection, it should correspond to the rate of charge leaving (or entering) the system. (Injection pressure: $\approx 20mbar$. Chamber pressure: $2.5mbar$) Figure 8a) shows the first injection after cleaning of the injection system, figure 8b) shows an injection performed after repeated injections in which it is assumed that accumulation of particulates has occurred leading to increased charge exchange and also the observation of numerous "discharge" like features, these have a rapid onset (fall lasting of the order of 1ns) and an exponential return to previous voltage. The rapid onset is assumed to be a sudden transfer of charge between the electrified aerosol and the injector tube within the chamber. The exponential decay is compatible the subsequent discharge of the injector tube through the oscilloscope probe resistor ($10M\Omega$).

Table 5.1: The dependence of measured surface charge concentration values with respect to relative humidity is presented for 2 samples. The injector material used in these experiments was always SiO2. *$RH < 2\%$ is the relative humidity inside the environmental chamber that particles experience before the injection process. The gas from the injection side is air at ambient humidity ($RH \approx 50\%$), therefore the humidity seen by the particles during the injection process may vary and is poorly constrained.

Particle material	**Humidity $\ll 1\%$ (Argon)**	**Humidity $< 2\%$ (Air*)**	**Humidity $\approx 50\%$ (Air)**
Al_2O_3 (4.6μm)	+40 ± 7	+50 ± 9	+33 ± 3
SiO_2 (2μm)	-11 ± 0.3	-14 ± 5	-104 ± 3

set of tests.
The first consisted of splitting the Faraday system into two sections: the T piece (length: 4 cm) and the long tube (length: 42 cm) were electrically isolated in order to study individually the Q transferred to each section. The amount of charge exchanged with the T piece is measured integrating the oscilloscope channel 1 signal $Q_1 = Q_{CH1}$. These charged particles must enter in the long tube section generating the same signal with an opposite polarity, as shown in Fig. 5.8. The charge generated in the long tube section is then quantified as $Q_2 = Q_{CH1} + Q_{CH2}$. Such technique allows also to calculate the total net charge generated as $Q_{tot} = Q_1 + Q_2 = 2Q_{CH1} + Q_{CH2}$. A typical measurement (Fig. 5.8) shows that around 10% of the total charge is generated in the T piece ($Q_1/Q_2 \approx 0.1$). These tests also confirmed that the ball valve connecting the T piece and the long tube (valve 2 in Fig. 2.3) seems not to contribute significantly to the particle charge generation.
A second set of tests was performed by reducing the length of the copper foil enclosure (i.e. reducing the Faraday tube length) to around 18cm with respect to the typical 48cm (i.e. to around 38% of the length). Using Al_2O_3 as the tube material and 11.8 μm Soda Lime Glass spheres the measured charge was $-8.3 \pm 0.6 \cdot 10^{-8} C$ and $-8.7 \pm 0.3 \cdot 10^{-8} C$ for respectively the long and short Faraday tube injecting the same particle mass, i.e. essentially the same transferred Q.
Such results indicate that the T piece section (4 cm long) is not enough to generate the maximum charging, whereas it is reached already after 18 cm from the beginning of the T piece section. As it is not clear whether single or multiple wall interactions are necessary to achieve this charge, these results indicate either a weak dependence of electrification upon tube length (this would

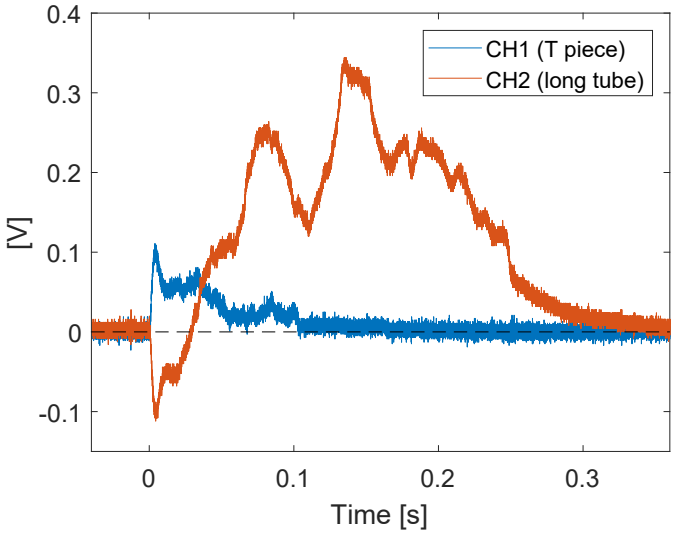

Figure 5.8: Raw oscilloscope data from a measurement of the voltage on the T piece (Channel 1) and the long tube portion (Channel 2). It can be observed that particles initially leave the T piece (positive voltage on Ch 1) and enter the long tube (mirrored negative voltage on Ch 2). When particles leave the long tube, a net positive current is measured on Ch 2. By integration of the 2 portions, it can be observed that the total charge generated in the long tube portion is higher than in the T piece. In this specific test Soda Lime Glass spheres (1-8 µm) were electrified against a stainless steel injector, with reservoir and chamber pressure respectively $p_0 = 11.6 mbar$, $p_{\text{ch}} = 2.5 mbar$.

imply that not every particle has experienced collisions with the injector system within the T piece section) or possibly that a maximum electrification had been achieved already after transiting for 18 cm as a result of multiple contacts.

Chapter 5

CHAPTER 6

DISCUSSIONS

6.1 A predictive model for contact electrification

In Section 4.1 a linear correlation is seen between χ_{AGR} (absolute generalized relative electronegativity) and the surface charge concentration σ on a particle.
A simple physical interpretation with regards to this correlation can be derived based upon an electron transfer model applied to insulators [107]. When a contact between particle and wall is established, χ_{AGR} may be interpreted as a potential difference dV, as electronegativity represents the energy change which accompanies the removal or addition of one electron [113]. Electron transfer between the two surfaces may then be expected to occur until an equal and opposite potential is produced.
The electrical charge concentration at the contact site necessary to achieve this potential (σ_{c}) may be quantified by treating the two contacting surfaces as a classical parallel plate capacitor:

$$\sigma_c = \frac{dV}{\delta_{\mathrm{l}}} \cdot \epsilon_0 \epsilon_{\mathrm{r}} = \chi_{\mathrm{AGR}} \cdot \epsilon_0 \epsilon_{\mathrm{r}} / \delta_{\mathrm{l}} \tag{6.1}$$

Where $\epsilon_0 \epsilon_{\mathrm{r}}$ is the permittivity at the contact site and δ_{l} is the effective surface-particle separation, which may be estimated as the effective bond length. The ratio $\frac{dV}{\delta_{\mathrm{l}}}$ can be interpreted as the electric field generated at the contact site.
The charge q transferred from the reference (injector tube) surface to a particle

may then be determined given the contact area (A_c):

$$q = \sigma 4\pi r^2 = \sigma_c A_c = A_c \chi_{AGR} \cdot \epsilon_0 \epsilon_r / \delta_l \tag{6.2}$$

Here σ is the total surface charge concentration if the charge is assumed to be spread over the entire particle surface, whereas σ_c is the surface charge concentration developed at the contact site.
This model allows a prediction of the surface charge concentration dependence as a function of the absolute generalized relative electronegativity χ_{AGR} (the parameter a in Eq.4.1, Fig. 4.1) as:

$$a = \frac{d\sigma}{d\chi_{AGR}} = \frac{A_c}{4\pi r^2} \frac{\epsilon_0 \epsilon_r}{\delta_l} \tag{6.3}$$

This simple calculation can be applied to any material with a known chemical composition. For example with SiO_2, the separation δ_l can be estimated from the silicon-oxigen bond length ($\delta_l \approx 1.6$Å) and the relative permittivity is $\epsilon_r \approx 3.9$. The major problem comes when estimating the effective contact area of particle-surface contact. Previous experimental determination of the contact adhesive force has been made for some micron-scale particles [79, 80, 114]]. The measured values are in reasonable agreement with the adhesive force that would be predicted from simplistic classical adhesion models as $F_{adh} = 2C_{adh}r$, where C_{adh} is an empirical parameter [15]. The contact area may be estimated in first approximation from the classical Hertzian model as:

$$A_c = \pi \left(\frac{3FR_*}{4Y_*} \right)^{2/3} \tag{6.4}$$

Where $\frac{1}{R_*} = \frac{1}{R_1} + \frac{1}{R_2}$ is used to calculate the effective radius, where R_1 and R_2 are the radius of the two contacting surfaces (R_* is equal to the particle radius, for particle-wall contact where $R_2 \to \infty$) and $\frac{1}{Y^*} = \frac{1}{Y_1} + \frac{1}{Y_2}$ the effective Young's modulus.
For a $6\mu m$ SiO_2 particle, given an adhesive force $F_{adh} \approx 5nN$ [79], knowing the effective Young's modulus for glass-glass contact ($Y_* \approx 36GPa$) and assuming a smooth sphere, Eq. 6.4 gives a contact area of around $A_c \approx 144nm^2$ and therefore a predicted gradient of $d\sigma/d\chi_{AGR} \approx 1.7e/\mu m^2/V$. Interestingly, this is in reasonable (order of magnitude) agreement with the measured gradient ($4.7e/\mu m^2/V$, as calculated in Section 4.1), implying that such a simple model is not unreasonable and may be representative of the contact electrification process.
This simple model does not directly take into account the b parameter in Eq.

4.1 which implies that even two chemically identical materials will still exchange charge. Such offset has been observed also in other previous studies [42, 43] and might be interpreted as the manifestation of the experimentally observed size dependence in tribo-electrification [36, 47, 48, 50], where two contacting particles of dissimilar sizes tend to electrify with the small particle being negative and the large particle (in this case the tube surface) positive (see also Section 1.1.4).
It may be argued here that these oxide materials are classical insulators, i.e. the electrons are not mobile at their surfaces. Importantly, here the oxide materials cannot be considered as classical insulators, as the electric field generated at the contact site exceeds their typical dielectric strength ($10^7 - 10^8 V/m$). This also implies that a significant charge spreading is expected to occur, until the electric field decreases below the dielectric breakdown voltage. This is roughly 10% of the volume of a Silica particle (dielectric strength around $3 \cdot 10^7 V/m$), considering all the charge concentrated initially in the contact area.
Remarkably, this is merely an order of magnitude estimate and may lead to large errors, especially due to a poor estimation of the effective contact area: the adhesive force is only estimated from previous experimental work [79, 80, 114], and surface roughness is neglected.
As observed in Section 5.4, a substantial increase in the measured surface charge concentration has been observed at high humidity (i.e. around 50%) specifically for Silica particles. This effect might be due to the creation of surface adhered water which may form water bridges, significantly increasing the effective contact area. This effect would then be expected to be material dependent, based on the hygroscopicity of the particle/injector material. This argument is supported by observations of anomalous enhanced adhesion observed for silica microsphere particles at high RH values [79, 115]. An alternative charge exchange process as ion exchange might also happen through the water layer, thus enhancing the measured charge.

The predictive model presented here may have general validity for both conductive/insulating materials. Electronegativity is defined as the tendency of an atom to attract electrons, and in its generalized form extends its meaning to molecules. Similarly, the work function is defined as the thermodynamic work necessary in order to remove an electron from the material to vacuum in a state of rest nearby the surface. However, these two quantities are not entirely equivalent (see Fig. 4.5). Electronegativity can be analytically calculated (e.g. in the absolute Mullikan's scale is the mean of the ionization energy and electron affinity), whether the electron work function rely on measurements that substantially vary in literature depending on the experimental technique,

and it is dependent on crystal face orientation. Based on the results of this work, neither of the two quantities is extremely well correlated to the surface charge concentration measured with metals (Fig. 4.3, 4.4) but also both show a certain trend.
Also, since typical electric fields locally generated at the contact site exceed the dielectric breakdown limit typical of insulators it may be reasonable to consider such insulators equivalent to conductive materials (at least locally).

6.2 Electron transfer VS ion transfer models: reasons for supporting electron transfer in dry contact electrification

Whereas the contact electrification process between two metallic (conductive) surfaces is almost certainly due to electron transfer [25, 26], there is still disagreement upon the charge transfer mechanisms in insulators: this can potentially be due either to electron or ion transfer, or possibly a combination of the two processes [41] (see Section 1.1).
Usually ion-contaminant transfer models involve the presence of a water layer at the contact site and/or are correlated with the Lewis acid/base property of the materials. As discussed in Section 5.4, at extremely dry conditions ($RH \ll 1\%$) contact electrification is still present i.e. a water layer is not required for charge exchange to happen, and we also observed little dependence upon the surrounding gas (Section 5.1). For this reason we might argue here that the contact electrification mechanism is not necessarily related to materials in solutions (i.e. the presence of adsorbed surface water) and ionization of water or gas molecules as charge carriers in the form of ions. It is not possible though to exclude entirely that ions can be carried from one material to another, as claimed in Wiles et al. [41]. For example, ion-material transfer is energetically plausible: the vaporization energy of SiO_2 is 143.4 kcal/mol [116] (i.e. $\approx 6eV$ per molecule) and indicates the amount of energy needed to break molecular bonds at the surface. This value is roughly comparable with the difference in χ_{AG} between the materials used here, and it is an underestimate as it does not consider the energy recover when the ion is transferred on the opposite surface. However there is no direct evidence for this material transfer to be happening and further investigations should be carried on, e.g. involving transmission electron microscopy (TEM) on particles after contact charging.
None of the arguments presented here would prove that an exclusive process (either electron or ion transfer) is always the charge carrier. Nevertheless, the

discussion presented in 6.1 indicate that a simple electron transfer model based the chemical properties of the two surfaces (i.e. electron affinity and ionization potential, electronegativity) correlates well with our data set and also with similar previous experimental studies (see Section 6.4), at least for pure oxides. It would be clearly of great interest to try applying this model to more complex chemical structures, e.g. polymers. Here another problem arises: estimating an absolute generalized electronegativity for such materials. This can be another research challenge for extending this study.

6.3 Limiting factors for the maximum measured charge

The concept of a maximum surface charge concentration has deep roots in literature and is supported by a large range of experimental studies [14,23,32,46, 55], with measured values around $0.01-0.1 mC/m^2$ ($60-600 e/\mu m^2$).
In Section 3.1 single-particle charge measurement revealed a large set of electrified particles with a narrow surface charge concentration range around $\pm 100 e/\mu m^2$. This upper and lower limit was seen also when measuring the average surface charge concentration over the whole particle cloud in Section 4.1. It is not clear why a process with such complex dynamics, i.e. involving possibly multiple collisions between particles and the injector wall and with highly non-stationary flow, should lead to a well defined limit for the surface charge concentration instead of a broad distribution of electrification states.
A possible explanation would involve the concept of an upper limit (maximum surface charge concentration). The physical nature of this limit might be electrical breakdown through gas molecules, essentially due to the potential difference established between a particle and the injector wall. However, for a single spherical particle the surface voltage is calculated as $V = q/4\pi\epsilon_0 r$, e.g. for a 8 µm particle it is around $5.5V$, which is then well below the minimum gas breakdown voltage of e.g. $\approx 300V$ for air. Also, the typical length scale, i.e. particle size, and pressure ($p \cdot d < 0.01 mbar \cdot cm$) makes this process extremely unlikely, given the Paschen curve for e.g. air (Fig 1.1).
Gas discharge is more likely at the macroscopic scale of the injection tube: considering a number concentration of electrified particle of around $10^5/mm^3$ (which is reasonable given the total number of particles per injection, usually 10^{10} for a 1 µm particle), and assuming an average charge of around $400e$ per particle (see Table 3.1), a particle cloud of the size of the tube radius (e.g. a

sphere with 2 mm diameter) would have a potential at its surface of:

$$V_{sur} = \frac{Q}{4\pi\epsilon_0 R} \approx 1000V \tag{6.5}$$

which is compatible with gas breakdown given the Paschen curve, also considering that the chamber pressure is around 2.5mbar and the characteristic distance 2mm makes it around the minimum for Paschen breakdown. This order-of-magnitude calculation shows that the intense spikes observed sometimes on the oscilloscope signal (e.g. in Fig. 5.7) may be due to gas breakdown from a cloud of electrified particles to the injector tube. A flat region following a discharge, as in Fig. 5.5, may imply that the breakdown can propagate inside the injector tube discharging particles that are flowing in the tube. Such flat (neutral) regions lasted for around $2-3ms$, interestingly this is comparable with the time it takes for a fluid particle to travel from the reservoir to the tube exit (see Section 5.3).
Another process possibly driving gas breakdown might be due to electrified aggregates: in Section 3.3, the effective surface voltage of an electrified aggregate ($\approx 55\text{e}/\mu\text{m}^2$ for a 1 mm aggregate) would be around $\approx$ 400V which is in reasonable agreement with the voltage expected if limited by gas breakdown at this pressure-distance range ($\approx 1\text{mbar}\cdot\text{cm}$).

However, as gas breakdown was only sometimes observed, none of the arguments presented above would explain such a large set of equally electrified particles, with a limit around $\pm 100\text{e}/\mu\text{m}^2$. A possible explanation for it may be electron field emission [25,26], expected for electric fields exceeding $> 10^9\text{V/m}$ at the contact site. For this, we may assume all the measured charge as concentrated in the contact area, which from Eq. 6.4 may be again estimated as $A_c \approx 144\text{nm}^2$ (see Section 6.1) obtaining a surface charge density in the contact area $\sigma_c \approx 8\cdot 10^7\text{e}/\mu\text{m}^2$. This would then generate an electric field between the particle surface and the injector tube (calculated as the electric field of a parallel plate capacitor) of:

$$E = \sigma_c/\epsilon_0 \approx 10^{12}\text{V/m} \tag{6.6}$$

which is exceeding by three orders of magnitude the electric field required for field emission. It should be noted here that this model assumes a perfectly smooth sphere and reference surface (which is not realistic), and assumes that there is no water bridging possibly enhancing the contact area. Also, electrical charge spreading may happen as the local electric field exceeds the dielectric breakdown of these materials [63] (typically of the order of $10^7 - 10^8\text{V/m}$).

Therefore a combination of electron field emission and lateral charge spreading (locally causing these insulating materials to become conductive) might contribute to the observed well defined maximum surface charge concentration.

6.4 Comparing the results with previous experimental works

This work showed reasonable agreement upon the order of magnitude of the maximum surface charge concentration measured for insulating particles, i.e. around $0.1 mC/m^2$ [14, 23, 32, 42, 43, 46, 55].
Remarkably, extremely good agreement was found with the work of Oguchi and Tamatani [42], where also a linear relation was shown between generalized electronegativity and the charge per mass of several oxide powders. In their work a different approach was followed, where micron-sized particles were blown into a Faraday cup after being in contact with a reference material (i.e. larger grains of Iron oxide particles, impeded to enter the faraday cup through a metal mesh).
Specifically for oxides it was found the following relation:

$$Q_0 = \frac{Q\rho_0}{M} = 427 - 37.1\chi_{(\mathrm{P,G})} \tag{6.7}$$

where ρ_0 is the specific gravity (i.e. the ratio between the particle density and a reference density) and $\chi_{(\mathrm{P,G})}$ is the generalized electronegativity expressed in Pauling's units. Similar linear relations were found for a set of fluorides and sulfides particles.
It is possible to convert the relation obtained by Oguchi and Tamatani [42] (Eq. 6.7) in the same units used in this work (Section 4.1, Eq. 4.1): this is done by converting electronegativity from Pauling's units $\chi_{(\mathrm{P,G})}$ into the absolute generalized electronegativity χ_{AGR}, and the charge Q_0 into surface charge concentration σ. This was possible because in [42] particle sizes were all within a narrow range, around $0.4\mu m$.
The results of this comparison are presented in Fig. 6.1, together with the numerical values for a and b in Table 6.1, including also the a value predicted by the physical model presented in Section 6.1 (Eq. 6.3). The experimental values are in extremely good agreement, especially considering the typical uncertainties in experimental studies of contact electrification [24, 25]. Also a comparable offset for electrification of a particle against the same reference material is found (b value in Table 6.1), even though specifically in [42] neutral

Table 6.1: A list of the a and b parameters comparing the present work, the work of Oguchi & Tamatani [42,43], and the value obtained from the proposed physical model (Eq. 6.3). The injector (reference surface) material composition is in all cases an oxide.

Particle composition	a $[e/\mu m^2/V]$	b $[e/\mu m^2]$
Oxides fit (this work)	4.7 ± 0.9	-27 ± 10
Oxides [42,43]	4.9	-20
Fluorides [42,43]	3.6	-35
Sulfides [42,43]	3.1	-57
Predictive model for oxides (Eq. 6.3)	1.7	0

charge was measured with SiO_2 against quartz as a reference material.

On another hand, measurements of metal (conductive) particles presented in this thesis led to results that are not entirely agreeing with those obtained by Harper [26]. Despite being 50 years old, Harper's work is, to the knowledge of the author, still the most relevant for correlating charge and electron work function for metal spheres, followed by Lowell's work [27] which essentially confirmed his results. Harper obtained a better correlation with work function than the one found here (Fig. 4.3). His successful correlation was attained only when the contact potentials were measured for the actual surfaces for which the charge was determined [26]. This was possible due to the large sizes of his metal spheres (mm size) while is not possible in our setup, as we used micron sized particles. Also oxidized layers play a role in the determination of contact charging: measurements of copper particles in copper tube clearly showed that non-oxidized (or less oxidized) surfaces lead to much different results (i.e. change in the charge polarity) (see Section 2.7). Also Harper observed a lower charge than the theoretically predicted one, justifying it by the presence of surface impurities and oxidized layers.
Interestingly, Harper measured low surface charge concentration values, of around $10^{-5} mC/m^2$ ($0.05 e/\mu m^2$) for a 4mm chromium metal sphere, in contact with other 13mm metal spheres [24, 26], i.e. 3 order of magnitude lower. This might be due to the invasive measurement technique, as the two spheres were attached to precision-lever apparatus.

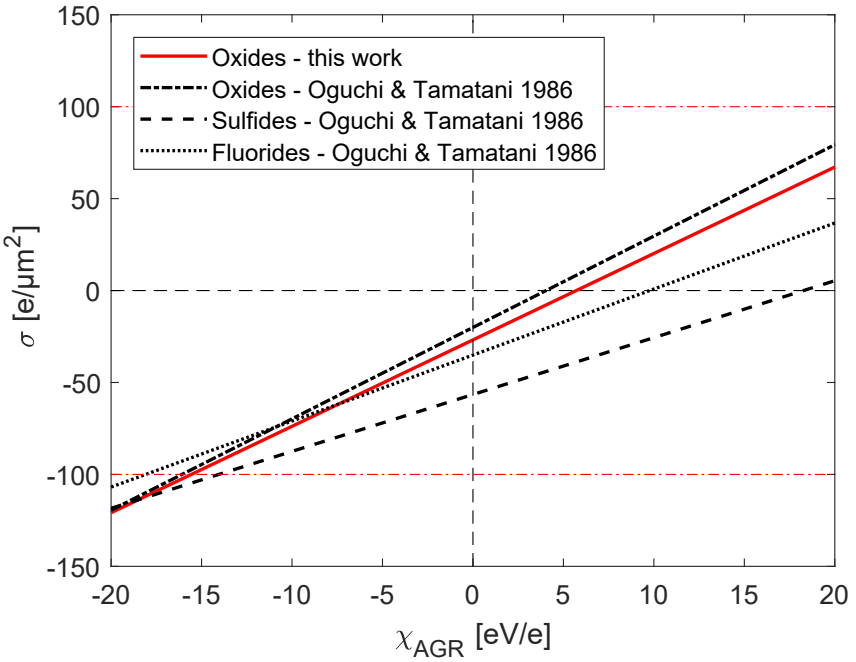

Figure 6.1: Comparison between the predictive model found in Section 4.1 and the models derived in Oguchi & Tamatani, 1986 [42]. The latter have been converted in the units used in this work (χ_{AGR} in $[eV/e]$ and σ in $[e/\mu m^2]$).

6.5 Effect of broad size distribution and particle composition for volcanic ash samples

A downside of measuring an average surface charge concentration using the Faraday tube technique is represented by the need to apply an effective mean particle size of the sample. Clearly using the mean value of the particle size distribution should work reasonably well for narrow PSD. However, for broad size distribution and non spherical particle the mean value of the volumetric PSD introduces an error.

This effect is seen especially when using volcanic ash samples (Section 4.3), where size and composition dependence could not be accurately isolated. The generated charge appears to be dominated by the fine particle fraction. This is particularly evident for the sample 'MSH', which shows a too high surface charge concentration (see Fig. 4.7). In this case, also uncertainty on the determination of χ_{AGR} furthermore complicate the picture. It would be of great

interest for future studies to be able to study with a narrow PSD to constrain better the composition dependence for both metal and volcanic ash samples. Also for natural samples such as volcanic ash, there is the need of developing a better way of estimating the effective χ_{AGR}: ash is not, in fact, a composition of pure oxides. Eq. 4.2 applies well only for pure oxides, whether other forms of chemical component might require a different formulation.

Chapter 6

Chapter 6

CHAPTER 7

CONCLUSIONS

In this work novel precision techniques have been developed and applied in order to study the contact electrification process (also known as tribo electrification) in solid aerosolized particles. Specifically, the dependence upon size, chemical composition and aerosolizing gas properties has been investigated. An aerosolizer system was used to disperse (aerosolize) solid particles into an environmental chamber under controlled conditions (gas composition, pressure and relative humidity). This was achieved by the rapid decompression of a gas reservoir through an injector tube. Particles were electrified by contact with the injector tube during the aerosolization process. Several combinations of particles (i.e. oxides, metals and volcanic ash samples) and injector tube material were studied.

In one measurement technique an AC electric field was applied and a 2D Laser Doppler Velocimeter was used to measure simultaneously the size and electric charge of individual grains by determining their settling and drift velocities. Particles interacting with the injector tube were seen to be electrified with a narrow range of surface charge concentration σ of around $\pm 100 e/\mu m^2$, independently of particle size (i.e. the charge on a particle scales with its total surface area). It was proposed that contact electrification was high for these particles, limited by some form of discharge. Electron field emission at the contact site has been potentially identified as the physical process limiting the maximum surface charge concentration, as the electric field generated at the contact site would be in excess of the one necessary for field emission ($\approx 10^9 V/m$).

Possibly lateral charge spreading across the particle material (due to overcoming of the material dielectric breakdown limit) also occurred.
In a second measurement technique a conductive Faraday cage enclosed the injector tube, and the current generated by charged particles exiting the tube was measured using an oscilloscope (i.e. a Faraday tube type technique). The average charge/mass over the entire particle cloud measured with oxide powders (1-45 μm) was seen to have an inverse dependence on particle size (1/r), consistent with a constant particle surface charge concentration (as also seen with the single particle LDV technique).
Interestingly, the measured surface charge concentration for a set of oxide (insulating) particles was also seen to correlate linearly with particle composition, expressed using the absolute generalized relative electronegativity χ_{AGR}, which can be calculated by knowing the electronegativity of the metal element bound in the oxide molecule and its valence. The simple relation for estimating (predicting) particle surface charge concentration is expressed as $\sigma = a\chi_{\mathrm{AGR}} - b$, where $a = 4.7\mathrm{e}/\mu\mathrm{m}^2/\mathrm{V}$, $b = -27\mathrm{e}/\mu\mathrm{m}^2$ are empirical parameters calculated from a linear fit to our experimental data set. A more general expression has also been formulated for estimating χ_{AG} in compound materials (e.g. soda lime glass) by taking into account the molecule number percentage of each oxide composing the compound.
A physical interpretation of this model is put forward. Here the absolute generalized relative electronegativity χ_{AGR} is interpreted as an effective contact potential difference, and the magnitude of the charge exchanged is such that it produces an equal and opposite potential. By estimating the contact area using conventional models, this expression leads to a prediction of the gradient $a = d\sigma/d\chi_{\mathrm{AGR}}$ in reasonable agreement with the experimentally derived gradient. This simple model may potentially be used to predict the electrification between any contacting material, once the effective χ_{AGR} is known. The magnitude of the electric field at the contact site (which is far in excess of the dielectric breakdown voltage of the material) and the characteristic small spatial scale (≈nm) might allow electron transfer, despite these materials being classically considered insulators.
The charge of particle aggregates (as large as mm size) was measured, with their surface charge concentration ranging from almost zero up to $55\mathrm{e}/\mu\mathrm{m}^2$. The amount of aggregated particles and also particle adhesion to the injector tube wall was seen to reduce the total charge measured. Cohesion/adhesion were observed to increase at small particle size, and were highly significant for particles smaller than 1 μm.
Electrification of metal (conductive) powders has also been measured using metal injector tube (copper or stainless steel): the range of surface charge con-

centrations was seen to be compatible with the one determined for oxide powders, and a correlation with relative electron work function and electronegativity was observed although this trend was less clear than the one observed with oxides, presumably due to poor determination of the work function.
Contact charging of volcanic ash samples was measured, and results confirmed a surface charge concentration within the expected range, again showing a tendency for the measured charge/mass to increase with the inverse of particle size 1/r (constant surface charge concentration). A reasonable agreement was found with the predictive model for oxides (Eq. 4.1) by considering the particles composed of pure SiO_2. Surprisingly, no clear dependence was found upon minor mineral components. Broad particle size distributions were seen to constitute an additional source of uncertainty.
The generated charge was also investigated as a function of the aerosolizing gas composition using air, Argon and CO_2. The mean measured surface charge concentration did not seem to correlate linearly with breakdown voltages typical of these gases, indicating that gas breakdown should not be the limiting factor for the generated charge. However, a trend was observed for increasing charge with around 50% increase between Ar and CO_2.
Relative humidity was seen to play an important role specifically for silica (SiO_2), showing almost 10 times increased surface charge concentration at around 50% RH. Note that most of the experiments performed here can be considered to be in dry conditions (RH < 2%).
Electrical breakdown through gas was sometimes observed both through characteristic features seen on the injector tube voltage (rapid and intense spikes), and as light using an high speed camera (glow discharge). Such discharges might be due to gas breakdown between the electrified (aerosolized) particle cloud inside the chamber and the injector tube. A single discharge was seen to reduce as much as 6% the total generated charge.
Particle electrification as a function of transit inside the injector tube was studied by modifying the length of the Faraday tube extension. Results showed that after around 38% of the total tube length a maximum charge was already reached. Also the effect of varying the reservoir gas (air) pressure was investigated, here the charge of the entire particle cloud was not seen to vary for initial reservoir pressures between 1bar and 100mbar, but decreased below 100 mbar (chamber pressure at 2.5 mbar). This corresponds to the expected pressure threshold for a transition between turbulent and laminar flow within the aerosolizing injector tube: although it is not clear if single or multiple collisions are necessary to reach this maximum charge, such observations indicated that the number of particles colliding with the injector tube is crucial for the total charge generated over the entire particle cloud.

The charge values obtained in this work are in reasonable agreement (order of magnitude) with typical values measured in previous experimental work. In particular, the composition dependence addressed here agrees extremely well with a previous study from Oguchi and Tamatani [42], where the measured charge was also seen to relate with the generalized electronegativity.

Despite the persistent lack of a universally accepted model for contact electrification, this work is hoped to be of considerable use in predicting and understanding contact electrification in aerosol particles (especially insulators), and also for placing further requirements to possible models.
Potentially interesting ideas for continuing and extending this study include a dedicated investigation of contact electrification between particles composed of the same material and different sizes, which is one of the many unanswered questions in contact electrification. The LDV measurement technique would be appropriate to investigate such phenomena as it can directly measure size and charge of individual grains, but another aerosolizing technique which reduces the influence of particle-wall contact should be developed: for example, it may help using a shorter and wider aerosolizing tube, using a material such that its chemical composition should not lead to high charging (its absolute generalized electronegativity may be determined by using our predictive model in Eq. 4.1). Also interesting would be investigating the origin of the b offset in Eq. 4.1, which expresses the surface charge concentration of a particle contacting against the same reference material. Other insulating compounds (e.g. salts, polymers) should be studied for a comprehensive understanding of contact charging in insulators. Another great challenge would be to extend the generalized electronegativity model to more complex chemical compositions, in order to predict contact electrification in all (dry) insulating and possibly also conductive materials. In addition, dedicated studies of the surface of contact electrified materials (e.g. using AFM, atomic force microscopy) could be of considerable use for understanding what is the charge carrier in various materials and environmental conditions.

References

[1] Patricia F O'grady. *Thales of Miletus: the beginnings of western science and philosophy*. Routledge, 2017.

[2] R Giles Harrison, E Barth, F Esposito, Jonathan Merrison, Franck Montmessin, KL Aplin, C Borlina, Jean-Jacques Berthelier, Grégoire Déprez, and William M Farrell. Applications of electrified dust and dust devil electrodynamics to martian atmospheric electricity. *Space Science Reviews*, pages 1–47, 2016.

[3] D Boland and D Geldart. Electrostatic charging in gas fluidised beds. *Powder Technology*, 5(5):289–297, 1972.

[4] Jun Yao, Yan Zhang, Chi-Hwa Wang, Shuji Matsusaka, and Hiroaki Masuda. Electrostatics of the granular flow in a pneumatic conveying system. *Industrial & engineering chemistry research*, 43(22):7181–7199, 2004.

[5] Farzam Fotovat, Xiaotao T Bi, and John R Grace. Electrostatics in gas-solid fluidized beds: A review. *Chemical Engineering Science*, 173:303–334, 2017.

[6] Yu Pu, Malay Mazumder, and Charles Cooney. Effects of electrostatic charging on pharmaceutical powder blending homogeneity. *Journal of pharmaceutical sciences*, 98(7):2412–2421, 2009.

[7] Kalyana C Pingali, Troy Shinbrot, Stephen V Hammond, and Fernando J Muzzio. An observed correlation between flow and electrical properties of pharmaceutical blends. *Powder Technology*, 192(2):157–165, 2009.

[8] LB Schein. Recent advances in our understanding of toner charging. *Journal of electrostatics*, 46(1):29–36, 1999.

[9] Adrian G Bailey. The science and technology of electrostatic powder spraying, transport and coating. *Journal of electrostatics*, 45(2):85–120, 1998.

[10] S Matsusaka and H Masuda. Simultaneous measurement of mass flow rate and charge-to-mass ratio of particles in gas–solids pipe flow. *Chemical Engineering Science*, 61(7):2254–2261, 2006.

[11] M Ghadiri, CM Martin, JEP Morgan, and R Clift. An electromechanical valve for solids. *Powder technology*, 73(1):21–35, 1992.

[12] Guiqing Wu, Jia Li, and Zhenming Xu. Triboelectrostatic separation for granular plastic waste recycling: A review. *Waste Management*, 33(3):585–597, 2013.

[13] H Frank Eden and Bernard Vonnegut. Electrical breakdown caused by dust motion in low-pressure atmospheres: Considerations for mars. *Science*, 180(4089):962–963, 1973.

[14] Jonathan Merrison, J Jensen, K Kinch, R Mugford, and Per Nørnberg. The electrical properties of mars analogue dust. *Planetary and Space Science*, 52(4):279–290, 2004.

[15] Jonathan Merrison. Sand transport, erosion and granular electrification. *Aeolian Research*, 4:1–16, 2012.

[16] Jonathan P Merrison, Haraldur Pall Gunnlaugsson, MR Hogg, M Jensen, JM Lykke, M Bo Madsen, MB Nielsen, Per Nørnberg, TA Ottosen, and RT Pedersen. Factors affecting the electrification of wind-driven dust studied with laboratory simulations. *Planetary and Space Science*, 60(1):328–335, 2012.

[17] TA Mather and RG Harrison. Electrification of volcanic plumes. *Surveys in Geophysics*, 27(4):387–432, 2006.

[18] Corrado Cimarelli, MA Alatorre-Ibargüengoitia, Ulrich Kueppers, Bettina Scheu, and Donald B Dingwell. Experimental generation of volcanic lightning. *Geology*, 42(1):79–82, 2014.

[19] MR James, L Wilson, SJ Lane, JS Gilbert, TA Mather, RG Harrison, and RS Martin. Electrical charging of volcanic plumes. In *Planetary Atmospheric Electricity*, pages 399–418. Springer, 2008.

[20] SJ Lane and JS Gilbert. Electric potential gradient changes during explosive activity at sakurajima volcano, japan. *Bulletin of Volcanology*, 54(7):590–594, 1992.

[21] MR James, SJ Lane, and Jennie S Gilbert. Volcanic plume electrification: experimental investigation of a fracture-charging mechanism. *Journal of Geophysical Research: Solid Earth*, 105(B7):16641–16649, 2000.

[22] Elisabetta Del Bello, Jacopo Taddeucci, Jonathan Merrison, Stefano Alois, Jens Jacob Iversen, and Piergiorgio Scarlato. Parameterization of volcanic ash remobilization by wind-tunnel erosion experiments. In

EGU General Assembly Conference Abstracts, volume 19, page 13873, 2017.

[23] Daniel J Lacks and R Mohan Sankaran. Contact electrification of insulating materials. *Journal of Physics D: Applied Physics*, 44(45):453001, 2011.

[24] S. Matsusaka, H. Maruyama, T. Matsuyama, and M. Ghadiri. Triboelectric charging of powders: A review. *Chemical Engineering Science*, 65(22):5781–5807, 2010.

[25] Logan S. McCarty and George M. Whitesides. Electrostatic charging due to separation of ions at interfaces: Contact electrification of ionic electrets. *Angewandte Chemie-International Edition*, 47(12):2188–2207, 2008.

[26] Wallace Russell Harper. *Contact and frictional electrification*. Clarendon Press, 1967.

[27] J Lowell. Contact electrification of metals. *Journal of Physics D: Applied Physics*, 8(1):53, 1975.

[28] Pekka Peljo, Jose A Manzanares, and Hubert H Girault. Contact potentials, fermi level equilibration, and surface charging. *Langmuir*, 32(23):5765–5775, 2016.

[29] Stanislaw Halas and Tomasz Durakiewicz. Work functions of elements expressed in terms of the fermi energy and the density of free electrons. *Journal of Physics: Condensed Matter*, 10(48):10815, 1998.

[30] DK Davies. Charge generation on dielectric surfaces. *Journal of Physics D: Applied Physics*, 2(11):1533, 1969.

[31] J Lowell and AC Rose-Innes. Contact electrification. *Advances in Physics*, 29(6):947–1023, 1980.

[32] J Lowell. Constraints on contact charging of insulators. i. spatial localisation of insulator states. *Journal of Physics D: Applied Physics*, 19(1):95, 1986.

[33] J Lowell and WS Truscott. Triboelectrification of identical insulators. ii. theory and further experiments. *Journal of Physics D: Applied Physics*, 19(7):1281, 1986.

[34] Adrian G Bailey. The charging of insulator surfaces. *Journal of Electrostatics*, 51:82–90, 2001.

[35] CB Duke and TJ Fabish. Contact electrification of polymers: A quantitative model. *Journal of Applied Physics*, 49(1):315–321, 1978.

[36] Scott R Waitukaitis, Victor Lee, James M Pierson, Steven L Forman, and Heinrich M Jaeger. Size-dependent same-material tribocharging in insulating grains. *Physical Review Letters*, 112(21):218001, 2014.

[37] Yoshiyuki Shirakawa, Naoto Ii, Mikio Yoshida, Ryusuke Takashima, Atsuko Shimosaka, and Jusuke Hidaka. Quantum chemical calculation of electron transfer at metal/polymer interfaces. *Advanced Powder Technology*, 21(4):500–505, 2010.

[38] Chongyang Liu and Allen J Bard. Electrostatic electrochemistry at insulators. *Nature materials*, 7(6):505, 2008.

[39] Chong-yang Liu and Allen J. Bard. Electrostatic electrochemistry: Nylon and polyethylene systems. *Chemical Physics Letters*, 485(1-3):231–234, 2010.

[40] Chunlei Pei, Chuan-Yu Wu, and Michael Adams. Dem-cfd analysis of contact electrification and electrostatic interactions during fluidization. *Powder Technology*, 304:208–217, 2016.

[41] Jason A Wiles, Bartosz A Grzybowski, Adam Winkleman, and George M Whitesides. A tool for studying contact electrification in systems comprising metals and insulating polymers. *Analytical chemistry*, 75(18):4859–4867, 2003.

[42] Toshihiko Oguchi and Masaaki Tamatani. Contact electrification in inorganic binary compounds. *Journal of The Electrochemical Society*, 133(4):841–847, 1986.

[43] T Oguchi and M Tamatani. Contact electrification phenomena and powder surface treatments. *Wear*, 168(1-2):91–98, 1993.

[44] HT Baytekin, AZ Patashinski, M Branicki, Bilge Baytekin, S Soh, and Bartosz A Grzybowski. The mosaic of surface charge in contact electrification. *Science*, 333(6040):308–312, 2011.

[45] S Pence, VJ Novotny, and AF Diaz. Effect of surface moisture on contact charge of polymers containing ions. *Langmuir*, 10(2):592–596, 1994.

[46] S Nieh and T Nguyen. Effects of humidity, conveying velocity, and particle size on electrostatic charges of glass beads in a gaseous suspension flow. *Journal of Electrostatics*, 21(1):99–114, 1988.

[47] Mihai A Bilici, Joseph R Toth III, R Mohan Sankaran, and Daniel J Lacks. Particle size effects in particle-particle triboelectric charging studied with an integrated fluidized bed and electrostatic separator system. *Review of Scientific Instruments*, 85(10):103903, 2014.

[48] Keith M Forward, Daniel J Lacks, and R Mohan Sankaran. Charge segregation depends on particle size in triboelectrically charged granular materials. *Physical review letters*, 102(2):028001, 2009.

[49] Jasper F Kok and Daniel J Lacks. Electrification of granular systems of identical insulators. *Physical Review E*, 79(5):051304, 2009.

[50] Daniel J Lacks and Artem Levandovsky. Effect of particle size distribution on the polarity of triboelectric charging in granular insulator systems. *Journal of Electrostatics*, 65(2):107–112, 2007.

[51] SR Waitukaitis and HM Jaeger. In situ granular charge measurement by free-fall videography. *Review of Scientific Instruments*, 84(2):025104, 2013.

[52] Daniel J Lacks, Nathan Duff, and Sanat K Kumar. Nonequilibrium accumulation of surface species and triboelectric charging in single component particulate systems. *Physical review letters*, 100(18):188305, 2008.

[53] Joseph R Toth III, Amber K Phillips, Siddharth Rajupet, R Mohan Sankaran, and Daniel J Lacks. Particle-size-dependent triboelectric charging in single-component granular materials: Role of humidity. *Industrial & Engineering Chemistry Research*, 56(35):9839–9845, 2017.

[54] Andrew E. Wang, Phwey S. Gil, Moses Holonga, Zelal Yavuz, H. Tarik Baytekin, R. Mohan Sankaran, and Daniel J. Lacks. Dependence of triboelectric charging behavior on material microstructure. *Phys. Rev. Materials*, 1:035605, Aug 2017.

[55] Torsten Poppe, Jürgen Blum, and Thomas Henning. Experiments on collisional grain charging of micron-sized preplanetary dust. *The Astrophysical Journal*, 533(1):472, 2000.

[56] JS Gilbert, SJ Lane, RSJ Sparks, and T Koyaguchi. Charge measurements on particle fallout from a volcanic plume. *Nature*, 349(6310):598, 1991.

[57] Hideo Watanabe, Mojtaba Ghadiri, Tatsushi Matsuyama, Yu Long Ding, and Kendal G Pitt. New instrument for tribocharge measurement due to single particle impacts. *Review of scientific instruments*, 78(2):024706, 2007.

[58] Shuji Matsusaka, Mojtaba Ghadiri, and Hiroaki Masuda. Electrification of an elastic sphere by repeated impacts on a metal plate. *Journal of Physics D: Applied Physics*, 33(18):2311, 2000.

[59] Troy Shinbrot, Matthew Rutala, and Hans Herrmann. Surface contact charging. *Physical Review E*, 96(3):032912, 2017.

[60] Mario M Apodaca, Paul J Wesson, Kyle JM Bishop, Mark A Ratner, and Bartosz A Grzybowski. Contact electrification between identical materials. *Angewandte Chemie*, 122(5):958–961, 2010.

[61] Hideo Watanabe, Abdolreza Samimi, Yu Long Ding, Mojtaba Ghadiri, Tatsushi Matsuyama, and Kendal G Pitt. Measurement of charge transfer due to single particle impact. *Particle & Particle Systems Characterization*, 23(2):133–137, 2006.

[62] Tatsushi Matsuyama and Hideo Yamamoto. Charge-relaxation process dominates contact charging of a particle in atmospheric condition: Ii. the general model. *Journal of Physics D: Applied Physics*, 30(15):2170, 1997.

[63] Roger G Horn, DT Smith, and A Grabbe. Contact electrification induced by monolayer modification of a surface and relation to acid-base interactions. *Nature*, 366:442–443, 1993.

[64] Logan S McCarty, Adam Winkleman, and George M Whitesides. Ionic electrets: electrostatic charging of surfaces by transferring mobile ions upon contact. *Journal of the American Chemical Society*, 129(13):4075–4088, 2007.

[65] TH DiStefano and M Shatzkes. Impact ionization model for dielectric instability and breakdown. *Applied Physics Letters*, 25(12):685–687, 1974.

[66] Alexandre A Martins and Mario J Pinheiro. On the propulsive force developed by asymmetric capacitors in a vacuum. *Physics Procedia*, 20:112–119, 2011.

[67] Ekram Husain and RS Nema. Analysis of paschen curves for air, n2 and sf6 using the townsend breakdown equation. *IEEE transactions on electrical insulation*, (4):350–353, 1982.

[68] Raymond P Iczkowski and John L Margrave. Electronegativity. *Journal of the American Chemical Society*, 83(17):3547–3551, 1961.

[69] AL Allred. Electronegativity values from thermochemical data. *Journal of inorganic and nuclear chemistry*, 17(3-4):215–221, 1961.

[70] Steven G Bratsch. Revised mulliken electronegativities: I. calculation and conversion to pauling units. *J. Chem. Educ*, 65(1):34, 1988.

[71] Ken-Ichi Tanaka and Atsumu Ozaki. Acid-base properties and catalytic activity of solid surfaces. *Journal of Catalysis*, 8(1):1–7, 1967.

[72] H Zhao, GSP Castle, and II Inculet. The measurement of bipolar charge in polydisperse powders using a vertical array of faraday pail sensors. *Journal of electrostatics*, 55(3):261–278, 2002.

[73] Malay K Mazumder, RE Ware, T Yokoyama, BJ Rubin, and D Kamp. Measurement of particle size and electrostatic charge distributions on toners using e-spart analyzer. *IEEE Transactions on Industry Applications*, 27(4):611–619, 1991.

[74] S Balachandar and John K Eaton. Turbulent dispersed multiphase flow. *Annual Review of Fluid Mechanics*, 42:111–133, 2010.

[75] Robert D Zucker and Oscar Biblarz. *Fundamentals of gas dynamics*. John Wiley & Sons, 2002.

[76] JF Douglas, JM Gasiorek, JA Swaffield, and LB JACK. *Fluid Mechanics. Harlow*. United Kingdom: Prentice Hall, 2005.

[77] Juan José Peña Fernández and Jörn Sesterhenn. Compressible starting jet: pinch-off and vortex ring–trailing jet interaction. *Journal of Fluid Mechanics*, 817:560–589, 2017.

[78] Hans-Jürgen Butt, Brunero Cappella, and Michael Kappl. Force measurements with the atomic force microscope: Technique, interpretation and applications. *Surface science reports*, 59(1):1–152, 2005.

[79] R Jones, HM Pollock, D Geldart, and A Verlinden. Inter-particle forces in cohesive powders studied by afm: effects of relative humidity, particle size and wall adhesion. *Powder Technology*, 132(2):196–210, 2003.

[80] Robert Jones, Hubert M Pollock, Jamie AS Cleaver, and Christopher S Hodges. Adhesion forces between glass and silicon surfaces in air studied by afm: Effects of relative humidity, particle size, roughness, and surface treatment. *Langmuir*, 18(21):8045–8055, 2002.

[81] Lars-Oliver Heim, Jürgen Blum, Markus Preuss, and Hans-Jürgen Butt. Adhesion and friction forces between spherical micrometer-sized particles. *Physical Review Letters*, 83(16):3328, 1999.

[82] KL Johnson, K Kendall, and AD Roberts. Surface energy and the contact of elastic solids. In *Proceedings of the Royal Society of London A: Mathematical, Physical and Engineering Sciences*, volume 324, pages 301–313. The Royal Society, 1971.

[83] Boris V Derjaguin, Vladimir M Muller, and Yu P Toporov. Effect of contact deformations on the adhesion of particles. *Journal of Colloid and interface science*, 53(2):314–326, 1975.

[84] Yaping Shao and Hua Lu. A simple expression for wind erosion threshold friction velocity. *Journal of Geophysical Research: Atmospheres*, 105(D17):22437–22443, 2000.

[85] Shuji Matsusaka, Woraporn Theerachaisupakij, Hiroko Yoshida, and Hiroaki Masuda. Deposition layers formed by a turbulent aerosol flow of micron and sub-micron particles. *Powder Technology*, 118(1):130–135, 2001.

[86] Andreĭ Sergeevich Monin and Akiva M Yaglom. *Statistical fluid mechanics, volume II: Mechanics of turbulence*, volume 2. Courier Corporation, 2013.

[87] Paul E Dimotakis. The mixing transition in turbulent flows. *Journal of Fluid Mechanics*, 409:69–98, 2000.

[88] E Cunningham. On the velocity of steady fall of spherical particles through fluid medium. *Proceedings of the Royal Society of London. Series A, Containing Papers of a Mathematical and Physical Character*, 83(563):357–365, 1910.

[89] Robert A Millikan. The general law of fall of a small spherical body through a gas, and its bearing upon the nature of molecular reflection from surfaces. *Physical review*, 22(1):1, 1923.

[90] Robert A Millikan. Coefficients of slip in gases and the law of reflection of molecules from the surfaces of solids and liquids. *Physical review*, 21(3):217, 1923.

[91] Paul S Epstein. On the resistance experienced by spheres in their motion through gases. *Physical Review*, 23(6):710, 1924.

[92] Stefano Alois, Jonathan Merrison, Jens Jacob Iversen, and Jörn Sesterhenn. Contact electrification in aerosolized monodispersed silica microspheres quantified using laser based velocimetry. *Journal of Aerosol Science*, 106:1–10, 2017.

[93] Andreas Boes Jakobsen. An experimental study of aerosol settling rates in rarefied gases : measurements of terminal fall velocities of fine silica microspheres in dry air, water vapour, co2, helium, argon and xenon at reduced pressures, 2016.

[94] C. Holstein-Rathlou, J. Merrison, J. J. Iversen, A. B. Jakobsen, R. Nicolajsen, P. Nørnberg, K. Rasmussen, A. Merlone, G. Lopardo, T. Hudson, D. Banfield, and G. Portyankina. An environmental wind tunnel facility for testing meteorological sensor systems. *Journal of Atmospheric and Oceanic Technology*, 31(2):447–457, 2014.

[95] Jonathan P Merrison, H Bechtold, H Gunnlaugsson, A Jensen, Kjartan Kinch, P Nornberg, and K Rasmussen. An environmental simulation wind tunnel for studying aeolian transport on mars. *Planetary and Space Science*, 56(3):426–437, 2008.

[96] R Israel and Daniel E Rosner. Use of a generalized stokes number to determine the aerodynamic capture efficiency of non-stokesian particles from a compressible gas flow. *Aerosol Science and Technology*, 2(1):45–51, 1982.

[97] Timothy CW Lau and Graham J Nathan. Influence of stokes number on the velocity and concentration distributions in particle-laden jets. *Journal of Fluid Mechanics*, 757:432–457, 2014.

[98] Timothy CW Lau and Graham J Nathan. The effect of stokes number on particle velocity and concentration distributions in a well-characterised, turbulent, co-flowing two-phase jet. *Journal of Fluid Mechanics*, 809:72–110, 2016.

[99] DANTEC. *LDA and PDA reference manual*. Dantec Dynamics A/S, Tonsbakken 18, DK-2740 Skovlunde, Denmark.

[100] Shuji Matsusaka, H Fukuda, Y Sakura, H Masuda, and M Ghadiri. Analysis of pulsating electric signals generated in gas–solids pipe flow. *Chemical Engineering Science*, 63(5):1353–1360, 2008.

[101] Johannes Schindelin, Ignacio Arganda-Carreras, Erwin Frise, Verena Kaynig, Mark Longair, Tobias Pietzsch, Stephan Preibisch, Curtis Rueden, Stephan Saalfeld, and Benjamin Schmid. Fiji: an open-source platform for biological-image analysis. *Nature methods*, 9(7):676–682, 2012.

[102] Caroline A Schneider, Wayne S Rasband, and Kevin W Eliceiri. Nih image to imagej: 25 years of image analysis. *Nature methods*, 9(7):671–675, 2012.

[103] A Vogel, S Diplas, AJ Durant, AS Azar, MF Sunding, WI Rose, A Sytchkova, C Bonadonna, K Krüger, and A Stohl. Reference dataset of volcanic ash physicochemical and optical properties. *Journal of Geophysical Research: Atmospheres*, 2017.

[104] Anthony Rondeau. Étude de la mise en suspension aéraulique appliquée à la problématique des poussières dans le futur tokamak iter, 2015.

[105] Laure Alloul-Marmor. Reentrainement par ecoulement d'air d'une contamination particulaire deposee sur une surface application au cas d'un "tas" de poudre. *Créteil: Université Paris XII-Val de Marne*, 2002.

[106] Torsten Detloff, Titus Sobisch, and Dietmar Lerche. Particle size distribution by space or time dependent extinction profiles obtained by analytical centrifugation. *Particle & Particle Systems Characterization*, 23(2):184–187, 2006.

[107] Stefano Alois, Jonathan Merrison, Jens Jacob Iversen, and Jörn Sesterhenn. Quantifying the contact electrification of aerosolized insulating particles. *Powder Technology*, 2018.

[108] M Tamatani. Contact electrification phenomena on phosphor particle surfaces. *Journal of luminescence*, 100(1):317–323, 2002.

[109] William M Haynes. *CRC handbook of chemistry and physics*. CRC press, 2014.

[110] N. Barrett, O. Renault, H. Lemaître, P. Bonnaillie, F. Barcelo, F. Miserque, M. Wang, and C. Corbel. Microscopic work function anisotropy and surface chemistry of 316l stainless steel using photoelectron emission microscopy. *Journal of Electron Spectroscopy and Related Phenomena*, 195:117–124, 2014.

[111] Motukuru S Naidu. *High voltage engineering*. Tata McGraw-Hill Education, 2013.

[112] JP Holman. *Heat transfer, 9th*. McGraw-Hill, 2002.

[113] Raymond P Iczkowski and John L Margrave. Electronegativity. *Journal of the American Chemical Society*, 83(17):3547–3551, 1961.

[114] Robert Jones, Hubert M Pollock, Derek Geldart, and Ann Verlinden-Luts. Frictional forces between cohesive powder particles studied by afm. *Ultramicroscopy*, 100(1):59–78, 2004.

[115] J.A.S Cleaver and J.W.G Tyrrell. The influence of relative humidity on particle adhesion–a review of previous work and the anomalous behaviour of soda-lime glass. *KONA Powder and Particle Journal*, 22:9–22, 2004.

[116] HB Lim, TH Kim, SH Eom, Yong-ik Sung, MH Moon, and DW Lee. Vaporization process of sio 2 particles for slurry injection in inductively coupled plasma atomic emission spectrometry. *Journal of Analytical Atomic Spectrometry*, 17(2):109–114, 2002.

Publications related to this work

Refereed journal publications:

Alois, S., Merrison, J., Iversen, J.J. and Sesterhenn, J. *Contact electrification in aerosolized monodispersed silica microspheres quantified using laser based velocimetry.* Journal of Aerosol Science, 106 (2017): 1-10.
doi: 10.1016/j.jaerosci.2016.12.003

Alois, S., Merrison, J., Iversen, J.J. and Sesterhenn, J. *Quantifying the contact electrification of aerosolized insulating particles.* Powder technology (2018).
doi: 10.1016/j.powtec.2018.03.059

Conference proceedings:

Alois, S., Merrison, J. *Laboratory study of volcanic ash electrification.* EGU General Assembly Conference Abstracts, Vol. 18. 2016.

Alois, S., Merrison, J. *Laboratory study of solid aerosol electrification.* NOSA Symposium 2016.

Alois, S., Merrison, J., Iversen, J.J. and Sesterhenn, J. *Laboratory studies of aerosol electrification and experimental evidence for electrical breakdown at different scales.* EGU General Assembly Conference Abstracts, 2017

Del Bello, E., Taddeucci, J., Merrison, J., **Alois, S.**, Iversen, J.J., Scarlato, P. *Parameterization of volcanic ash remobilization by wind-tunnel erosion experiments.* EGU General Assembly Conference Abstracts, 2017